Systematic investigations of the ^{4}He monopole

Dissertation

zur Erlangung des Grades
„Doktor der Naturwissenschaften“
am Fachbereich Physik, Mathematik und Informatik
der Johannes Gutenberg-Universität Mainz

Simon Kegel
geboren in Speyer

Institut für Kernphysik
Johannes Gutenberg-Universität Mainz
2019

Datum der mündlichen Prüfung: 05.11.2020

ABSTRACT

Nuclear form factors are fundamental properties of nuclei and connected to several quantities of a nucleus at the same time. Precise data on form factors can be used to stringently test theoretical calculations and predictions on nuclear structure, whereas in particular chiral perturbation theory (χPT) has raised interest in the current decade among the research community.

One quantity that drew attention in the theoretical field of Few-Body-Physics is the monopole transition form factor of ^{4}He, calculated with χ-potentials [BBLO13] and established phenomenological potentials [HGK04]. These calculations include 3N-interactions and lead to very different results on the strength of the monopole transition. On the experimental side, the existing data of the transition form factor goes back almost 50 years [FRC$^+$68, KOM$^+$83, Wal70] and lacks in precision and consistency, and thus do not allow for a credible verification of the different proposed models. For a more precise determination of the monopole transition form factor $|\mathcal{F}_{M0^+}(Q_0^2)|^2$ data were taken at the A1 collaboration by using electron scattering on ^{4}He to scan a Q_0^2-range from $0.5\,\mathrm{fm}^{-2}$ to $5.0\,\mathrm{fm}^{-2}$. These measurements were performed with two different spectrometers at energies of 450 MeV, 690 MeV and 795 MeV with overlapping Q_0^2-areas to reach a high level of redundancy. Measuring the investigated kinematic also with effectively reduced density inside the target cell opened the possibility to create a full target model for background subtraction. The data was analysed by using Monte-Carlo techniques and different parametrisations of the monopole resonance and the background to test model dependencies.
An indirect determination of the width of the monopole yields the intrinsic *full-width-at-half-maximum* (FWHM)

$$\Gamma_0 = 288 \pm 39 \text{ keV}$$

where radiative effects and energy loss of the scattered electron were taken into account by the simulation. This value with reduced uncertainty for Γ_0 confirms the existing values from [KOM$^+$83, Wal70].
The determined transition form factor $|\mathcal{F}_{M0^+}(Q_0^2)|^2$ is in agreement with existing data [FRC$^+$68, KOM$^+$83, Wal70] but shows a strongly improved precision over the whole Q_0^2-range of interest. Thus, the recent results in this thesis even stress the tension between *ab initio* predictions based on a χ-expansion [BBLO13] that deviate from the data by a factor two. The more precise data presented in this work opens now the opportunity for theorists to track the origin of these deviations and gain a deeper insight into Few-Body-Physics.

ZUSAMMENFASSUNG

Kernformfaktoren spiegeln fundamentale Eigenschaften von Kernen wieder, die gleichzeitig mit vielen anderen Größen eines Kerns zusammen hängen. Präzise Daten von Kernformfaktoren bieten die Möglichkeit theoretische Vorhersagen und Berechnungen von Kernstruktur zu überprüfen, wobei im speziellen die chirale Störungstheorie (χPT) in den vergangenen Jahren besonderes Interesse im wissenschaftlichen Arbeitsfeld auf sich zog.

Eine physikalische Größe die dabei speziell in den Fokus der Few-Body-Theorie gerückt ist, ist der Übergangsformfaktor des ^{4}He Kerns, berechnet mit χ-Potentialen einerseits [BBLO13] und bewährten phänomenologischen Potentialen [HGK04] andererseits. Diese Berechnungen beinhalten Terme von 3-Körperkräften und führen zu teils sehr unterschiedlichen Resultaten die Stärke des Übergangs der Monopolresonanz betreffend. Die experimentelle Datenlage des Übergangsformfaktors reicht teilweise über 50 Jahre zurück und weist dementsprechend hohe Unsicherheiten und große Fehlerbalken auf, was eine glaubwürdige Verifizierung bestehender Modelle nicht ermöglicht.

Um die Datenlage des Übergangsformfaktors der Monopolresonanz $|\mathcal{F}_{M0^+}(Q_0^2)|^2$ zu verbessern wurde in der A1 Kollaboration ein Elektronenstreuexperiment an ^{4}He durchgeführt um den Q_0^2-Bereich von $0.5\,\mathrm{fm}^{-2}$ bis $5.0\,\mathrm{fm}^{-2}$ zu überdecken. In diesem Experiment wurden zwei verschiedene Spektrometer verwendet, wobei mit den Energien 450 MeV, 690 MeV und 795 MeV gemessen wurde um durch überlappende Q_0^2-Bereiche eine möglichst hohe Redundanz zu erzielen. Die untersuchten Kinematiken wurden mit Messungen an einer praktisch leeren Targetzelle ergänzt, um ein Modell zu entwickeln, dass den Untergrund der Targetzelle simuliert. Die Daten wurden mit Monte-Carlo Methoden analysiert, wobei verschiedene Parameterisierungen zum Beschreiben der Monopolresonanz sowie des Untergrunds untersucht wurden, um die Resutate auf Modellabhängigkeiten zu testen.
Eine indirekte Bestimmung der Breite des Monopols ergab für den Wert der intrinsischen *vollen Halbwertsbreite* (FWHM)

$$\Gamma_0 = 288 \pm 39 \text{ keV}$$

wobei Strahlungskorrekturen und Energiverlust des Elektrons beim Streuprozess in der Simulation berücksichtigt wurden. Dieser Wert für Γ_0 mit kleinerer Unsicherheit bestätigt die Werte von [KOM+83, Wal70]. Der erhaltenene Übergangsformfaktor $|\mathcal{F}_{M0^+}(Q_0^2)|^2$ ist in guter Übereinstimmung mit den Daten von [FRC+68, KOM+83, Wal70] mit jedoch deutlich

verbesserter Präzision über den ganzen betrachteten Q_0^2-Bereich. Dadurch wird die Diskrepanz der jüngsten Ergebnisse zu den *ab initio* Berechungen basierend auf einer χ-Entwicklung zusätzlich bestärkt, welche etwa einen Faktor zwei zu den Daten abweichen. Die genaueren Ergebnisse des Übergangsformfaktors, die in dieser Arbeit vorgestellt werden, eröffnen Theoretikern die Möglichkeit, den Ursprung dieser Abweichungen aufzuspüren und einen tieferen Einblick in die Few-Body-Physik zu gewinnen.

CONTENTS

1

INTRODUCTION

The question for the origin and structure of matter can be traced back to Greek philosophers like Leukipp or Demokrit. Their established concepts of very small, non-divisible particles, founded purely on observations like the wear of frequently climbed stone stairs, have influenced our view of the microscopic world for a long time. Even if, from our modern point of view, the ideas seem incomplete, their pioneering thoughts were honored by preserving the name of the so called *atomos*.

It took then more than 2000 years to deepen our insight into the structure of matter: with the postulate of a very dense nucleus, concentrating nearly the entire mass of an atom, Ernest Rutherford [F.R11] falsified all previous predictions of atomic structure by scattering of α-particles on thin foils of gold. The discovery of the neutron by James Chadwick [J.C32] completed Rutherfords model. Many puzzles were solved, but likewise others emerged: what keeps two protons together - on a size-scale beyond all limits of imagination ? Why do chemical elements have different isotopes ?
On the other hand, astonishing phenomena like the association of wave attributes to electrons by Louis de Broglie [Bro25] lead to head-shaking among the physicists of that time. With the postulate of Erwin Schrödinger's famous equation [Sch26], the new domain of quantum physics got its theoretical foundation in the non-relativistic regime. Later it was expanded by Paul Dirac [Dir28] to a Lorentz-invariant and relativistic framework.
Finally, due to the development of particle accelerators and colliders with permantently increasing energy scince the 1930s, the subnucleonic particle spectrum is accessible nowadays. Our understanding of fundamental interactions is presently compiled in the Standard Model, in which twelve gauge-bosons are responsible for the electromagnetic, the weak and the strong interaction. The theory of electromagnetic interaction has already proven to be accurate and can be unified with the weak interaction in the high energy limit. Quantum chromodynamis (QCD) is the underlying theory of strong interaction: its validity is often split into two domains - a high energy, perturbative regime with asymptotically free quarks, and the non-perturbative regime with quarks confined into hadrons.
If, according to confinement, in the QCD Lagrangian the elementary degrees of freedom (quarks and gluons) are replaced by complex hadrons, convergence is not valid any more and this hinders a theoretical description of the nucleus. A solution is offered by chiral perturbation theory (χPT), an effective field theory

(EFT) conserving the chiral symmetry of QCD. In χPT light mesons, such as pions, mediate the interaction between nucleons. This interaction is usually organised in power counting schemes, excluding those diagrams that do not respect symmetry. The strength of the terms in this power counting scheme is regulated by low-energy-constants (LEC) with initially unknown values that have to be adjusted to experimental data or must be derived from another theoretical context.

The procedure of using an effective approach for interactions on the nuclear level has already shown remarkable success. ^{12}C exhibits an excited 0^+-state, also known as Hoyle-state, that plays a key-role in the fusion-cycle of stars and has thus an indirect influence on the formation of life. *Ab initio* calculations in the framework of EFT have shown agreement to experimental data by calculating the first excited states of ^{12}C and the Hoyle-state with increasing order in the power counting scheme [EKLM11].

Yet, another quantity showed that EFT is not an all-embracing solution for predictions of nuclear properties: ^{4}He posseses a narrow isoscalar resonance with same intrinsic quantum numbers as its ground state, located between the proton- and neutron break-up thresholds at an energy of 20.21 MeV. The transition form factor of this monopole resonance $|\mathcal{F}_{M0^+}(Q_0^2)|$ provides insight into nuclear dynamics and can serve as test for *ab initio* methods. Latest state-of-the-art *ab initio* calculations with χPT-potentials from Bacca et al. [BBLO13] show agreement of the form factor of the ^{4}He ground state to experimental data within a few percent, while the transition form factor of the monopole resonance shows a deviation of approximately a factor two (Fig. 1).

The results of calculations with established phenomenological potentials by Hiyama et al. [HGK04] show smaller deviation to the data, although the level of agreement to the data is hard to estimate due to large experimental uncertainties (see Fig. 1). The available data from electron scattering on ^{4}He, published by authors [FRC+68, KOM+83, Wal70], are almost 50 years old and show in-

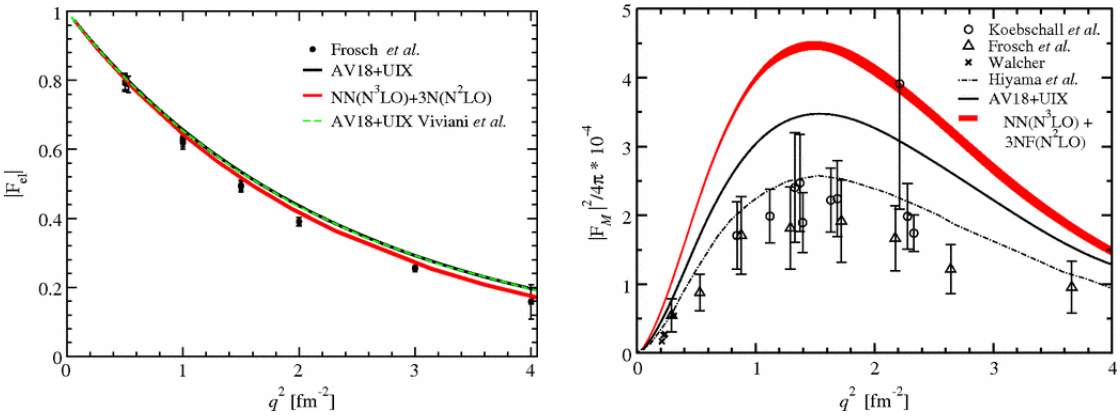

Figure 1: *(left)*: Various *ab initio* calculations for the ^{4}He ground state form factor including pion interactions up to N^3(LO) compared to experimental data from [FRC+68]. *(right)*: Same interactions for the monopole transition form factor and calculations from [HGK04] in comparison to data from [FRC+68, KOM+83, Wal70].

consistencies and large experimental uncertainties. The need of reliable data to stringently test the *ab initio* methods of χPT against results of established potentials led to the proposal for a new experiment.
This experiment was performed with the three-spectrometer setup of the A1 collaboration in Mainz. Electron scattering data were taken at forward scattering angles in a range from 16.3° to 36.8° at three different beam energies of 450 MeV, 690 MeV, and 795 MeV to achieve a high redundancy in the data by overlapping Q_0^2-ranges.
The scope of this work is to improve the experimental data over a Q^2-range from 0.5 fm^{-2} to 5.0 fm^{-2} and to determine the monopole transition form factor $|\mathcal{F}_{\mathrm{M0}^+}(Q_0^2)|^2$ with the highest achievable precision. Furthermore, other important properties of the monopole resonance of ^{4}He, such as the *full-width-at-half-maximum* Γ_0, the monopole matrix element ME, and transition radius $\mathcal{R}_{\mathrm{tr}}$ are extracted as well.

This thesis is organised as follows: After introducing the theoretical basics of resonances, form factors, and electron scattering in Chap. 2, the experimental setup of the A1 experiment is described with a focus on the detector system in Chap. 3. Subsequently, in Chap. 4 the calibration of the particular detector components is discussed. Chap. 5 details the background studies concerning the aluminium target cell. In Chap. 6 the transition form factor is determined relative to the elastic form factor of ^{4}He with an appoximate resonance parametrisation and omitting radiative corrections. Improved parametrisations and Monte-Carlo techniques to sample the monopole are outlined in Chap. 7. The determination of the width Γ_0 of the monopole is covered in Chap. 8, followed by the determination of the transition form factor of the monopole in Chap. 9. Chap. 10 provides a brief summary of the applied methods and obtained results and gives an outlook.

2

THEORETICAL FOUNDATIONS

2.1 NUCLEAR RESONANCES

One has to deal with fundamental properties of resonances to determine the transition form factor of the ^{4}He monopole. In the following, the basic features and concepts of resonant states are classified.

The theory of resonances is always linked to the term of "modes", an integer number of knots of a wave characterising a wave in resonance. The most intuitive picture of a resonance can be drawn from string instruments. A string, fixed at its end points and set in motion, creates an intrinsic note or pattern of notes of the system, described by certain frequencies. In quantum mechanics, this picture still holds for deep potential wells with wave numbers that are multiples of a fundamental wave number k_0. In nuclear systems, these analogies can at most serve as toy models, but still offer insight into resonance phenomena.
Resonance phenomena in nuclear physics were discovered and studied by e.g. Breit and Wigner [BW36], using predominantly nucleon-nucleus scattering rather than electron scattering. A fundamental difference of resonances compared to excited states is that resonances have a (central) energy E_0 larger than the minimal separation energy S_{min} to knock a nucleon out off the nucleus. Thus, resonances are located in the continuum and decay preferentially by particle emission, while excited states decay into states of lower energy by selection rules.
To give a brief theoretical introduction to resonances, we follow the approach of J. M. Blatt and V. F. Weisskopf [JMB79] that derive the features of resonances in the context of nucleon-nucleus scattering. The basic difference to electron scattering is that a nucleon has to enter the nucleus with an appropriate energy to create the resonant state in the compound nucleus (in the case of electron scattering, a bound nucleon inside the nucleus receives the energy from the virtual photon to form the resonance). For simplification it is assumed, that only a single nucleon n_r is responsible for the resonance when entering the compound nucleus N_r. The compound nucleus N_r decays only via a single mode α by emitting an identical nucleus n_r. The wave function of n_r inside the nucleus can be assumed as a superposition of an in- and outgoing wave with equally strong amplitudes:

$$u_{\text{in}} \propto \exp(-iKr) + \exp(i(Kr + 2\xi(\epsilon))) = 2\exp(i\xi(\epsilon))\cos(Kr + \xi(\epsilon)) \quad (1a)$$
$$u_{\text{out}} \propto \sin(kr + \delta) \quad (1b)$$

here, K is the wave number of n_r inside the nucleus and $\xi(\epsilon)$ the energy dependent phase shift. This phase shift depends on nuclear properties and the interactions the nucleon n_r undergoes before leaving the compound nucleus. This means, in contrast to a bound state, the nucleon enters and escapes from the compound system, as long as its wave number and energy corresponds to the resonance. Consequently, n_r is loosely bound and in motion with the other nucleons. The following conditions hold for the wave function of the nucleon n_r inside N_r to escape from the compound nucleus if only the part dependent on r is considered:

1. To escape the compound nucleus, the nucleon's wave function needs to have a large amplitude at $r = R$.
2. The wave function and the derivative need to coincide at $r = R$: $u_{\text{in}}(R) = u_{\text{out}}(R)$, $u'_{\text{in}}(R) = u'_{\text{out}}(R)$.

Three cases can now be distinguished (Fig. 2): If the energy of the nucleon inside the nucleus is not close to resonance energy or does not have the matching phase shift $\xi(\epsilon)$, the particle remains inside the nucleus. The second case is approaching the resonant state, and in the third case, if both wave functions match with their maximum at the nuclear surface R, the nuclear state is in resonance and n_r will more likely escape from the compound nucleus.
The energy dependent phase shift is strongly related to the nuclear interaction inside the nucleus and all its components. The difference between electron and nucleon scattering is the type of interaction, where in the electromagnetic case a virtual photon with momentum $\vec{q}$ is interchanged with a nucleon n_r aready inside the nucleus. For nucleon scattering, the projectile target is repelled or absorbed at the nuclear surface, and, after absorption, reemitted within finite time[1]. Both these interactions come with other competing processes, but have in common, that inside the nucleus n_r experiences a repetition of motion, that causes the finite lifetime of the resonance state. This, in analogy to atomic phenomena, leads together with Heisenbergs uncertainty relation to the connection between energy uncertainty and lifetime of the resonant state:

$$\Delta\tau\Delta E \approx \hbar \quad (2)$$

1 Projectiles with more than one nucleon are of course also possible.

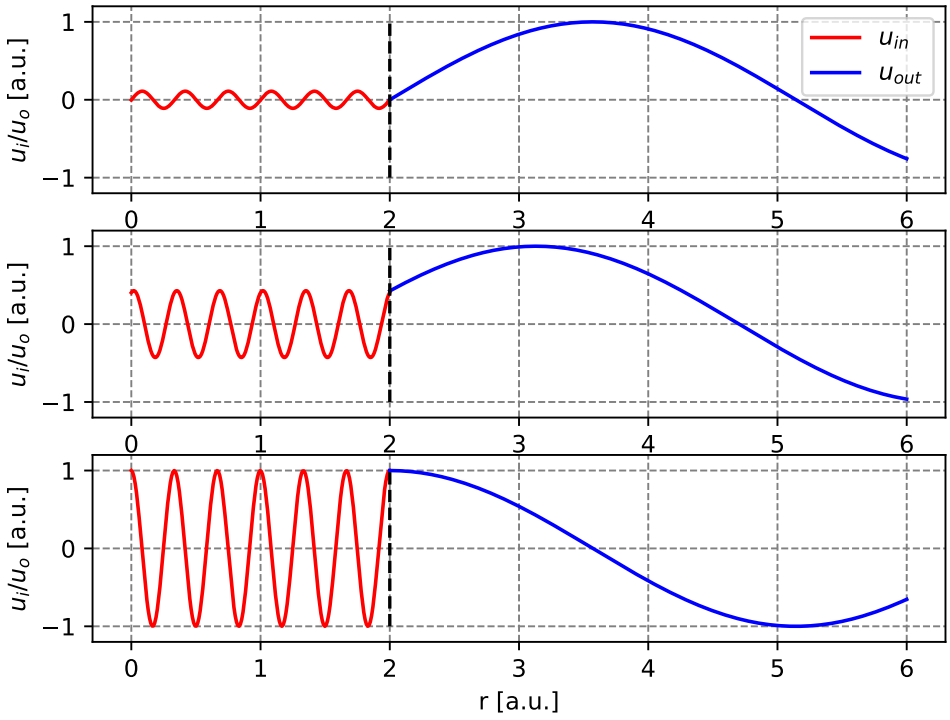

Figure 2: The wave functions of a nucleon interacting with a nucleus for three cases. *(top):* The energy of the nucleon n_r does not have the appropriate value to form a resonant state. *(middle):* The energy of n_r approaches the matching energy. *(bottom):* A resonant state is formed with matching wave number K of nucleon n_r inside the compound nucleus.

Thus, the resonance has a width Γ_0 which is connected to its lifetime τ_0 in the following way:

$$\Gamma_0 = \frac{\hbar}{\tau_0} \tag{3}$$

The value of Γ_0 can be composed from different widths $\Gamma^{(i)}$ of several decay channels with different branching ratios. In analogy to dispersion phenomena from other fields of physics, the energy dependent cross section of a nuclear resonance can be written in the following representation:

$$\left(\frac{d\sigma}{dE}\right) = \frac{1}{2\pi}\frac{\Gamma_0}{(E - E_0) + \frac{\Gamma_0^2}{4}} \tag{4}$$

This formula is better known as Breit-Wigner formula and applies to resonance phenomena in nuclear pyhsics in general and in particular. It describes an energy distribution around a central energy E_0 with a width Γ_0. The common convention is to use Γ_0 as *full-width-at-half-maximum* (FWHM), and normalise the distribution accordingly. This convention will be used if not specified otherwise.

2.2 INVESTIGATION OF NUCLEAR STRUCTURE

Nuclear structure can be investigated in many ways, with electron scattering offering the most advantageous possibility.
If an electron interacts with a nuclear system with a particle-wavelength λ comparable to the size of this system, it can probe its structure by exchange of virtual photons. These processes rely solely on the electromagnetic interaction, which is a well understood and confirmed theory.
Observables that describe the kinematic in electron scattering experiments are given in the formalism of four-vectors. In the laboratory system, the target with mass M is at rest, and the scattering process can be illustrated by Fig. 3. The notation of the used four-vectors is shown in Tab. 1:

Observable	Notation	Four-vector
init. electron four-momentum	k_i	$k_i = \{E_i, \vec{k_i}\}$
final electron four-momentum	k_f	$k_f = \{E_f, \vec{k_f}\}$
transfered four-momentum[2]	q	$q = k_f - k_i$
init. target four-momentum	K_i	$K_i = \{M, 0, 0, 0\}$
final target four-momentum	K_f	$K_f = \{E^*, \vec{K_f}\}$

Table 1: Momentum four-vectors of kinematical observables in this analysis.

An important quantity derived from the observables in Tab. 1 is the squared four-momentum[2] $q^2 = q_\mu q^\mu$ of the virtual photon

$$q^2 \simeq -4E_i E_f \sin^2 \frac{\theta}{2} \tag{5}$$

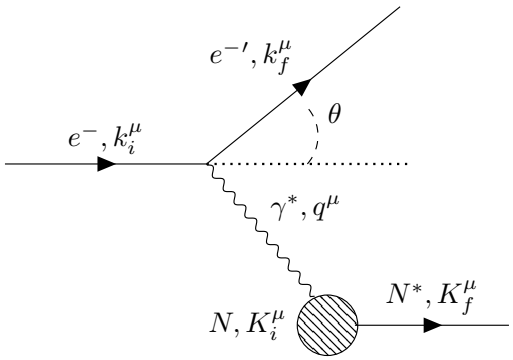

Figure 3: Electron scattering at angle θ on a target nucleus at rest. The virtual photon γ^* transfers the four-momentum q. The final nucleus momentum is not measured in an inclusive measurement, where the final nucleus N^* can be in an excited state or undergo other inelastic processes.

2 If not required, we omit the greek indices of four-vectors. If $q = |\vec{q}|$ it will be noted explicitly.

with scattering angle θ, initial and final electron energy E_i and E_f. For convenience $Q^2 = -q^2$ is defined as negative of the squared four-momentum. If unpolarised, elastic cross sections are investigated, the experimental cross section depends only on E_i, θ, and Q^2:

$$\left(\frac{d\sigma}{d\Omega}\right)_{\text{Mott}} = \frac{(2Z\alpha E_f \cdot \cos\frac{\theta}{2})^2}{Q^4}\frac{E_f}{E_i} = \frac{(Z\alpha \cdot \cos\frac{\theta}{2})^2}{(2E_i \cdot \sin^2\frac{\theta}{2})^2}\frac{E_f}{E_i} \tag{6a}$$

with final electron energy

$$E_f = \frac{E_i}{1 + \frac{2E_i}{M_T}\sin^2\frac{\theta}{2}} \quad . \tag{6b}$$

Here, $(d\sigma/\,d\Omega)_{\text{Mott}}$ is the Mott cross section with a recoil correction term E_f/E_i for a point-like particle with charge Z. With our advanced understanding of nuclear matter we know, that nuclei and nucleons have an internal structure. This deviation of point-like particles leads to the introduction of form factors $\mathcal{F}(Q^2)$,

$$\left(\frac{d\sigma}{d\Omega}\right)_{\text{exp}} = \left(\frac{d\sigma}{d\Omega}\right)_{\text{Mott}} \cdot |\mathcal{F}(Q^2)|^2 \tag{7}$$

that can be regarded as a correction applied to the Mott cross section. Form factors are Fourier transforms of quantities that are related to the internal structure or dynamics of a nucleus. A prominent example of such a Fourier pair is the elastic form factor $\mathcal{F}_{\text{el}}(Q^2)$ and the charge density $\rho(\vec{r})$ of a nucleus,

$$|\mathcal{F}_{\text{el}}(Q^2)|^2 \propto \left| \int \exp^{i\vec{q}\vec{r}} \cdot \rho(\vec{r})\, d\vec{r} \right|^2 \tag{8a}$$

where

$$\rho(\vec{r}) = \langle \Psi_0 | \frac{1}{A} \sum_{i=1}^{A} \delta(\vec{r} - \vec{r}_j) | \Psi_0 \rangle \quad , \tag{8b}$$

with nucleon number A and ground-state wave function Ψ_0.
Since the determination of a form factor by experimental techniques is limited to the accessible range of Q^2, the common approach is to calculate $\rho(\vec{r})$ using (8b) with a realistic nuclear Hamiltonian $\hat{H}$ and obtain the form factor by Fourier transformation, which is then compared to the experiment. In Fig. 4 elastic form factors and related charge density distributions are shown for various nuclei. For heavier nuclei, the charge density exhibits a plateau for $r < c$, where c is the *half-density radius*. Light nuclei like ^{4}He form an exception, with a large density of nuclear matter at small r, but a very diffuse fringe. If the nuclear charge was concentrated in a point-like charge, no diffraction effects would be observed and the form factor would be constant.

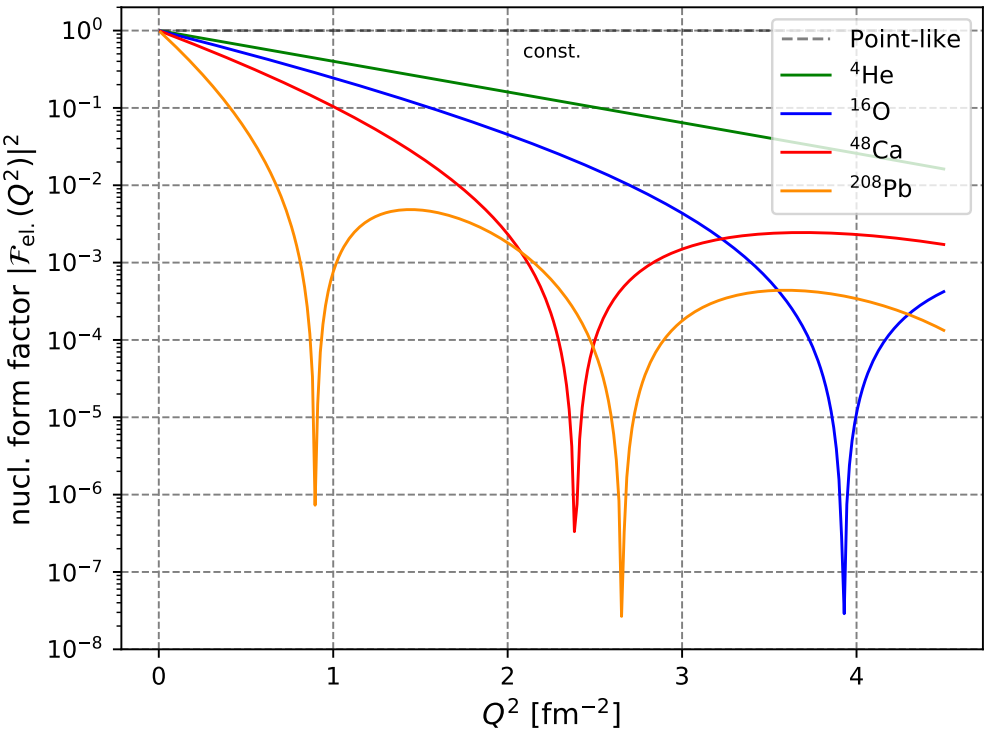

(a)

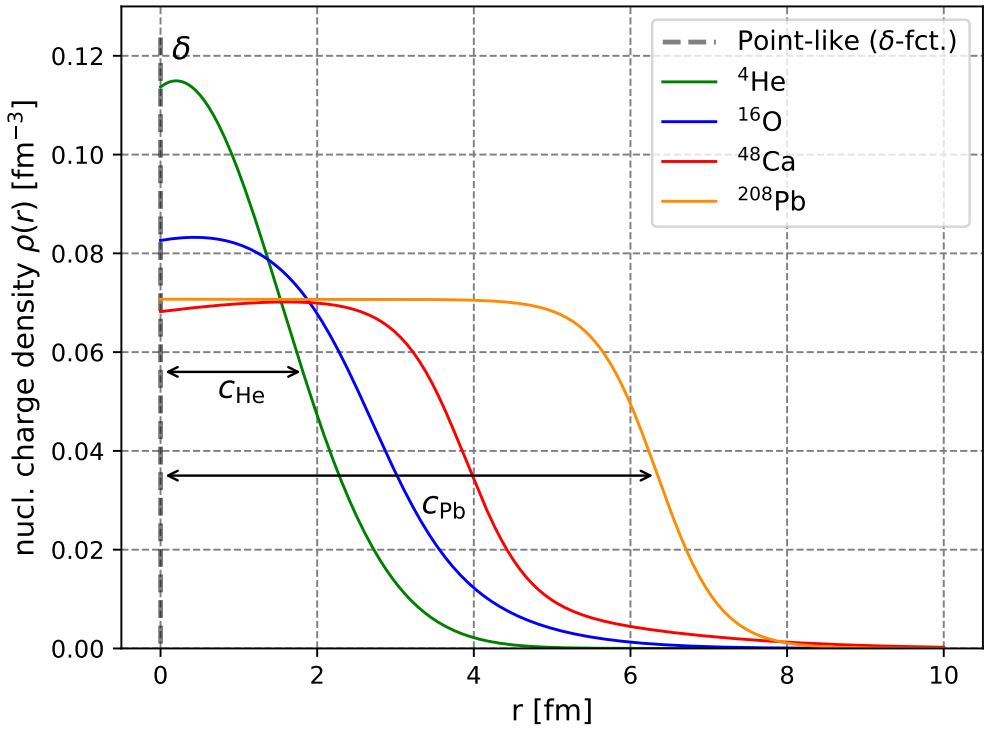

(b)

Figure 4: Schematic form factors of various nuclei *(a)* with their related charge densities *(b)*. The diffraction minima appear very sharp for heavier nuclei. Light nuclei like ^{4}He are an exception with their Gaussian-shaped form factor and charge density distribution. A point-like particle would have a constant form factor and thus a δ-function as charge density.

2.3 MONOPOLE TRANSITION FORM FACTOR OF ^{4}HE

As outlined in Sec. 2.2, form factors reveal informations about a nuclear system and its dynamics. As an example, the elastic form factor $\mathcal{F}_{\text{el}}(Q^2)$ can be determined by the wave function of the ground state Ψ_0 and the charge density operator (see (8a) and (8b)). For the resonant state, the situation is slightly more challenging. The monopole resonance is a quasi-bound state located between the proton- and neutron threshold of the ^{4}He continuum which decays into a continuum state, different from the ground state. The strength to excite the resonance is given by the response function [BBLO13]

$$|\mathcal{R}_M(\omega, q)| = \sum\!\!\!\!\!\!\int_n dn \left| \langle \Psi_n | \mathcal{M}(q) | \Psi_0 \rangle \right|^2 \delta(\omega - E_n + E_0) \tag{9}$$

with energy ω transferred by the electromagnetic probe, three-momentum transfer $q = |\vec{q}|$ and the isoscalar monopole operator

$$\mathcal{M}(q) = \frac{G_E^s(q)}{2} \sum_{i=1}^{4} j_0(qr_i) \tag{10}$$

where $G_E^s(q) = G_E^p(q) + G_E^n(q)$ is the nucleon electric isoscalar form factor, r_i the position of the nucleon and $j_0(qr_i)$ the spherical Bessel function of 0^{th} order. The integral sum in (9) runs over all continuum states n with energy E_f while the δ-function ensures energy conservation. Thus, solving (9) for the response function $\mathcal{R}_M(\omega, q)$ requires not only the solution for the ground state Ψ_0, but also for the continuum few-body problem Ψ_f.
The use of the Lorentz integral transform (LIT) is a method that circumvents the explicit calculation of Ψ_f, [LEI09]. The equation for the LIT reads as

$$\mathcal{L}(\omega_0, \Gamma, q) = \int d\omega \, K(\omega, \omega_0, \Gamma) \cdot \mathcal{R}_M(\omega, q) \tag{11a}$$

where

$$K(\omega, \omega_0, \Gamma) = \frac{\Gamma}{\pi} \frac{1}{(\omega - \omega_0)^2 + \Gamma^2} \tag{11b}$$

is the integral kernel. Similar to the Breit-Wigner[3] distribution, ω_0 represents a central energy value and Γ an energy resolution. Combining (9) and (11) we get

$$\mathcal{L}(\omega_0, \Gamma, q) = \int d\omega \sum\!\!\!\!\!\!\int_n K(\omega, \omega_0, \Gamma) \left| \langle \Psi_n | \mathcal{M}(q) | \Psi_0 \rangle \right|^2 \delta(\omega - E_n + E_0) \tag{12a}$$

where integration over ω yields

$$\mathcal{L}(\omega_0, \Gamma, q) = \sum\!\!\!\!\!\!\int_n K(E_n - E_0, \omega_0, \Gamma) \, \langle \Psi_0 | \mathcal{M}(q)^\dagger | \Psi_n \rangle \, \langle \Psi_n | \mathcal{M}(q) | \Psi_0 \rangle \tag{12b}$$

3 NB: the normalisation is different to (4) due to a different definition of Γ

With $\hat{H}\,|\Psi_n\rangle = E_n\,|\Psi_n\rangle$ one can replace the final energy E_n with the Hamiltonian of the interaction $\hat{H}$ in the kernel function:

$$\mathcal{L}(\omega_0,\Gamma,q) = \frac{\Gamma}{\pi}\sum\!\!\!\!\!\!\int_n \frac{\langle\Psi_0|\mathcal{M}(q)^\dagger|\Psi_n\rangle\,\langle\Psi_n|\mathcal{M}(q)|\Psi_0\rangle}{(E_n - E_0 - \omega_0 + \Gamma)(E_n - E_0 - \omega_0 - \Gamma)} \tag{12c}$$

$$\begin{aligned}\mathcal{L}(\omega_0,\Gamma,q) = \frac{\Gamma}{\pi}\sum\!\!\!\!\!\!\int_n \langle\Psi_0|\mathcal{M}(q)^\dagger(\hat{H} - E_0 - \omega_0 + i\Gamma)^{-1}|\Psi_n\rangle\cdot \\ \langle\Psi_n|(\hat{H} - E_0 - \omega_0 - i\Gamma)^{-1}\mathcal{M}(q)|\Psi_0\rangle\end{aligned} \tag{12d}$$

To integrate (12d), one can use the closure relation $\sum\!\!\!\!\!\!\int |\Psi_n\rangle\,\langle\Psi_n| = 1$ and reduce the Lorentz-integral to an expectation value of the ground state:

$$\begin{aligned}\mathcal{L}(\omega_0,\Gamma,q) = \frac{\Gamma}{\pi}\langle\Psi_0|\mathcal{M}(q)^\dagger(\hat{H} - E_0 - \omega_0 + i\Gamma)^{-1} \\ (\hat{H} - E_0 - \omega_0 - i\Gamma)^{-1}\mathcal{M}(q)|\Psi_0\rangle\end{aligned} \tag{13}$$

Solving (13) is possible with bound state techniques and does not require the calculation of scattering state wave functions Ψ_n. The resolution parameter Γ is fixed for a set of n basis functions. To obtain $\mathcal{R}(\omega,q)$, the calculation of (13) is repeated for a range of ω_0, that is determined by $\omega_{\min} - \Gamma \leq \omega_0 \leq \omega_{\max} + \Gamma$, where $\omega_{\min}$ and $\omega_{\max}$ confine the area of interest in the response function. The inversion of $\mathcal{L}(q,\omega_0,\Gamma)$ is often performed in a set of basis functions with linear parameters to be determined. Once $\mathcal{R}(\omega,q)$ is given, the monopole transition form factor can be obtained by

$$|\mathcal{F}_{\mathrm{M}}(q^2)|^2 = \frac{1}{Z^2}\int d\omega \mathcal{R}_M(\omega,q) \tag{14}$$

Several benchmark tests have been made for the LIT, showing the great success of the method. Other approaches of ab-initio calculations of the monopole transition form factor solve the wave function with bound-state boundary conditions and phenomenological three-body forces [HGK04]. The outcome of the different calculation methods does not only differ in the transition form factor, but also in quantitites sensitive to it. For instance, it has been argued over, e.g. if the resonance structure has to be considered as *breathing mode* [BBLO15] or a loosely bound $3N + N$ system [HGK04].

Physical observables in electromagnetic processes are usually derived or calculated in *Plane-Wave-Born-Approximation* (PWBA), a perturbative method to describe scattering processes on electromagnetic potentials.
The key assumption of PWBA is that initial and final particles are described by plane waves of the form

$$\Psi_{i,f} = \frac{1}{\sqrt{V}} e^{i\vec{k_{i,f}}\vec{x}/\hbar} \tag{15}$$

within a large but finite volume V and wave numbers $\vec{k}_i, \vec{k}_f$, where the momentum transfer is written as $\vec{q} = \vec{k}_i - \vec{k}_f$. The validity of the Born approximation is restricted to $Z\alpha \ll 1$ with the Sommerfeld constant $\alpha \approx 1/137$. Higher order approximations, like two-photon exchange (see Fig. 5), contribute to the perturbative series in $(Z\alpha)^2$. The photon-exchange processes are usually organised by power counting. If higher-order terms are considered, the expansion of the series can get cumbersome very quickly. Still, for terms like the emission of hard or soft photons leading to the radiative corrections of electron scattering, calculations, which are used in this analysis, have been made by M. Vanderhaeghen et al. [VFL+00]. Higher order terms, like the mentioned two-photon exchange, require to completely take into account the internal structure of the nucleus. These orders are not included in the scope of this analysis because they are relatively small and as yet unknown.

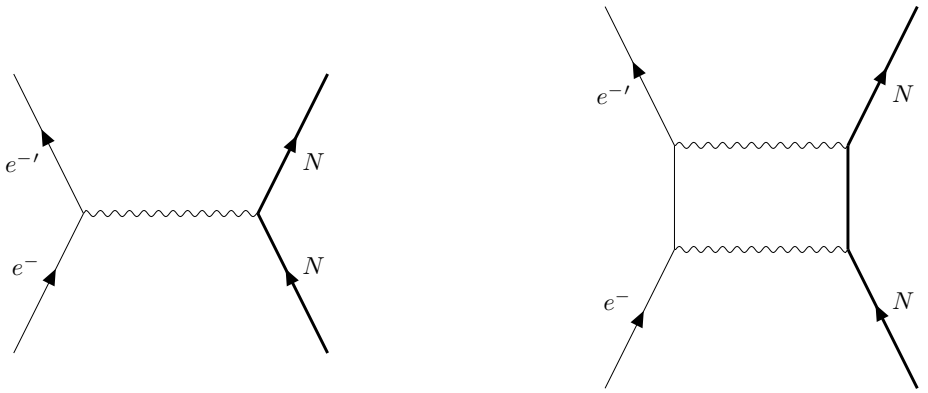

(a) (b)

Figure 5: One- and two-photon exchange in Born approximation.

Radiative corrections are applied to the experimental cross section as a factor consisting of several terms. As a result we write the experimental cross section as

$$\left(\frac{d\sigma}{d\Omega}\right)_{exp} = \left(\frac{d\sigma}{\Omega}\right)_0 (1+\delta) \tag{16}$$

in which δ is the sum of all radiative effects applied to the Born cross section:

$$\delta = \delta_{vac} + \delta_{vertex,e} + \delta_{rr,e} + \delta_1^Z + \delta_2^{Z^2} \quad , \tag{17}$$

with δ_{vac} the correction for vacuum polarisation, $\delta_{vertex,e}$ the electron-vertex correction, $\delta_{rr,e}$ the correction for initial- and final-state-radiation and δ_1^Z and $\delta_2^{Z^2}$ for easily applicable hadronic corrections. To approximately take into account higher orders, δ is exponentiated, except for the vaccuum polarisation, which is given by an approximated form in the denominator[4]:

$$\left(\frac{d\sigma}{d\Omega_{exp}}\right) \approx \left(\frac{d\sigma}{\Omega_e}\right)_0 \cdot \frac{e^{\delta_{vertex,e}+\delta_{rr,e}+\delta_1^Z+\delta_2^{Z^2}}}{(1-\delta_{vac}/2)^2} \quad . \tag{18}$$

The terms of the particular radiative processes contributing to δ and that are included in the analysis are outlined in the following, the recipes to calculate such corrections are given in [VFL+00], [MT00].

2.4.1 *Vacuum polarisation*

An important term is the vacuum polarisation, also called photon-loop or photon self-energy. The associated Feynman diagram is shown in Fig. 6. If we follow the approach of [VFL+00], the correction factor of the vacuum polarisation can be written as

$$\delta_{vac} = \frac{\alpha}{\pi}\frac{2}{3}\left\{\left(v_e^2 - \frac{8}{3}\right) + v_e\frac{3-v_e^2}{2}\ln\left(\frac{v_e+1}{v_e-1}\right)\right\} \tag{19a}$$

which becomes

$$\delta_{vac} = \frac{\alpha}{\pi}\frac{2}{3}\left\{-\frac{5}{3} + \ln\left(\frac{Q^2}{m_e^2}\right)\right\} \quad \text{as} \quad Q^2 \gg m_e^2 \tag{19b}$$

with

$$v_e = 1 + \frac{4m_e^2}{Q^2} \quad . \tag{19c}$$

In equation (19b) the ultrarelativistic limit is taken into account. Both, e^--e^+- and μ^--μ^+-pairs contribute to this loop, which can be included by exchanging m_e with m_μ in (19c). However, the μ^--μ^+ contribution is very small and in our kinematics negligible.

4 In the article [VFL+00] of Vanderhaeghen et al. it is shown, that this approximation is very accurate.

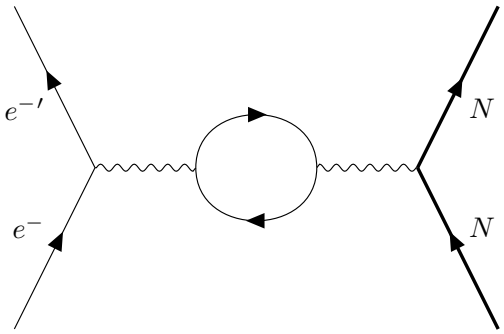

Figure 6: The Feynman diagram for the vaccum polarisation.

2.4.2 *Electron vertex correction*

The on-shell photon-electron-electron vertex diagram is shown in Fig. 7.
This diagram contains two divergent parts in the ultraviolet and infrared limits, which have to be compensated by counterterms. In the ultrareltivistic limit as in equation (19b), the correction term $\delta_{vertex,e}$ becomes

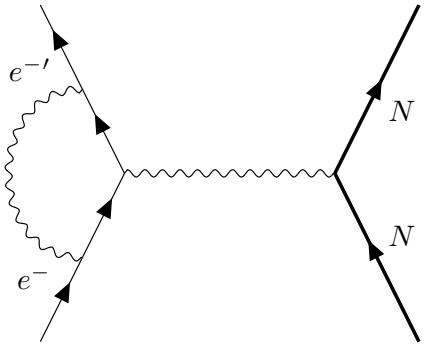

Figure 7: Feynman diagram of the electron vertex correction.

$$\delta_{vertex,e} = \frac{\alpha}{\pi}\left\{\frac{3}{2}\ln\left(\frac{Q^2}{m^2}\right) - 2 - \frac{1}{2}\ln^2\left(\frac{Q^2}{m^2}\right) + \frac{\pi^2}{6}\right\} \quad . \tag{20}$$

The quadratic logarithmic term in (20) shows, that the vertex correction is relatively large compared to other contributions of the radiative corrections.

2.4.2.1 *Initial- and final state radiation*

Initial-State-Radiation (ISR) and *Final-State-Radiation* (FSR) describe the processes of the electron emitting real photons, before (ISR) or after (FSR) an interaction with the nuclear electromagnetic field. In Fig. 8 the Feynman diagrams of these two processes are shown. The correction δ_{rr} is split in two parts with

$$\delta_{rr} = \delta^0_{rr,e} + \delta^1_{rr,e}(\Delta E'_{e,max}) \tag{21a}$$

with

$$\delta^0_{rr,e} = \frac{\alpha}{\pi}\left\{-\frac{1}{2}\ln^2\eta + \frac{1}{2}\ln^2\left(\frac{Q^2}{m_e^2}\right) - \frac{\pi^2}{3} + Sp\left(\cos^2\frac{\theta_e}{2}\right)\right\} \quad , \tag{21b}$$

$$\delta^1_{rr,e}(\Delta E'_{e,max}) = \frac{\alpha}{\pi}\left[\ln\left(\frac{Q^2}{m^2}\right) - 1\right] \cdot \ln\left(\frac{(\eta\Delta E'_{e,max})^2}{E_e \cdot E'^{el}_e}\right) \quad , \tag{21c}$$

where

E'^{el}_e is the energy of elastically scattered electron without photon emission,

E'_e is the energy of elastically scattered electron with photon emission,

$\Delta E'$ is the energy distribution following radiative tail characteristics,

$\eta = E_e / E'^{el}_e \geq 1$ and

$Sp(t) = -\int_0^t dt' \, \frac{\ln(1-t)}{t}$ is the dilogarithmic- or Spence function.

Here, $\Delta E'_{e,max}$ is a parameter that is determined by detector properties or analytical cuts, i.e. , the maximum allowed value of the scattered electron with included radiative corrections. Another quadratic logarithmic term similar to the one in (20) makes this correction fairly large.

2.4.3 *Hadronic corrections*

In general, the radiative corrections on the hadron side are suppressed compared to leptonic radiative corrections due to considerably larger mass of the hadron. Also, some of the hadron terms for radiative corrections are not model-independent and related to the internal structure of the nucleus, thus one must take into account the charge form factors.
For simulations in this analysis the hadron correction calculated by L.C. Maximon [MTo0] containing three parts is used:

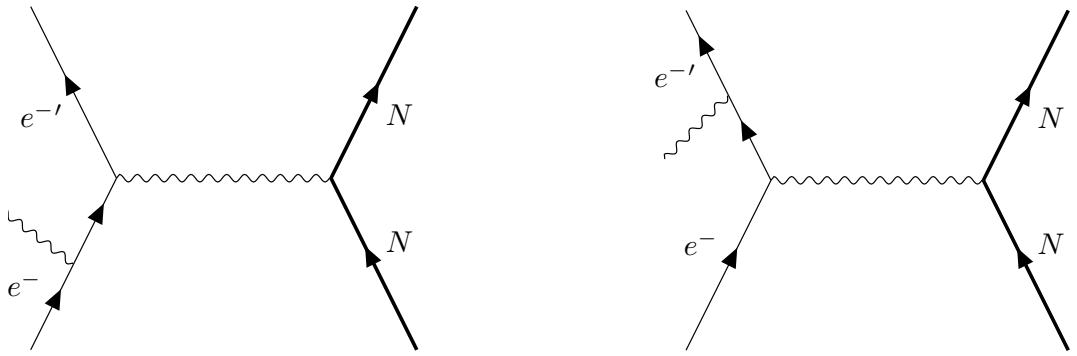

Figure 8: Feynman diagrams of ISR and FSR leading to the emission of real photons from the electron.

$$\delta_{h,rr} = \delta_1^{(Z)} + \delta_2^{(Z^2)} + \delta_{el}^{(1)} \tag{22a}$$

with

$$\delta_1^{(Z)} = \frac{2\alpha Z}{\pi}\left\{\ln\eta\ln\left(\frac{4(\eta\Delta E'_{e,max})^2}{Q^2x}\right) + Sp(1-\frac{\eta}{x}) - Sp(1-\frac{1}{\eta x})\right\} \tag{22b}$$

and

$$\begin{aligned}\delta_1^{(Z)} = \frac{2\alpha Z^2}{\pi}\Bigg\{&1+\ln\left(\frac{4(\eta\Delta E'_{e,max})^2}{M^2}\right)\left(\frac{E'_N}{|\vec{p}'_N|}\ln x - 1\right) + \\ &+ \frac{E'_N}{|\vec{p}'_N|}\left[-\frac{1}{2}\ln^2 x - \ln x\ln\left(\frac{\rho^2}{M^2}\right) + \ln x - Sp\left(1-\frac{1}{x^2}\right) + \right. \\ &\left. + 2\cdot Sp\left(-\frac{1}{x}\right) + \frac{\pi^2}{6}\right]\Bigg\}\ ,\end{aligned} \tag{22c}$$

where

$\vec{p}'_N$ is the final hadron momentum,

E'_N is the final hadron energy,

M is the hadron rest mass,

$x = \frac{(Q^2+\rho)^2}{4M^2}$ and

$\rho = \sqrt{Q^2+4M^2}$.

The term $\delta_{el}^{(1)}$ includes the internal structure of the hadron, but it is very small compared to $\delta_1^{(Z)}$ and $\delta_2^{(Z^2)}$. Due to its difficult calculation and the small benefit in accuracy, it is neglected in the hadronic radiative corrections.
The Feynman diagrams related to these corrections are shown in Fig. 9. Hadron structure dependent terms to these diagrams were neglected.

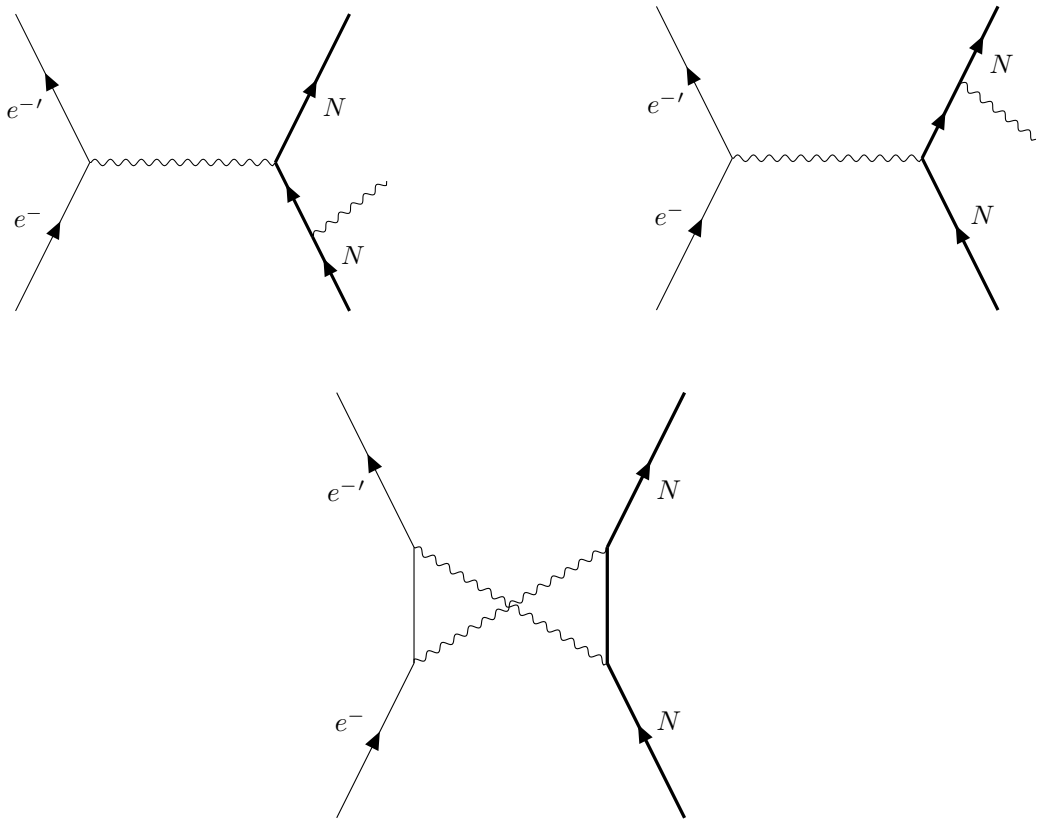

Figure 9: Feynman diagrams of the hadronic radiative corrections. The two photon box diagram also included is shown in Fig. 5.

All radiative corrections described in the previous pages are taken into account in Monte-Carlo simulations of this analysis. Fig. 10a shows δ_i for each correction term described above for electrons scattered on ^{4}He and the entire correction applied to the cross section $(d\sigma/d\Omega)_0$ as dependent on Q^2 (Fig. 10b). It can be seen in Fig. 10b, that the application of these corrections can have a strong influence on the determined cross sections, especially at higher Q^2, making these corrections indispensable.

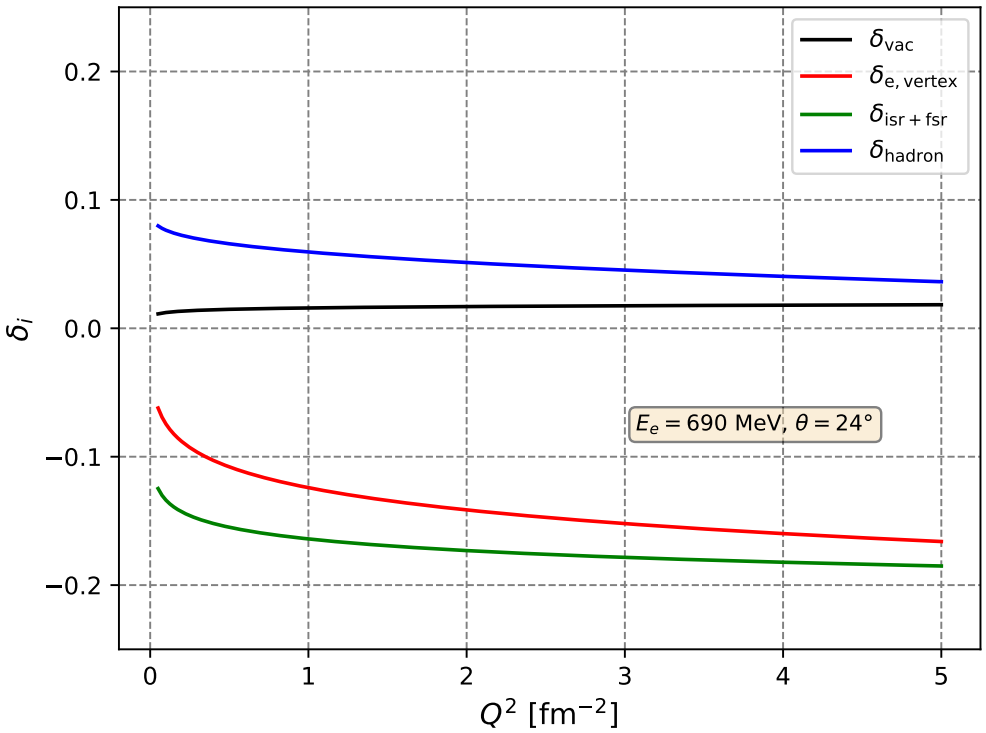

(a)

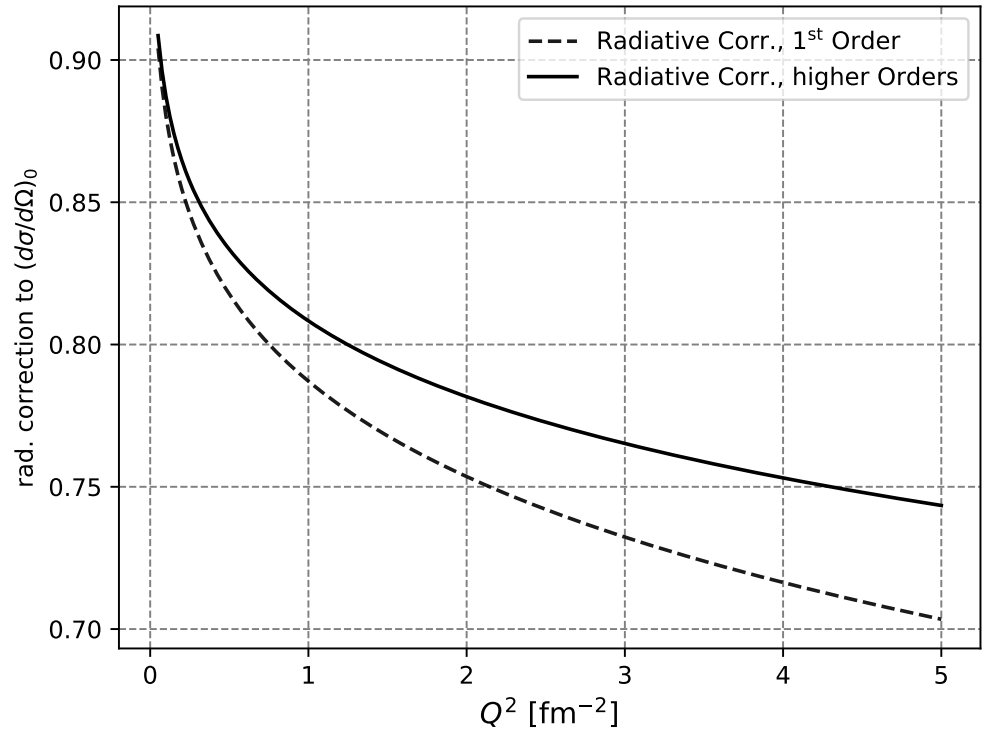

(b)

Figure 10: Radiative corrections. *(a)*: δ_i for the particular contributions of the radiative corrections of a typical kinematic. *(b)*: the radiative corrections as entire factor multiplied to the experimental cross section, as 1st order (17) and higher orders (18).

3

EXPERIMENTAL SETUP

3.1 MAINZ MICROTRON

The experiment has been performed at the MAMI (**Ma**inz **Mi**crotron) electron accelerator with the three high-resolution magnetic spectrometers of the A1 setup.
MAMI is a continuous wave, normal-conducting electron accelerator [Jan06]. A floor plan of the accelerator and the associated experiments is shown in Fig. 11.
Electrons are produced by a thermionic gun, providing an unpolarised electron beam of high quality and stability with beam currents up to 100 µA. A polarised GaAs photocathode is also available for experiments requiring polarised electrons, operating at beam currents of 20 µA at maximum. After emission from the source, the electrons are accelerated to 3.5 MeV and injected into the first Racetrack-Microtron RTM1. The concept of a RTM is based on accelerating electrons multiple times with the same accelerating cavitiy (see Fig. 12). Every time the electrons pass through the cavity, they gain energy. Each circulation, a so-called *turn*, is related to a constant energy boost, pushing the electrons to larger circles in the microtron. After being recirculated 18 times in RTM2 and leaving stage MAMI-A, the electron has an energy of 180 MeV. This value is the lowest beam energy available for experiments. The next stage of the accelerator, called MAMI-B, consists of the third Racetrack-microtron RTM3. After 51 turns in RTM3, the electrons are boosted to as much as 855 MeV. It is possible to extract the electrons after every second turn leading to a fine-tunable energy range from 180 MeV to 855 MeV in steps of approximately 15 MeV. The last stage, MAMI-C, uses a HDSM (**H**armonic-**D**ouble-**S**ided-**M**icrotron), offering a more economic design for larger electron energies. The HDSM operates with four bending magnets and two anti-parallel linacs, one LINAC operating with twice the frequency of the other leading to the name *"harmonic-double-sided-microtron"*. The design of the HDSM requires precise focussing techniques for the magnets in order to achieve a stable beam. The highest possible energy that electrons can reach at this stage is 1.6 GeV after 43 recirculations. Lower electron energies can be accessed likewise by extracting the electrons before the maximum number of turns is reached.

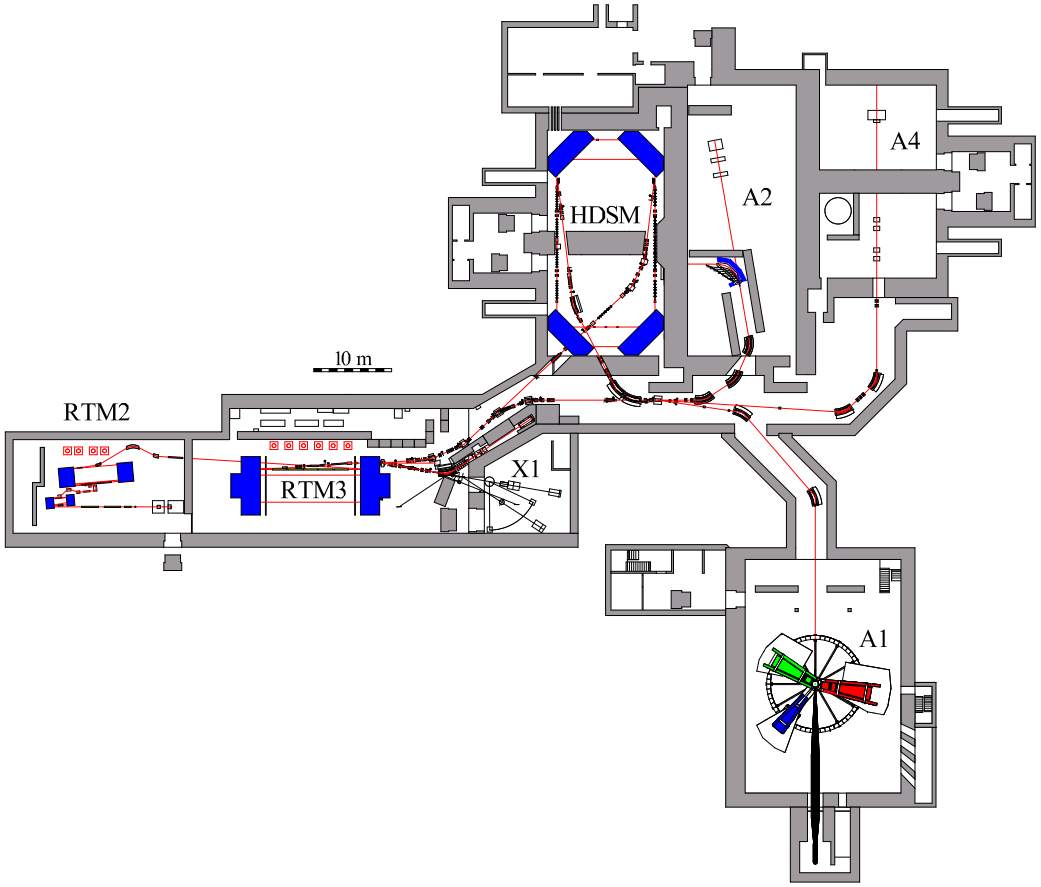

Figure 11: Floor plan of MAMI including the experimental halls A1, A2 and A4 [Ess13].

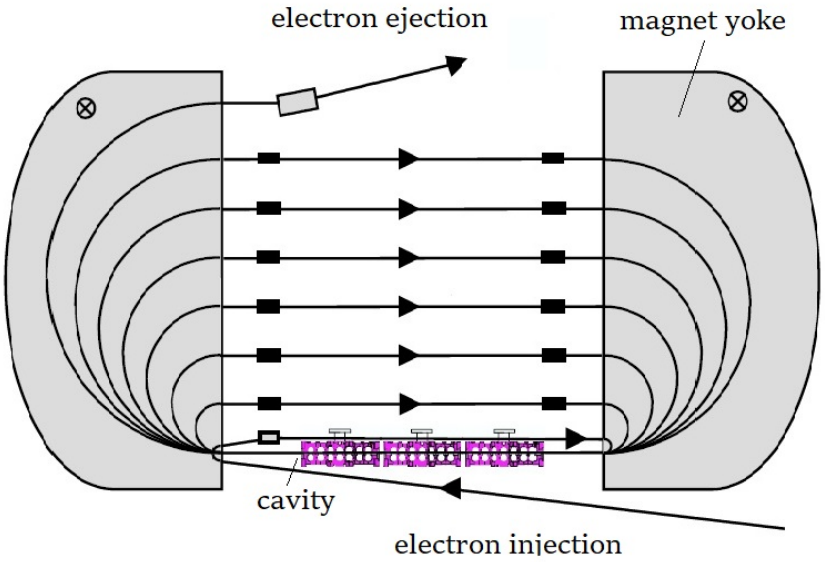

Figure 12: Sketch of a racetrack-microtron [Ber17]. The electrons are injected and gain a constant energy boost of ΔE after each passage through the cavity. The magnetic field in the yokes and the microtron frequency μ_{rf} remain constant, in contrast to other accelerator types.

3.2 DETECTOR SYSTEM OF A1

Three high-resolution magnetic spectrometers form the main setup of A1 to detect charged particles like electrons or pions. Each spectrometer uses a different technique to track, trigger and identify particles emerging from the target. The spectrometers are rotatable over a wide range of scattering angles. This, in combination with the tunable energy of MAMI, allows access to a wide range of Q^2, an import quantity when dealing with form factors. A schematic view of the detector setup is shown in Fig. 13.
After scattering in the target material, the electrons enter the magnetic field of the spectrometers and are bent onto different paths, dependent on the field configuration of the spectrometer and the electron momenta. Several components of the spectrometers, like VDCs (**V**ertical **D**rift **C**hamber) and plastic scintillators, produce signals by ionisation. The data acquisition software `Aqua` (D**A**ta Ac**qu**isition of **A**1) uses the different signals related to a single electron to determine information like time-of-flight and particle track coordinates. This information is fed into the `Cola` (**C**indy **O**n**L**ine **A**nalysis) software for data processing and generation of histograms by merging all detected events into a processable data format. All available data of a detected event can then be condensed into physically meaningful observables, e.g. four-vectors or scalars, but also quantities related to detector properties. The components and functionality of the A1 detector system as also the hardware to acquire raw signals will be described in the following.

3.2.1 *Magnet optics*

Spectrometer A and C have the same magnetic configuration comprising a quadrupole, a sextupole and two dipoles. This configuration provides a strong focussing with parallel-to-point optics in the non-dispersive plane to determine the scattering angle and point-to-point optics in the dispersive plane for high momentum resolution. The vertex acceptance of the two spectrometers can be extended up to a maximum of 28 msr.
Spectromter B has only one "clamshell"-dipole, making the design more economic in size to allow for experiments with small scattering angles. This results in different optical transformation properties as well as a smaller angular acceptance of 5.6 msr at maximum. The design allows measurements of scattering angles below 15° and thus to take data at very low Q^2. For Out-of-Plane measurements spectrometer B can be tilted in a range of $\phi = 0° - 10°$.
The momentum resolution $\Delta p/p$ of these three spectrometers is about 10^{-4} relative. The magnetic field in the spectrometers is measured by a set of nuclear magnetic resonance probes (NMR) and Hall probes.
The characteristics of spectrometers A, B and C are given in Tab. 2. A sketch of the magnet setup for spectromters A and B is shown in Fig. 14. For this experiment, only spectrometers A and B were in use, because measurements of the transition form factor at large Q^2 can be accessed by placing spectrometer B at higher scattering angles.

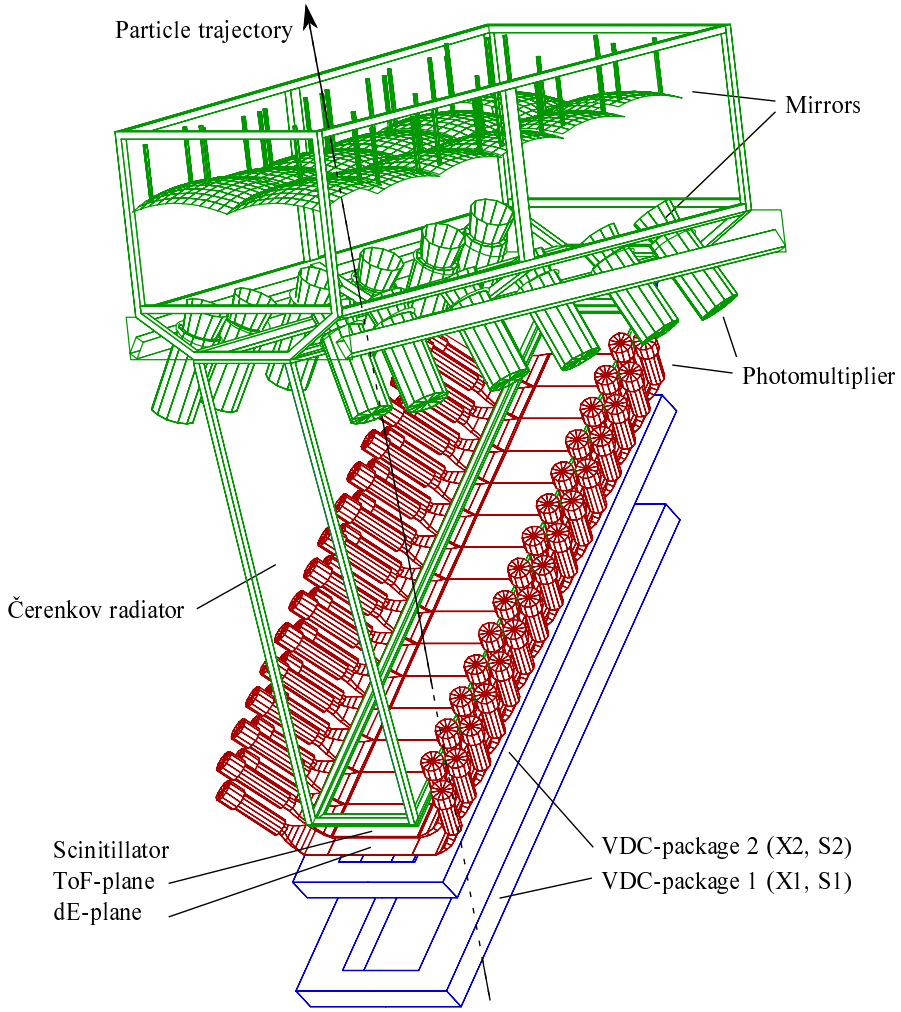

Figure 13: A schematic diagram of the detector components of the A1 detectors [Ber17]. The electrons traverse the VDCs (blue) first, then pass through the scintillators (dE-layer first) and finally, enter into the gas-Čerenkov-detector.

3.2.2 *Drift chambers*

Drift chambers are used for track reconstruction of charged particles. Each spectrometer is equipped with two VDCs (**V**ertical **D**rift **C**hamber), operating with a gas mixture of argon and isobutane. Fig. 15 illustrates the principle of a drift chamber: A charged particle, e.g. an electron (blue), traverses the gas mixture in the drift chamber, it ionises the gas atomes and creates an avalanche of electrons (red) that drift to the anode wires (signal (**S**) or potential (**P**) wires). The drift time and signal pattern of the charge collected by the anode wires provides information about the track of the ionising particle. The drift time depends on the distance to the wire and on specific gas properties, like mixture and density. Also the timing of those signals plays an important role, which will be topic of Sec. 4.2.
If two drift chamber layers are used in parallel, the tracking can be improved. The A1 spectrometers are equipped with two x-layers and two s-layers, where the wires in the s-layer have an angle of 40° with respect to the wires in the x-

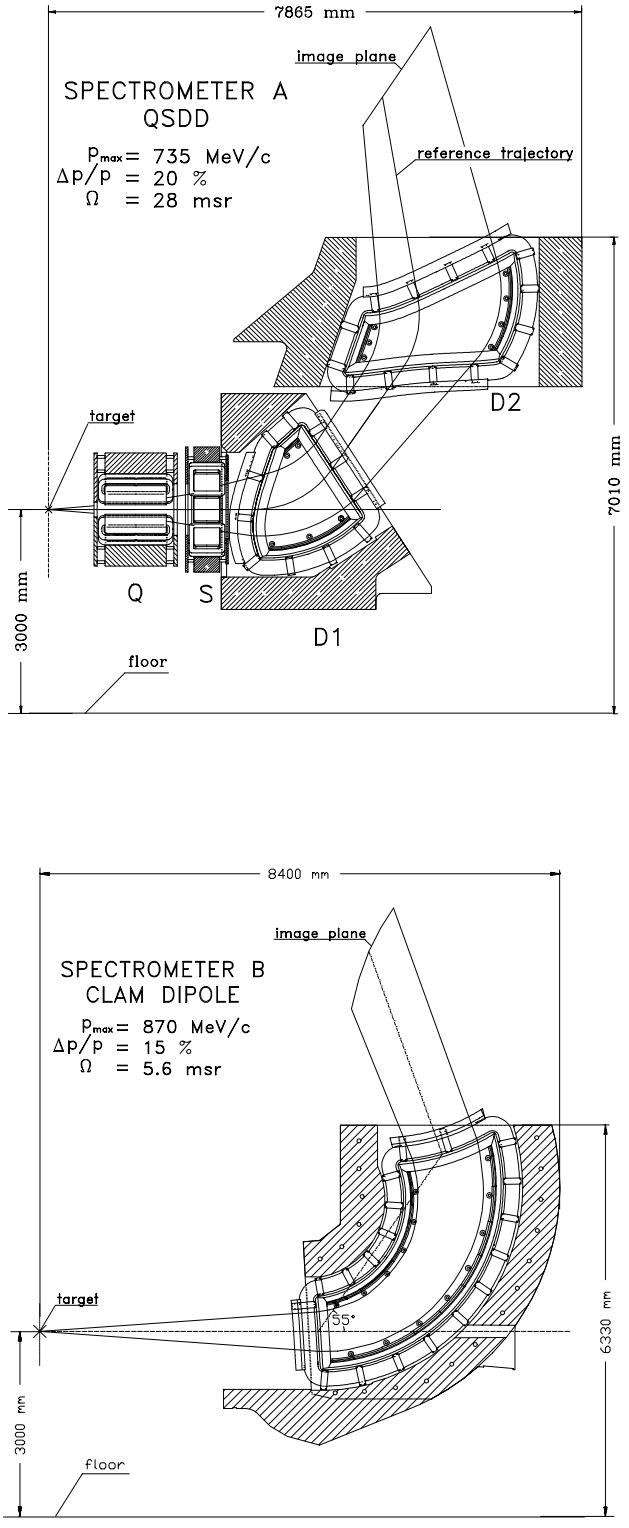

Figure 14: Schematic view of the magnet arrangement of spectrometer A *(top)* and spectrometer B *(bottom)* [AC16]. Besides a dipole for momentum separation, spectrometer A is additionally equipped with a quadrupole magnet to increase the angular acceptance and a sextupole magnet to decrease optical aberrations. In spectrometer B, the "clamshell"-dipole is the only magnet to access smaller scattering angles in the spatially limited environment.

	Spec. A	Spec. B	Spec. C
Configuration	QSDD	D (clamsh.)	QSDD
disp. plane	point-to-point	point-to-point	point-to-point
non-disp. plane	parallel-to-point	point-to-point	parallel-to-point
max. mom.	735 MeV	870 MeV	551 MeV
ref. mom	630 MeV	810 MeV	459 MeV
cent. mom	665 MeV	810 MeV	490 MeV
mom. accept.	20 %	15 %	25 %
solid angle	28 msr	5.6 msr	28 msr
rel. mom. resol.	10^{-4}	10^{-4}	10^{-4}
ang. resol.	< 3 mrad	< 3 mrad	< 3 mrad
pos. resol.	3 mm to 5 mm	1 mm	3 mm to 5 mm

Table 2: Characteristica of the A1 spectrometers. The configuration describes the order and number of magnets (**D**ipol, **Q**uadrupol, **S**extupol) that create the magnetic fields. The solid angle is the maximum solid angle at which the spectrometer can operate, though smaller collimators can reduce the solid angle. The momentum resolution is given relative to the spectrometers central momentum, while the angular and position resolution are given as absolute values.

layer. This geometry leads to an improved angular resolution. For spectrometer A the Čerenkov detector (see Sec. 3.2.4) can be replaced by an HDC (**H**orizontal **D**rift **C**hamber) as focal plane polarimeter for polarisation experiments. To obtain physical observables or target coordinates like particle momentum, vertex or scattering angle, the focal plane coordinates $x_{\mathrm{fp}}, \theta_{\mathrm{fp}}, y_{\mathrm{fp}}, \phi_{\mathrm{fp}}$ are transformed to target coordinates $X_{\mathrm{tg}} \in \Delta p, \theta, y, \phi$ with transfer matrices. The transfer matrices are the outcome of calibration measurements using sieve-slits that provide well defined spatial position information about the particle trajectory in the spectrometers.

$$X_{\mathrm{tg}} = \sum_{i,j,k,l} X_{\mathrm{fp}}(x^i_{\mathrm{fp}}, \theta^j_{\mathrm{fp}}, y^k_{\mathrm{fp}}, \phi^l_{\mathrm{fp}}) x^i_{\mathrm{fp}} \theta^j_{\mathrm{fp}} y^k_{\mathrm{fp}} \phi^l_{\mathrm{fp}} \tag{23}$$

The calculation of the target coordinates is a numerically stable process, as long as the algorithms determining the target coordinates do not have to extrapolate to the acceptance limit in focal plane coordinates. Another effect decreasing the resolution occurs at high reference momenta, where saturation effects distort the magnetic field.

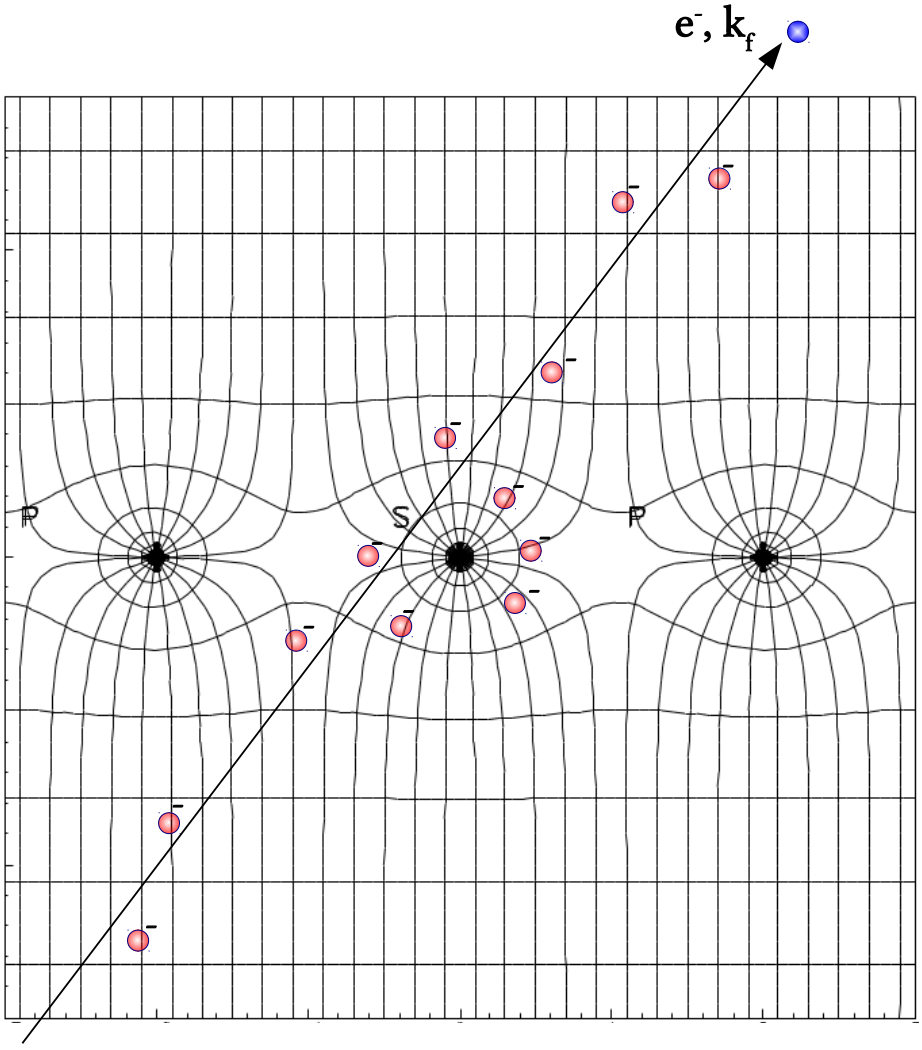

Figure 15: The principle of a drift chamber [Dis92]. An ionising electron (blue) crosses a drift chamber. The electrons from the ionised gas atoms (red) are attracted by the anode wires. The drift time the electrons need to reach the wires provides information about the track of the traversing ionising electron.

3.2.3 *Scintillators*

Scintillator layers in the A1 spectrometers are primarily used to provide trigger signals. Two layers of scintillators are included in each spectrometer, called the dE- and the ToF (**T**ime-**o**f-**F**light)-layer, where the dE-layer is 3 mm thick and the ToF-layer is 10 mm thick. Those layers consist of plastic scintillator bars wrapped with black foil to shield the setup from ambient light. Photomultipliers are placed at both ends of the bars for conversion of the scintillation light into electrical signals.
The dE-layer, as the name indicates, supplies in addition to the trigger signal a first information for the particle identification by energy loss. The ToF-layer is usually used for fast timing. In combination, both scintillators yield information about energy loss and additional signals to identify particles.

Since the detection of protons or charged mesons like pions was not the aim of this experiment, but only measuring high electron rates below meson-production thresholds, only the ToF-layer was used for triggering. The dE-layer still plays a role in determining the efficiency of the ToF-layer (further informations on scintillator efficiency can be found in Sec. 4.3).

3.2.4 *Gas-Čerenkov-Detector*

A Gas-Čerenkov-Counter is used to distinguish electrons from pions. This Čerenkov detector is built from several mirrors in an environment of C_4F_{10} decafluorbutane, serving as radiator gas. The mirrors capture the characteristic light emitted by particles crossing the medium with a velocity larger than the speed of light in the medium (c_0/n), where n is the refractive index of the medium. With a rest mass about 270 times smaller than the pion rest mass, the threshold for Čerenkov light emission is much lower for electrons. In combination with other software cuts it is possible to efficiently separate pion background from data signals (or alternatively veto electrons if the focus is on π^- detection).

3.3 TARGET

Helium as target material has several different properties compared to other frequently used low-Z elements. Helium is a chemically inert noble gas that is less sensitive to leakage compared to hydrogen, which is forming a highly reactive gas mixture when in contact with air. Leakage is still a significant problem for the expensive isotope ^{3}He.
The cryogenic target, available at the A1 collaboration, was refurbished [Hei16] for the purpose to perform experiments with ^{3}He and ^{4}He. This target was improved with more precise temperature and pressure sensors, which are relevant for density and thus luminosity determination. With the installation of fast-response valves, that close with a very short reaction time ($<$ 10 ms) in case of a possible leak at the target-cell, experiments with ^{3}He are now feasible.
The target cell that contains the cryogenic gas is made of aluminium and has a cell wall thickness of 250 µm. The relatively thick cell wall is required to withstand high pressures of the target gas and avoid leakage. On the other hand this leads to a very dominant aluminium background in the data. In order to increase the stability, the aluminium cell was milled from a single aluminium block to avoid welding seams. The operating pressure of helium in the target cell was limited by a drain valve, releasing gas at pressures p$>$ 20 bar. A heat exchange system, operating with liquid hydrogen as cooling medium in thermal contact with the helium cycle, is capable to cool the target gas down to temperatures below 20 K. Pictures and a schematic drawing of the target and its components are shown in Fig. 16.

(a)

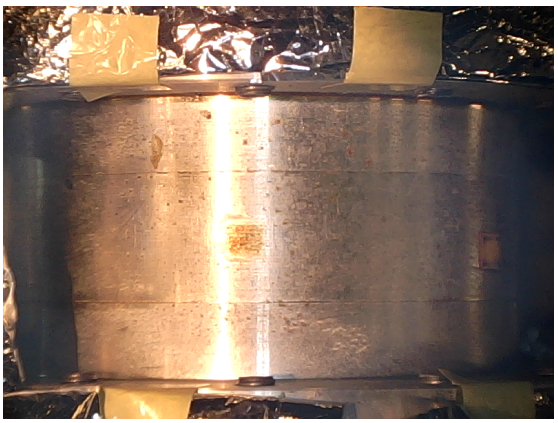

(b)

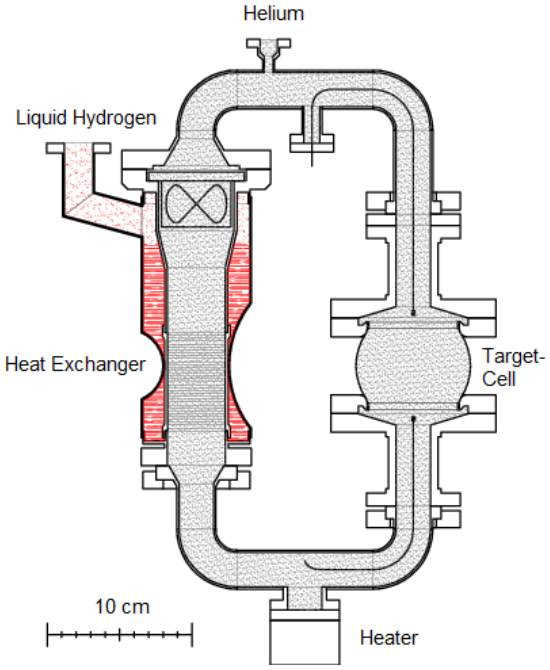

(c)

Figure 16: (a): Components of the ^{4}He target, (b) The aluminium cell used in this experiment, seen through the beam pipeline and (c): Schematic drawing of the helium cryogenic target [Koh01].

4

DATA CALIBRATION

4.1 A1 DATA ACQUISITION

Several steps are required before detector signals are converted to four-vectors. An event is triggered by the trigger logic, which uses signals from photomultipliers attached to plastic scintillators. The trigger unit can operate in single or coincidence mode and suppress readout by a prescaling factor i to only accept every i^{th} event. If the trigger condition is met, information which wires have fired and their related drift times are read out from the drift chamber electronics. This data is converted into a particle trajectory by the A1 data acquisition software `Aqua`[1] (see [Dis96]) using the information from both drift chamber layers. Focal plane coordinates of an event then form an interim result in the data acquisition. `Cola++` [2] is an A1 software package responsible for calculating target coordinates from the focal plane coordinates using optical matrices (see Sec. 3.2.2). At this level, effects like energy loss of scattered electrons and recoil of the target nucleus are taken into account. `Cola++` not only processes the focal plane coordinates to meaningful physical quantities like vertex coordinates, it also generates specific data formats like q_μ or Q^2.
The interaction of these software packages and the sensitivity of some algorithms to certain parameters, e.g. the gas mixture in the drift chambers which influence the drift time, makes it essential to properly determine the parameters that are fed into the `Cola++` software.
These parameters include drift time offsets and drift time velocities of the VDCs, efficiencies of the scintillators, and other detector and target properties. Several of those parameters share dependencies and are thus determined iteratively. The procedures for the calibration of the specific detector components are described below.

1 D**A**ta Ac**qu**isition of **A**1
2 **C**indy **O**n**L**ine **A**nalysis

The drift chamber wires attract ions, produced by a charged particle, traversing the chamber. This collected charge is amplified and, if the signal is large enough to trigger the discriminator, creates a logic pulse that activates a time-to-digital converter (TDC). A signal by the trigger stops the TDC and the data is read out. An event builder run by `Aqua` merges hits of different wires, that are associated with the same charged particle that entered the drift chambers. An algorithm determines the particle trajectory by linear regression. This algorithm uses drift velocity, drift time offset, and other VDC parameters for the particle track reconstruction, but can also disregard broken wires.

4.2.1 *Disabling wires*

The drift chambers contain about 200 wires each per layer, acting as anodes that attract the ionised particles in the chamber gas. If a wire is damaged, a replacement is not always feasible. Instead, the damaged wires are masked in the data acquisition. One can investigate the number of times a wire has fired to detect broken wires, see Fig. 17. Channels with deep gaps and high spikes are detrimental for the track reconstruction and therefore discarded.

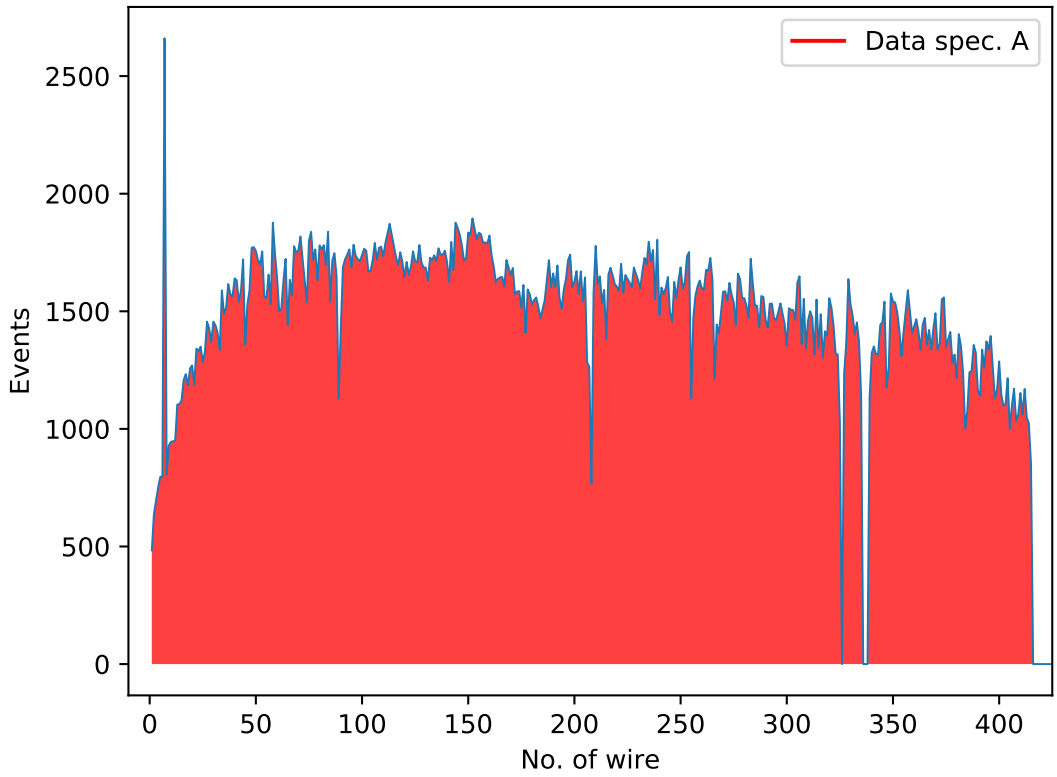

Figure 17: Events vs. wire number for the x2-layer in spectrometer A. Damaged wires produce a gap compared to wires nearby, whereas "hot wires" produce a spike in the spectrum (wire no. 9).

4.2.2 *Drift-time offset*

Another mandatory parameter for data calibration and analysis, is the drift-time offset of the different VDC layers. A typical drift-time spectrum is shown in Fig. 18. The shape of this spectrum can be understood with the help of Fig. 15 which shows the field geometry in the chamber. If electrons ionise the gas close to a wire, the ions move along the field which, in this case, is inhomogeneous. This leads to the large falling edge of the peak with a maximum around 600 ns. If the electrons ionise the gas in an area where the field is almost homogenous, the drift-time offsets are small. This offset parameter is required in the track reconstruction algorithm and it is also influenced by the drift velocity. This requires an incremental determination of drift-time offset and drift velocity, see Sec. 4.2.3. In general the drift-time offset is a parameter that does not vary strongly over duration of an experiment. The obtained values must still be monitored, since a large number of locally concentrated events, e.g. from the elastic line, can lead to deviations. Determining the drift-time offset is done by extrapolating the falling edge of the drift-time spectrum to the abscissa and taking the integer of the intercepted channel as drift-time offset. A linear fit is applied to the signal's falling edge, including all data between 30 % to 70 % of the peak maximum. Fig. 18 shows an example of this optimisation, which is repeated for the different spectrometers, layers, and setups.

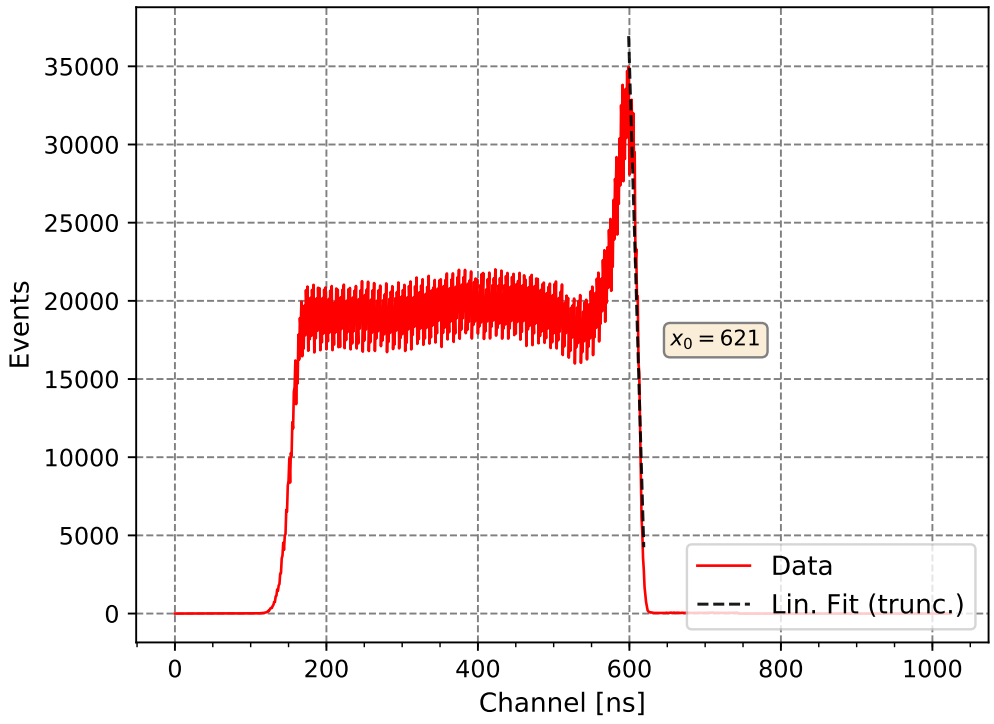

Figure 18: Drift-time spectrum of spectrometer A, x1-layer. The falling edge is fitted to values in a range from 70% to 30% of the peak maximum with the resulting intercept x_0 in the text box.

4.2.3 *Drift velocity*

The drift velocity has a significant impact to the track reconstruction of detected particles. A drift length is approximately the drift velocity multiplied with the drift-time. Environmental conditions, such as air temperature and pressure, influence the drift-time, as can the change of a gas bottle. Impurities hidden in the valve of the gas bottles can contaminate the gas mixture of the drift chambers. An investigation of the drift velocity over the whole experimental duration is thus mandatory.
Finding the optimised drift velocity for each spectrometer is done by minimising the track reconstruction error Δx. A robust procedure is to determine the peak maximum of the Δx histogram over an equally spaced range of drift velocities v_{drift}. The peak position of the track reconstruction error Δx shows a minimum for a certain drift velocity, which is the required parameter for the track reconstruction. This minimum can be determined by a parabolic fit to the obtained data. An extended Δx histogram is shown in Fig. 19.

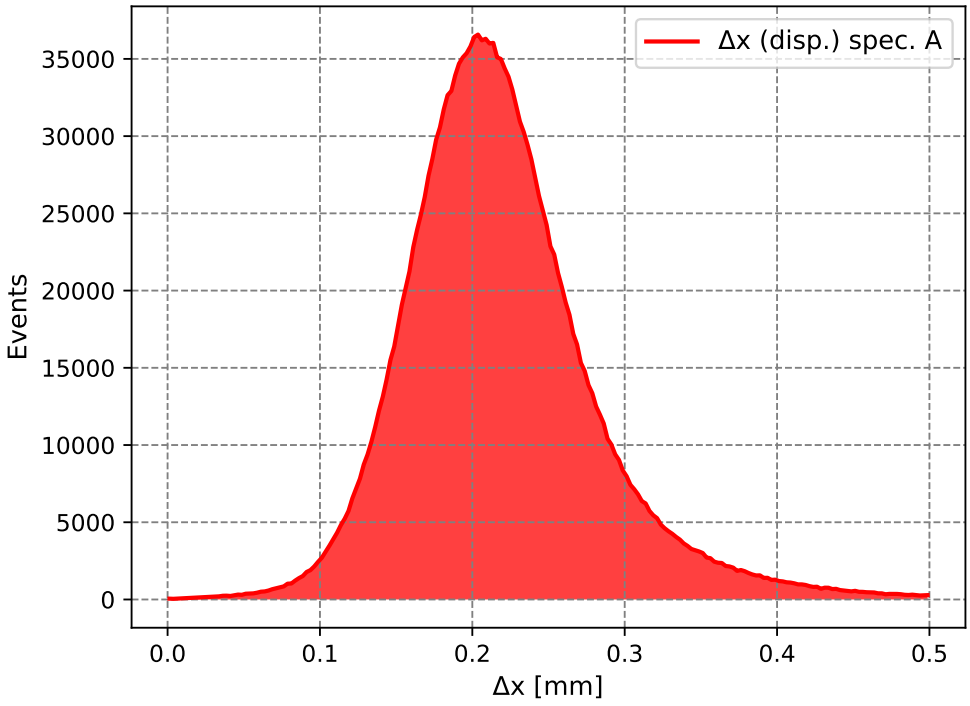

Figure 19: The Δx distribution in the dispersive plane of spectrometer A.

Since the reconstruction error Δx follows an unknown, skewed distribution, the maximum x_0 of this distribution is determined by a gaussian fit to data points in a small, truncated range around the peak maximum (see Fig. 20a). This is done for an initially chosen set of drift velocities v_{drift}, where the Δx-peak position depending on v_{drift} is the quantity of interest (see Fig. 20b). For this purpose the peak positions are fitted as function of the drift velocity with a parabolic function. This is done for all setups and spectrometers A and B independently.

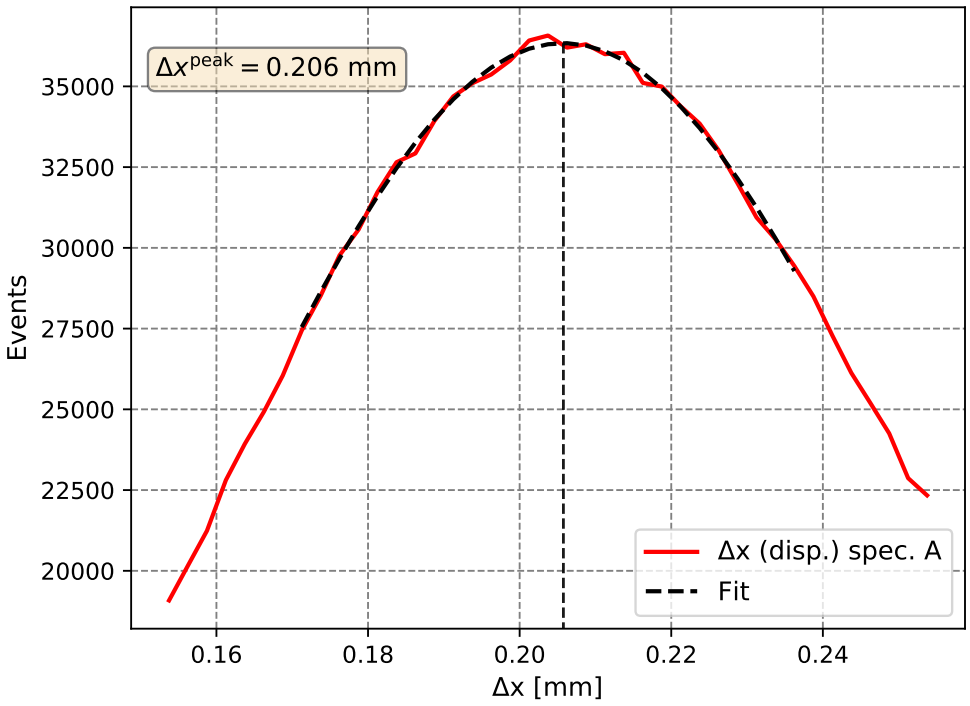

(a)

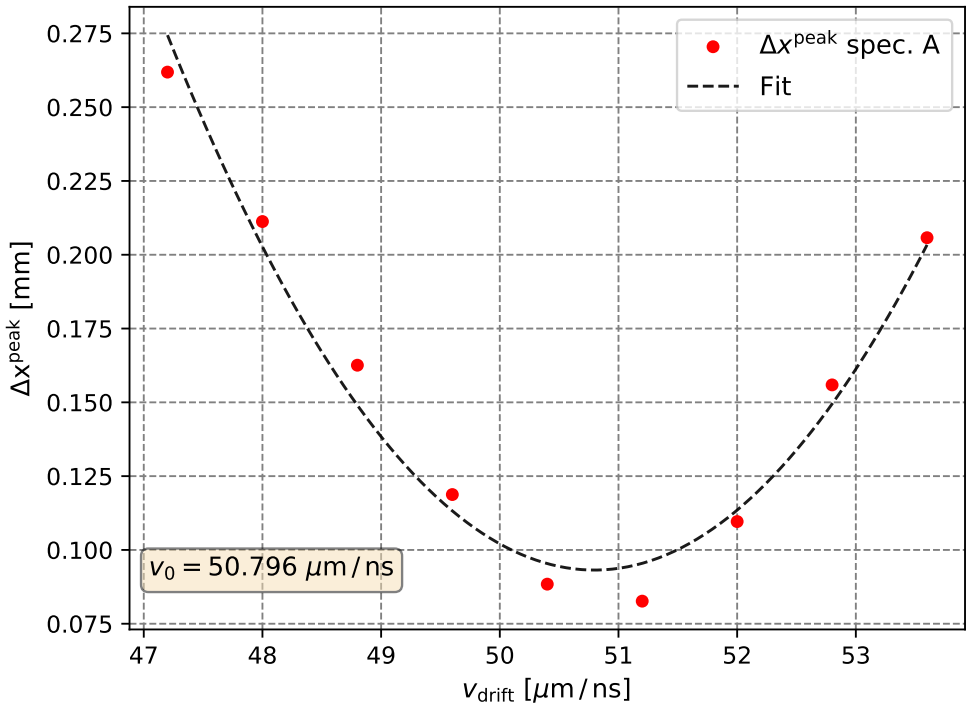

(b)

Figure 20: *(a)*: A small range of data around the maximum of the Δx distribution (solid red line) can be approximated well by a Gaussian (dashed line) to determine the center x_0. *(b)*: Δx^{peak} is minimised for a certain drift velocity. The value $\Delta x^{peak} = 0.206$ from plot *(a)* is found at $v_{drift} = 48.0\,\mu m/ns$.

The result is shown in Fig. 21. The small difference in drift velocity between spectrometers A and B is a well-known property of the A1 setup. Past experiments performed in A1 indicated that gas bottle exchanges can produce a significant change in the drift velocity. During this experiment a bottle of argon gas was exchanged, indicated by the vertical black line in Fig. 21. The influence on v_{drift} is still much smaller than for an exchange of an isobutane gas bottle, which somehow contains larger amounts of impurities in the valve.

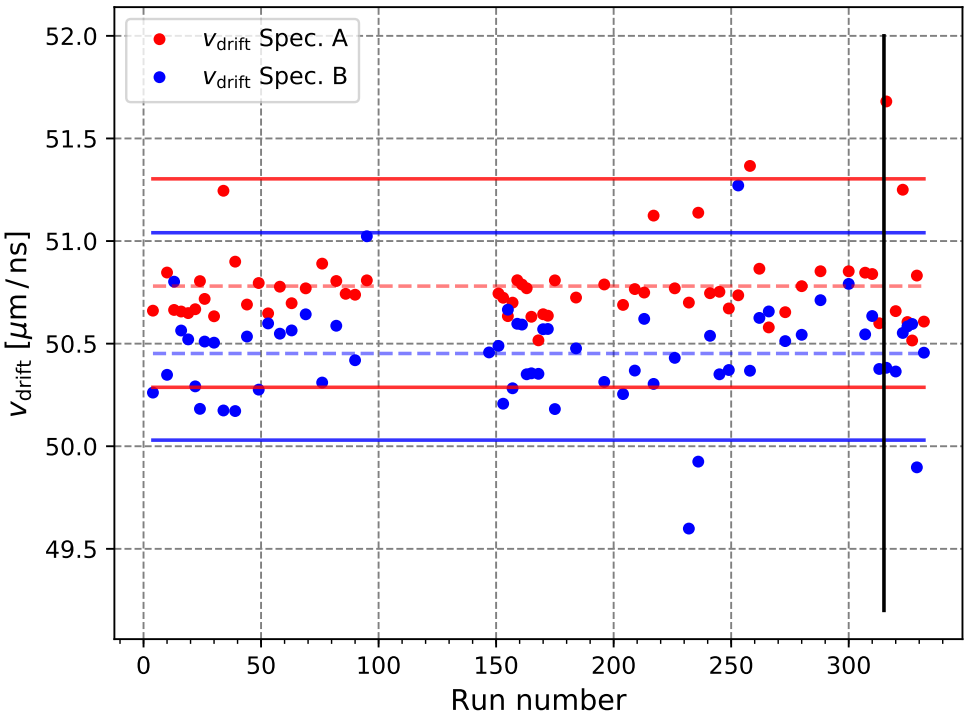

Figure 21: Overview of the determined drift velocities for spectrometers A *(red)* and B *(blue)* for all the setups. Most drift velocities are in the $\pm$ 1 % limits (solid lines) of the average drift velocity (dashed lines). The black vertical line indicates an exchange of Ar gas during the beam time. Deviations are also caused by small statistics of empty-cell runs.

4.2.4 *δ-electrons*

High energy electrons entering the drift chamber can sometimes strip electrons from the gas atoms that absorb enough energy to lead to secondary ionisation of chamber gas. This additionally created ionised charge, often nearby the true electron path, is then erroneously integrated in the track reconstruction. An exemplary configuration of true and false drift times, caused by such a δ-electron is shown in Fig. 22. Here, $t1$, $t2$, $t3$ and $t4$ belong to the electron track traversing the chamber, which has created a δ-electron. This δ-electron ionises gas atoms that fire two wires with a "false" drift-time $tf1$ and $tf2$ respectively. These erroneous drift-times, if not filtered out, would cause the track of the electron to be shifted more towards the wires that have fired for $tf1$ and $tf2$.

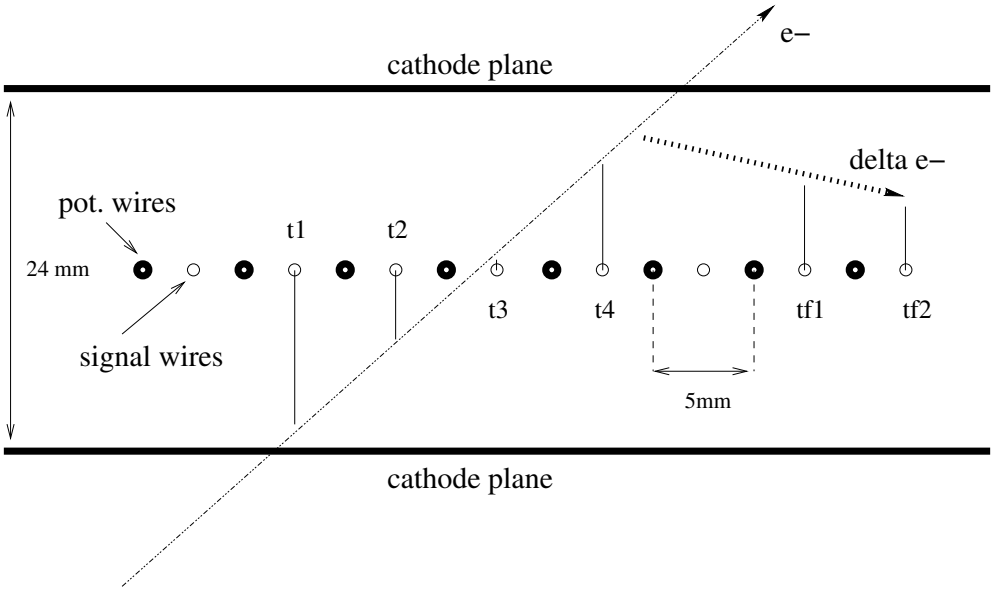

Figure 22: Timing difference of an electron in the VDC. While $t1$, $t2$, $t3$ and $t4$ are related to the electrons track, $tf1$ and $tf2$ are related to signals of δ-electrons. The drift-time difference $tf1 - t4$ or $tf2 - t4$ would be incompatible with the expected particle path. The algorithm for particle tracking can be improved by including timing difference into the calculation, leaving out wires with too large distances to be associated to the particle track.

To remove δ-electrons from the algorithm, additional parameters were introduced for the track reconstruction. One parameter triggers the mode how to proceed with events, if only one wire has fired in a specific chamber layer. These events originate more likely from δ-electrons and can either be ignored completely, or still be taken into account for the track reconstruction. The other parameters are three cut parameters related to the minimum and maximum timing-difference accepted in the track reconstruction algorithm [Frioo]: A δ-electron as shown in Fig. 22, will more likely cause wires to fire further away from the original particle track. The timing difference criterion would then exclude time differences $tf1 - t4$ and $tf2 - t4$ because they are too large.
The mode parameters specifying how to proceed with single wire-events are left unchanged throughout the analysis. The s- and x-layer have different orien-

tation to the electron path. With the s-plane beeing aligned parallel to the electron path, the probability of only one wire firing for a good event is larger than for the x-layer. The approach of determining the cut parameters that exclude too large drift-time differences from δ-electrons is described in Sec. 4.2.4.1.

4.2.4.1 *Drift-time cut parameter determination*

The drift-time cut parameters are slope and intercept of two lines in a plane defined by the drift-time difference and wire number, where the wire number corresponds to the geometrical order of the wires in the drift chamber. The area between those two lines encompasses the accepted events. To determine the parameters of slope and intercept, the following steps are made:

1) A two dimensional histogram showing events per wire and VDC channel for a drift chamber layer is created Fig. 23a.

2) This histogram is converted into a "binary histogram" Fig. 23b: All bins with one or more events are assigned the value 1, all other bins containing no events are assigned a value 0. Disabled wires appear as sharp lines in Fig. 23b.
   After transformation into this binary map, the bins with entry 1 can be interpreted as a data point with timing difference as x- and wire number as y-coordinate. This process accounts for the different statistics in the bins that would interfere in the next steps.

3) Now optimal parameters (slope and intercept) for two lines encompassing the bulk of points and excluding δ-electrons are determined (see Fig. 23c). The chamber geometry for a particular VDC-layer and spectrometer does not change. Thus, the slope of the lines is determined only once (for each of the spectrometers and VDC-layers).

4) To find the optimal intercepts with the abscissa (wire number), a centerline with the same slope like the outer lines is fitted through all the points in such way, that the line sits on the center-of-gravity of the drift-time differences Fig. 23c. The two outer lines are now adjusted symmetrically such that the "data cloud" is contained within.

5) Points lying outside the area encompassed by the two lines, like the small cloud of points in Fig. 23c on the right, are removed.

6) The fit through the remaining points is repeated and the slope and intercepts of left and right linear regression define the cut parameters.

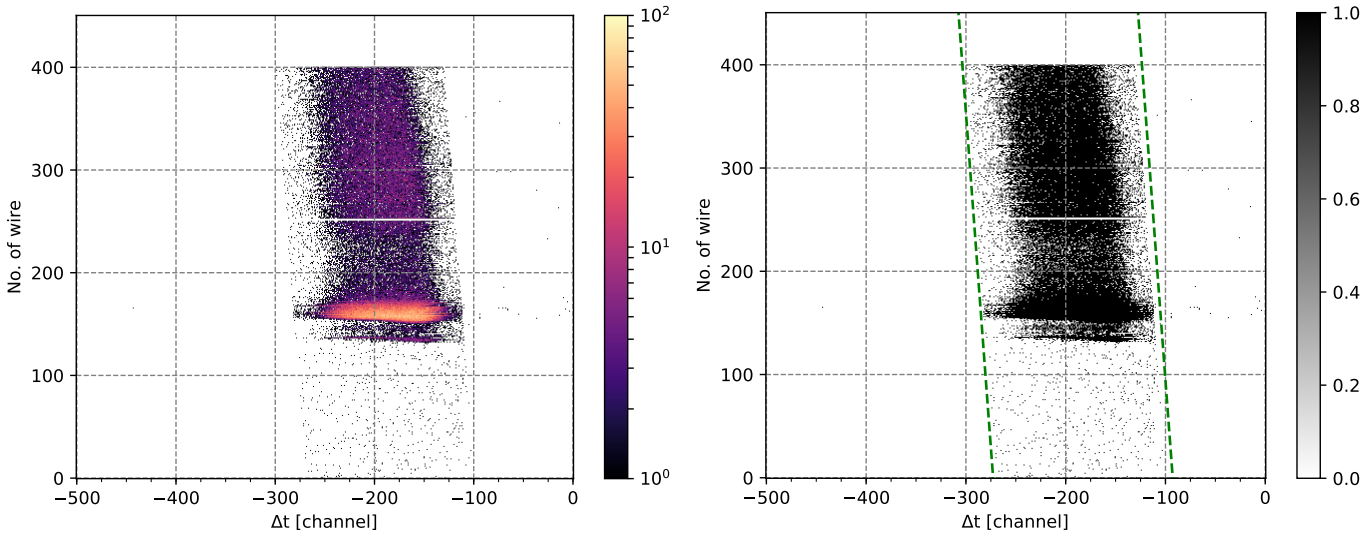

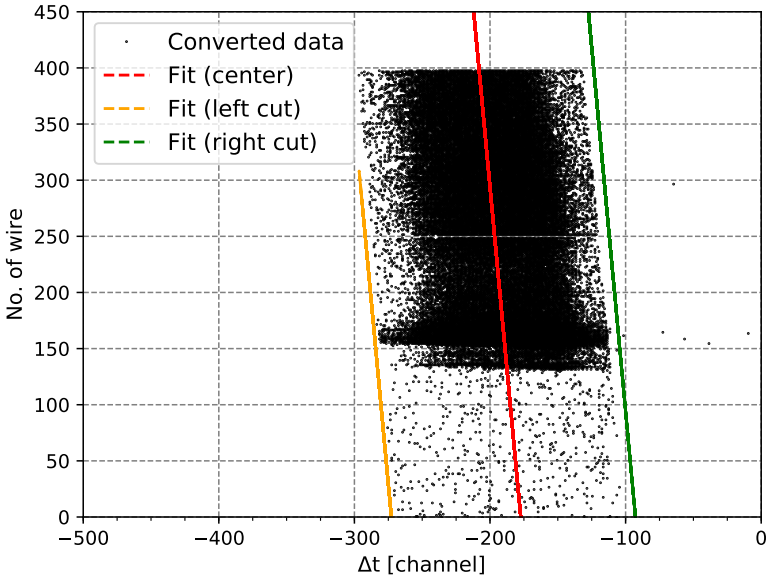

(c)

Figure 23: Drift-time cut parameter determination. *(a)*: Raw histogram showing wire number versus timing difference. *(b)*: The same histogram converted to binary representation. *(c)*: Linear fits to data points applied to the binary histogram. The line in the middle crosses the center-of-gravity of the data. The intercepts of the fitted lines with the Δt-axes define the cut parameters. All events lying outside the area between the two lines do not match the drift-time difference criterion and were discarded.

4.3 SCINTILLATORS

Scintillators, with their fast time response and energy sensitivity, are a good choice for a trigger system. The trigger system of the A1 spectrometers consists of two plastic scintillator layers called dE- and ToF-layer[3], located on top of the drift chambers. The dE-scintillator-layer can be additionally used to supply energy loss information for particles heavier than electrons. The ToF-scintillator-layer generates timing reference signals for the drift-time determination of the VDC. To estimate the efficiency of a scintillator layer, the other layer is used to provide a reference for comparison. Assuming 100 % efficiency in the reference layer, the layer to be tested should receive the same number of hits as the reference layer. The VDC particle track information is in addition used for position-resolved efficiency determination. The deviation of the number of hits between reference and investigated layer yields the position-resolved scintillator efficiency (see Fig. 24). Areas in the x-y-scintillator plane with low statistics, where electrons scarcely enter, are assumed to have an efficiency of 100 %. With these areas being rarely hit by electrons, the assumption of 100 % efficiency is uncritical and has a negligible effect on the analysis.

3 **T**ime **o**f **F**light

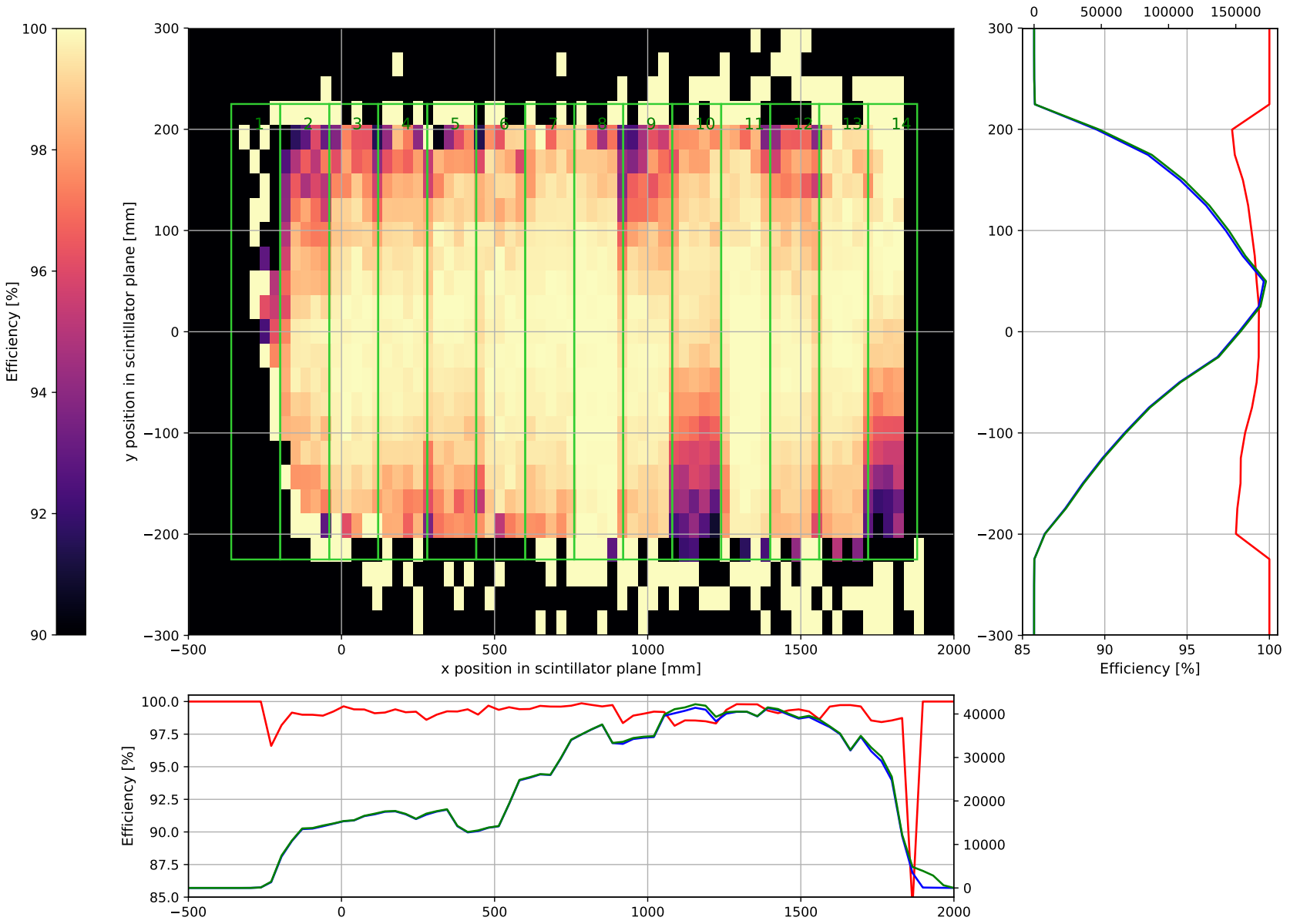

Figure 24: Efficiency of the ToF-scintillator-layer of spectrometer A used as trigger component for this experiment. The red lines in the two small plots (*right* and *bottom*) show the efficiency projected on the x- and y-coordinate, respectively. Green lines belong to number of events of the reference trigger (dE-scintillator-layer), the blue lines belong to events where also the ToF-layer produced a trigger signal. The light green rectangle in the center plot indicate the geometry of the trigger system.

4.4 NMR AND HALL PROBE CALIBRATION

The relative momentum resolution of the magnetic spectrometers is about $\delta_p \approx 10^{-4}$. NMR probes are used to measure the magnetic fields in the spectrometers. In addition, each spectrometer is equipped with several Hall probes, that yield a less precise field value but operate more reliably. The difference in precision between NMR and Hall probe measurements is about one order of magnitude. While for spectrometer A the central momentum can be measured with NMR probes, it is a well known problem of spectromter B, that these probes do not always work, due to the inhomogeneous magnetic field of the clam shell dipole. Hence, one has to rely on the Hall probe measurements for spectrometer B, yielding a relative resolution of approximately $\delta_{\text{Hall}} \approx 10^{-3}$.
Experiments made in the past showed, that spectrometers A and B should not approach too closely to avoid an interference of the sextupol magnet of spectrometer A to the dipole of spectrometer B. During the experiment and when preparing the setups, care was taken to avoid this issue.
The central momenta of both spectrometers are calibrated by fitting a $\mathcal{O}(4)$ polynomial for spectrometer A and a $\mathcal{O}(3)$ basis spline for spectrometer B to the central momenta versus the magnetic field values of the probes.

4.5 TARGET DENSITY

In contrast to hydrogen targets operating with the liquid phase of hydrogen at stable density, the helium target operating with cryogenic helium is more vulnerable to heat dissipation of the electron beam. Thus the gas density fluctuates stronger at different beam intensities requiring a high-frequent monitoring of temperature and pressure. The gas density can be evaluated by using an expansion of the virial theorem for gases [McC73]:

$$\begin{aligned} 0 = {} & p - \rho RT - \rho^2 B(b_i, T) \cdot RT - \rho^3 \sum_{i=1}^{8} n_{1,i} T^{(\frac{3}{2} - \frac{i}{2})} - \rho^4 \sum_{i=1}^{4} n_{2,i} T^{(\frac{3}{2} - i)} \\ & - \rho^5 \sum_{i=1}^{6} n_{3,i} T^{(\frac{3}{4} - \frac{i}{4})} - \rho^3 \sum_{i=1}^{3} n_{4,i} e^{\gamma \rho^2} T^{(1-i)} \\ & - \rho^5 \sum_{i=1}^{3} n_{5,i} e^{\gamma \rho^2} T^{(1-i)} - \rho^6 \sum_{i=1}^{2} n_{6,i} T^{(1-i)} \end{aligned} \tag{24}$$

with p pressure and T temperature of the gas. Coefficients b_i and n_{j_i} depend on p and T and have to be chosen by the particular region in the pT-diagram according to the helium phase (in this case above the boiling point of helium). The density can then be calculated iteratively by searching the root of (24) with the Newton-Raphson algorithm.
Fig. 25a shows the density as a function of pressure p and temperature T. With typical values for helium pressure of 20 bar and temperature of 20 K, a target density of 47.00 mg cm^{-3} for ^{4}He has been achieved.

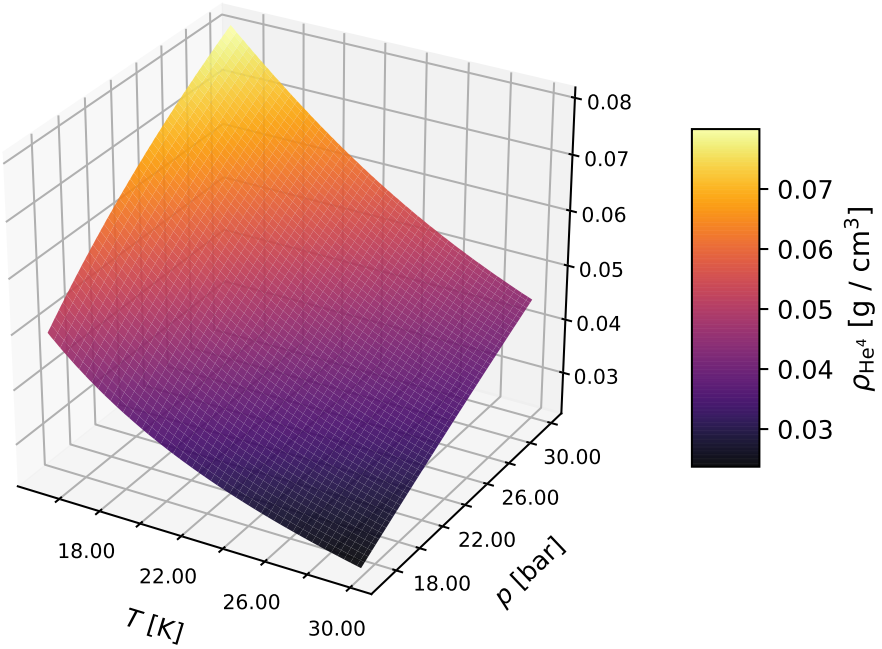

(a)

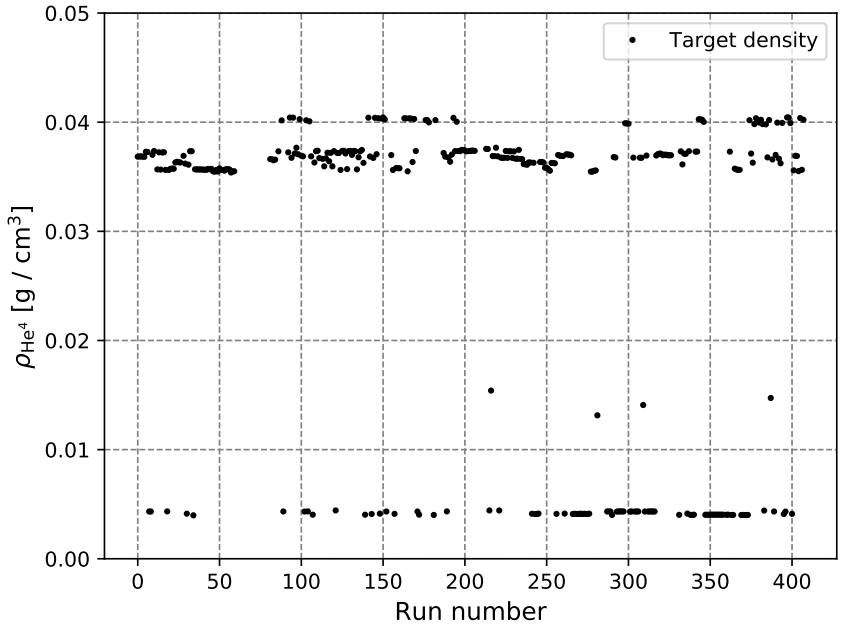

(b)

Figure 25: *(a)*: Helium density evaluated with (24) as a function of temperature T and pressure p. *(b)*: The target density during the experiment. The data runs have roughly ten times higher density than the empty-cell runs. Density fluctuations in the data runs are caused by different beam intensities.

In comparison to helium at standard pressure and temperature of 1.013 bar and 299.15 K, the target density is roughly increased by a factor 250. A cross-check by calculating the helium density with the ideal gas equation results in deviations of only a few percent compared to (24). An overview of the gas density over the duration of the experiment, also including the empty-cell measurements with effectively reduced helium density, is shown in Fig. 25b. The density fluctuations of the production data are caused by adjusting the beam intensity to the count rates, which strongly decrease at larger scattering angles. Beam intensities during the experiment range from 50 nA to 2 µA causing different heat dissipation in the target gas and leading to thermal fluctuations affecting the density inside the target cell.

4.6 MISSING MASS

The basic formula necessary to determine a form factor, in this case the transition form factor $|\mathcal{F}_{\mathrm{M0^+}}(Q^2)|^2$ of the monopole resonance, is given by

$$|\mathcal{F}_{\mathrm{M0^+}}(Q^2)|^2 = \frac{\left(\frac{d\sigma}{d\Omega}\right)_{\mathrm{exp}}}{\left(\frac{d\sigma}{d\Omega}\right)_{\mathrm{Mott}}} \tag{25}$$

in which

$$Q^2 = -q_\mu q^\mu = -(\omega^2 - \vec{q}^2) \simeq 4 \cdot E_i E_f \sin^2(\frac{1}{2}\theta) \tag{26}$$

is the negative, space-like, squared four-momentum transfer of the scattered electron, with E_i the initial and E_f the final electron energy.
In the high-relativistic limit with $E_i \gg m_e$, we neglect the electron rest mass and use the last term of (26) for simplification. Data binned in Q^2 are evaluated at the mean of this distribution and yield a central value[4] of Q^2.
The Mott cross section reads as

$$\left(\frac{d\sigma}{d\Omega}\right)_{\mathrm{Mott}} = \frac{\alpha^2 \cos^2(\frac{1}{2}\theta)}{(2 \cdot E \sin^2(\frac{1}{2}\theta))^2} \tag{27}$$

with α the fine-structure constant, E the (initial) electron energy and θ the scattering angle. It is thus specified only by kinematic observables. The experimental cross section is divided into multiple parts, each dependent not only on the measured kinematics but also on specific parameters of the experimental setup:

$$\left(\frac{d\sigma}{d\Omega}\right)_{\mathrm{exp}} = \frac{\mathcal{N} - \mathcal{N}_{\mathrm{BG}}}{d\Omega_{\mathrm{exp}} \cdot \mathcal{L}_{\mathrm{int}} \cdot \varepsilon} \tag{28}$$

4 A more precise description of the determination of Q^2 by its distribution can be found in Sec. 6.4 and App. A.

with experimental angular acceptance $d\Omega_{\text{exp}}$, integrated luminosity $\mathcal{L}_{\text{int}}$, detector efficiency ε, number of measured events $\mathcal{N}$ and background events $\mathcal{N}_{\text{BG}}$. The experimental angular acceptance $d\Omega_{\text{exp}}$ depends on the central angle and the relative angular acceptance, which again depends on the collimator of the spectrometer used during the experiment. An important tool to deal with the angular acceptance is Monte-Carlo simulations: the spectrometer's phase space is influenced by kinematic parameters like momentum and scattering angle, as well as software cuts. The integrated luminosity $\mathcal{L}_{\text{int}}$ depends on measurement time, beam current, target density and length of the target. The efficiency correction ε is a factor that includes the efficiency of detector components and the dead time of the data acquisition. The expression $\mathcal{N} - \mathcal{N}_{\text{bg}}$ can be considered as the number of background events subtracted from all detected events. This subtraction is performed in binned *missing mass*[5] spectra. The quantity missing mass (m_{miss}) can be derived from the conservation of four-momenta during the scattering process:

$$k_i^\mu + K_i^\mu = k_f^\mu + K_f^\mu \tag{29}$$

with k_i^μ the inital electron four-momentum given by the beam energy, k_f^μ the four-momentum of the scattered and detected electron. If the target is at rest, the initial four-momentum of the target nucleus is $K_i^\mu = \{M, 0, 0, 0\}$ with M the target rest mass. K_f^μ is the final four-momentum of the target nucleus, which in our case is unobserved. Still, the four-momentum K_f^μ of the target nucleus can be reconstructed,

$$K_f^\mu = k_i^\mu - k_f^\mu + K_i^\mu = q^\mu + K_i^\mu \tag{30}$$

where we use the notations in Tab. 1. From calculating the norm of K_f^μ one obtains the quantity *invariant mass*:

$$\sqrt{{K_f}^2} = \sqrt{(M + E_i - E_f)^2 - |\vec{q}|^2} = \sqrt{M^2 + 2M(E_i - E_f) - Q^2} = m_{\text{inv}} \tag{31}$$

The missing mass is then calculated as

$$m_{\text{miss}} = m_{\text{inv}} - M \tag{32}$$

where the target rest mass M is subtracted from the invariant mass.
Fig. 26 shows a typical missing mass spectrum of ^{4}He. Taking energy loss in the target into account, the elastic peak of the ^{4}He ground state is centered at $m_{\text{miss}} = 0\,\text{MeV}$. The monopole resonance, the quantity of interest, can be seen as a tiny peak at around 20.21 MeV and enlarged in the small inset of the plot.

5 Other terms like *missing energy* or *photon mass* are also common.

Considering the logarithmic event-scale, one quickly recognises that the background is enormous in this case. Different types of background need to be taken into account: the background from electrons scattering on ^{27}Al in the target cell walls, and events from elastic and quasi-elastic scattering on ^{4}He. This demonstrates the major challenge, in dealing with backgrounds to extract $|\mathcal{F}_{M0^+}(Q^2)|^2$. The following chapters describe in detail the separation of the background from the signal.

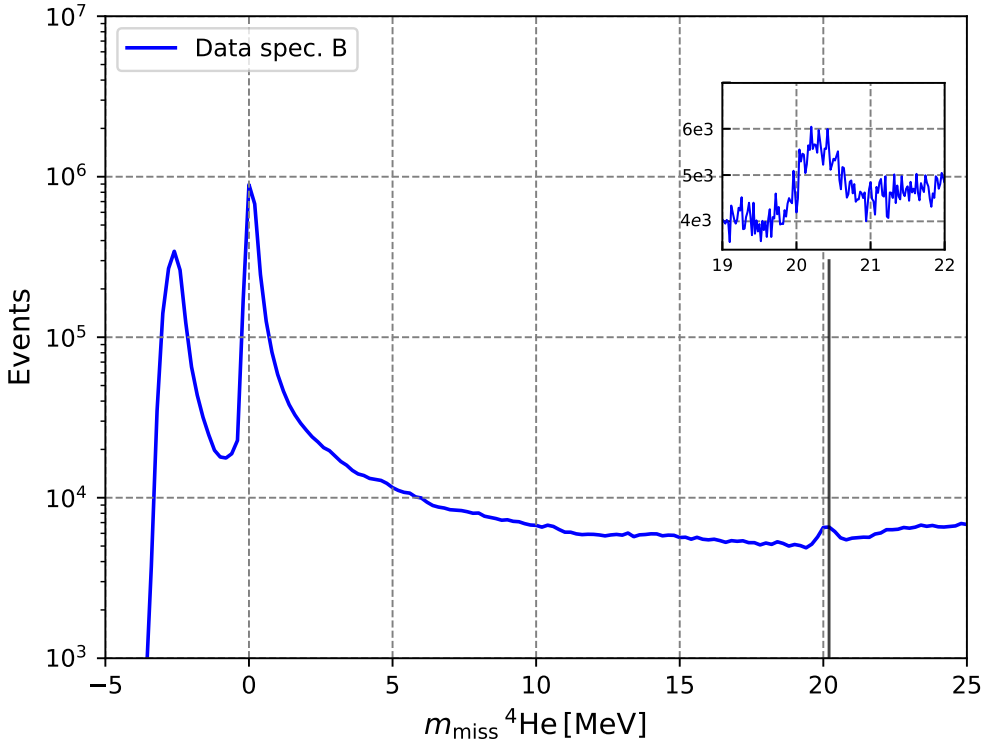

Figure 26: Typical m_{miss}-spectrum of ^{4}He. The elastic line of ^{4}He is located at 0 MeV, the peak on the left at lower m_{miss} is the elastic ^{27}Al line from the target cell. The monopole resonance of ^{4}He at 20.21 MeV is located on the continuum, between proton and neutron break-up threshold.

5

EMPTY-CELL MEASUREMENTS AND BACKGROUND STUDIES

5.1 INTRODUCTION

Measuring an isotope in gaseous form poses several challenges. The density of the target isotope has to be as high as possible while the mass density of the cell material has to be as low as possible. Too thin cell walls on the other hand cause safety issues. Other requirements are e.g. to minimise the radioactive contamination under beam conditions. The target should also be accessible for a large range of scattering angles, which is sometimes challenging due to lots of components attached to it. The cell material of the cryogenic target is natural aluminium, which is nearly 100 % ^{27}Al, with a small amount of stabilising components, thus forming an alloy widely used in research and industry. Typical additional metals in industrial aluminium are copper, manganese, silicon and zinc, with typical concentrations of $1.0 - 3.5\,\%$. Aluminium as target material has several advantages:

- Radioactive contamination is minimal because ^{27}Al has only short-lived- or low-energy radiative modes that are activated in typical electron scattering experiments.
- The mechanical strength of aluminium allows for high gas pressure.
- With effectively a single isotope in the cell walls, more precise background studies are possible.

Background studies of the target offer the opportunity to reduce uncertainties in the background subtraction as well as to improve the statistics in the data analysis: with a complete target cell model, error-prone vertex- or target-coordinate-cuts, usually applied to separate cell wall events, are avoided. In this experiment every production-data setup was accompanied by an empty-cell measurement, with identical kinematical settings to determine electron scattering from the target walls. This was achieved by reducing the helium density inside the cell by one order of magnitude. The cell was not completely emptied to protect the thin cell wall against tension forces generated by heating due to the electron beam. Simulations of the background were developed and tested with the empty-cell data. The optimised models were then used to simulate the background under the condition of the production data at higher helium pressure. The main differences between empty-cell and production data

are given by energy loss and multiscattering effects by the electrons. In the following sections the different contributions from the cell walls of the background are discussed and their simulations outlined.

5.2 ^{27}AL GROUND STATE FORM FACTOR

^{27}Al is the only stable aluminium isotope and has spin and parity quantum numbers $J^\pi = 5/2^+$.
The form factor of nuclear ground states is hard to calculate analytically as the number of terms of the multipole expansion grows with higher spin. Therefore, the use of a phenomenological form factor model is necessary.
If one assumes a spherically symmetric, uniform charge density distribution in space,

$$\rho_E(r) = \begin{cases} 3Z/4\pi R^3 & r \leq R \\ 0 & r > R \end{cases} \tag{33}$$

the charge form factor is the Fourier transform of $\rho_E(r)$, given by

$$\begin{aligned} \mathcal{F}(\rho_E(r))(q) = F_E(q) &= 3Z/2 \cdot \frac{\sin(qR)}{qR} \\ &= 3Z/2 \cdot j_0(qR) \end{aligned} \tag{34}$$

A better approximation is a spherically symmetric charge density distribution with a diffuse edge. This model is often referred to as the *Helms Model*, [Hel56], [CHK$^+$61], [Ueb71], which works well for nuclei with spin and parity $J^\pi = 0^+$. This model convolutes two charge distributions, a homogeneously charged sphere $\rho_E(r, R)$ and a gaussian function $\rho_G(r, \sigma)$

$$\rho_H(r) = \rho_E(r, R) * \rho_G(r, \sigma) \tag{35}$$

with a variance σ related to the surface thickness of the nucleus. Using the convolution theorem, the charge form factor $F_H(q)$ turns out to be a product of two simple terms,

$$F_H(q) = F_E(q) \cdot F_G(q) \tag{36}$$

where $F_E(q)$ and $F_G(q)$ are the Fourier transform of $\rho_E(r, R)$ and $\rho_G(r, \sigma)$, respectively. The form factor is then a product of $F_G(q)$, itself a Gaussian, and a spherical Bessel function of first kind $j_0(qR)$. This model requires two parameters: the radius R and the surface thickness σ, obtained by fits to form factor data or semi-empirical formulas [LB67]. The use of more realistic charge density functions in (35) may still not provide a perfectly realistic form factor because of the uncertainty of the parameters R and σ . It also becomes inappropriate for higher Q^2 as emphasized in [FV82]. Also the minima of the form factor calculated by *Helms Model* are not as distinct as shown in Fig. 27a, an

effect of Coulomb distortion which becomes stronger when electrons scatter on nuclei with higher Z.
To adjust the simulation based on *Helms Model* to the ^{27}Al ground state with the available data, the following procedure is followed:

1) A cut in missing mass is applied around the elastic peak of ^{27}Al. The number of events n_{data} satisfying the cut conditions is determined. The cut limits are chosen to include most of the ground state. The same cut is also applied to the simulation of elastic scattering on ^{27}Al and the events n_{simul} are determined likewise.

2) The correction factor given by the ratio $n_{\text{data}}/n_{\text{simul}}$ was applied to the simulation.

3) After the simulation was corrected, the resolution parameters are determined by minimising the χ^2 between data and simulation.

4) A final determination of the ratio between data and simulation, with the optimised resolution parameters, yields a more accurate correction factor.

Model uncertainties have been taken into account this way. Fig. 27b shows this procedure, where some excited states of ^{27}Al can be seen in the data. The handling of those will be discussed in detail in the next section. In Fig. 27b one can also see a secondary peak from a heavier nucleus in the missing mass spectrum of ^{27}Al. This peak appearing only in certain kinematics could not be ultimately identified but it is most likely manganese, an element often added to aluminium to improve its stability. The influence of this peak can be elimitated by applying a thighter cut to the ^{27}Al elastic peak.
The procedure described above was repeated for the production-data to check its consistency. Factors determined both for empty-cell and production-data to adjust the simulation for elastic electron scattering on ^{27}Al are in good agreement.

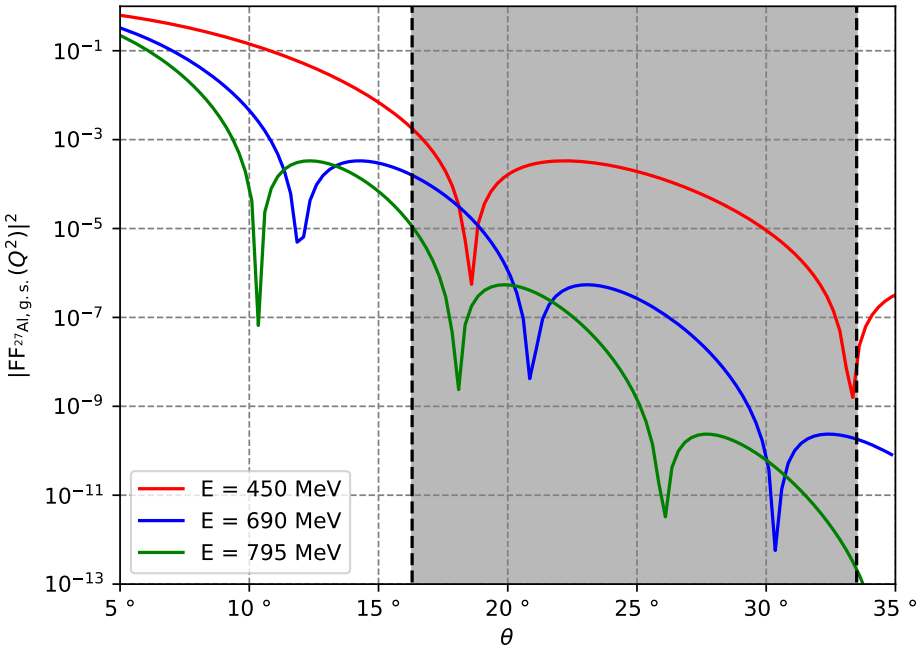

(a)

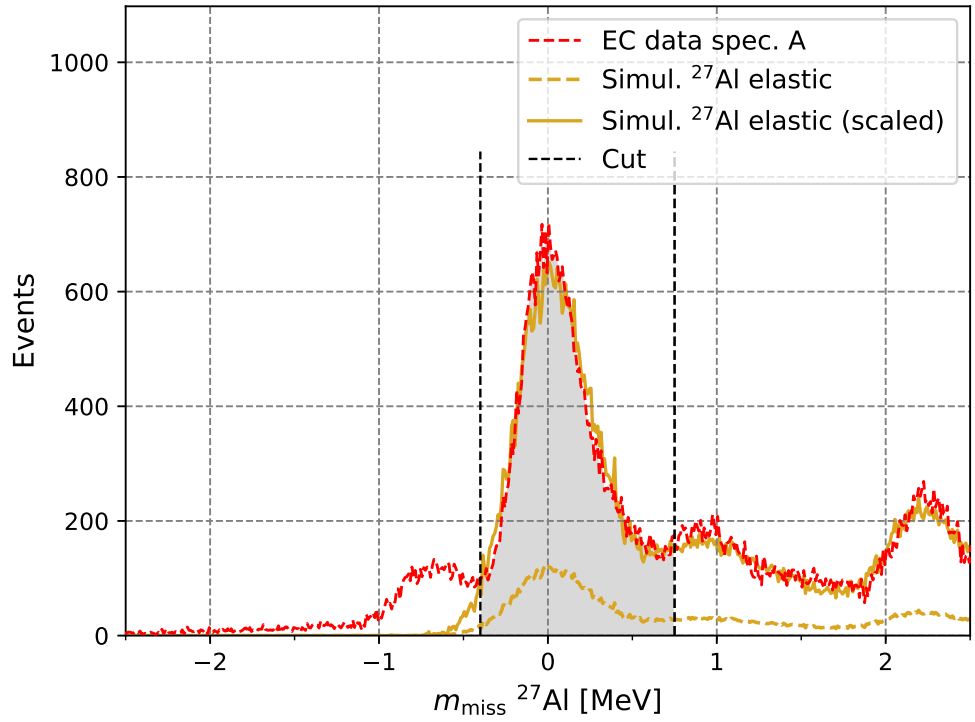

(b)

Figure 27: *(a)*: Form factor of the ^{27}Al ground state for the three energies measured in this experiment as a function of scattering angle calculated with *Helms Model*. The dashed vertical lines indicate the range of maximum and minimum angles in the experiment. *(b)*: Correction and scaling of the simulated ^{27}Al form factor to empty-cell data. The black dashed lines define the normalisation region.

5.3 ^{27}Al EXCITED STATES

^{27}Al has a vast number of nuclear levels, most of which can be observed in electron scattering [Bas11]. The energetically highest observed states lie far below the proton threshold in ^{4}He at 19.85 MeV, marking the onset of the quasi-elastic continuum. It can be excluded that the excited states of ^{27}Al will contribute much background to the resonance and thus the transition form factor. Contributions from these excited states are still of interest when ^{4}He elastic scattering data are compared to simulations. This procedure is in this analysis used to normalise the data with the elastic peak of ^{4}He with form factor parametrisations from former experiments. When determining the intensity of the excited states, one has to deal with several problems:

- The presence of remaining ^{4}He in the target cell when taking the "empty-cell" measurements. Beeing a lighter nucleus, the ^{4}He elastic peak is proportionally larger than the elastic peak of ^{27}Al. It also overlaps with the excited states of ^{27}Al in m_{miss}-spectra and thus complicates the determination of the yield of particular levels.
- The excited states of ^{27}Al lie very close together in the energy spectra. Even with a momentum resolution of $\delta \approx 2 \cdot 10^{-4}$ it is not possible to clearly separate two energy levels with an energy difference of e.g. $\delta E \approx$ 100 keV at a beam energy of 500 MeV.

To avoid these problems it is convenient to link the intensity of the nuclear levels relative to the yield of the elastic peak of ^{27}Al. In this way, every correction applied to the elastic form factor of ^{27}Al propagates directly to the form factor of the ^{27}Al excited states.
The first two excited states of ^{27}Al $J^\pi = 1/2^+$ and $J^\pi = 3/2^+$ have an energy difference of 0.17 MeV, making a distinction barely possible for low central momenta. If states lie too close for a clear distinction[1], several states were modeled by just one peak placed approximately in the center between these excited states. As long as one is not interested in an absolute measurement of form factors of every excited state, this approximation does not significantly affect the analysis of the monopole resonance.
Fig. 28 shows a zoom of the first ^{27}Al excited states, where sharp peaks indicate different energy levels.

1 One of many such cases are two states at 2.98 MeV and 3.00 MeV, with spins $J^\pi(2.98\,\text{MeV}) = (3/2)^+$ and $J^\pi(3.00\,\text{MeV}) = (9/2)^+$

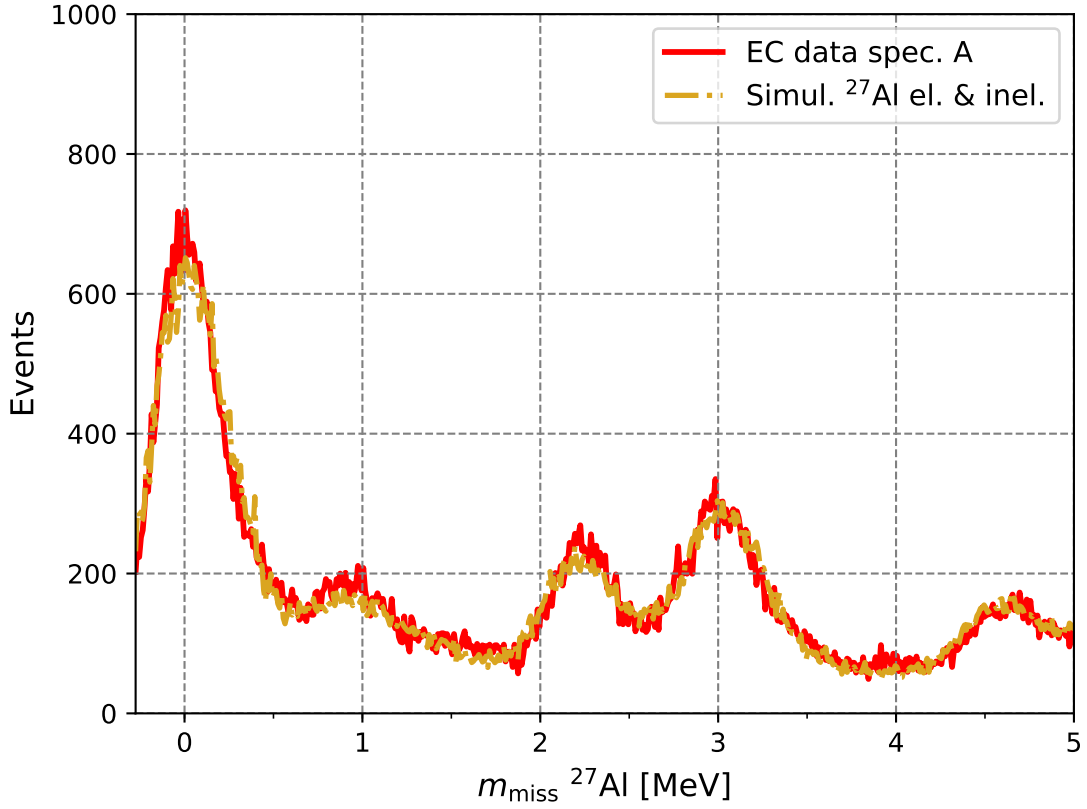

Figure 28: Comparison of data to simulation for a typical ^{27}Al m_{miss}-spectrum of the empty-cell measurements. The elastic peak of ^{27}Al at $m_{\text{miss}} = 0\,\text{MeV}$ is followed by low-energy excited states. Appearence and strength of these peaks depend strongly on the kinematics.

5.4 ^{27}Al quasi-elastic continuum

The more dominant background in the spectra is caused by the quasi-elastic continuum of ^{27}Al.
This continuum starts at the proton break-up threshold[2] and is composed of various knock-out reactions of the ^{27}Al nucleus or Δ-resonances at higher missing energy. Only two-body break-up processes by emission of a proton or a neutron, being the largest part in the kinematic region of this experiment, will be considered in simulations of the ^{27}Al continuum.
The calculation of cross sections by off-shell electron-nucleon scattering was examined by T. DeForset [For83] in PWIA[3], where the virtual photon is absorbed by a single nucleon, with the other nucleons acting only as spectators. It is also assumed that the momentum of the virtual photon and the emerging nucleon are parallel, i.e. $\vec{q} \parallel \vec{k}'$ (*parallel kinematics*), and that *Final State Interactions* (FSI) are negligible.

2 Protons and neutrons are treated as "equal partners" to nuclear forces, but Isospin-breaking forces favour the knock-out of protons.
3 **P**lane **W**ave **I**mpulse **A**pproximation

The differential cross section for the scattered electron is written as

$$\frac{d\sigma^6}{d\Omega_e dE'_e d\Omega_p dE'_p} = k'_N E'_N \sigma_{eN} S(k_p, E_p) \tag{37}$$

where the primed variables k'_N and E'_N denote the (absolute) three-momentum and energy of the scattered nucleon escaping the residual nucleus, not to be confused with k_f, the final electron momentum, and E'_e, the final electron energy. The nucleon cross section σ_{eN} is the cross section for an unbound nucleon. To keep σ_{eN} *on-shell* while maintaining the relativistic properties of the nucleon, an effective energy of the initial nucleon was introduced yielding two different off-shell cross sections σ_{cc1} and σ_{cc2}. In this analysis the more common cross section σ_{cc1} is used. $S(k_p, E_p)$ is the spectral function of the (initial) nucleus, that describes the probability of finding a nucleon of momentum k_p and energy E_p inside the nucleus.
While k'_N , E'_N, and σ_{eN} are fixed by the kinematics and can be evaluated easily, the spectral function $S(k_p, E_p)$ is based on intrinsic properties of the nucleus. The framework of the theory provides sum rules

$$\int dk\, dE\, S_{\mathrm{N}}(k, E) = \int dk\, n_{\mathrm{N}}(k) \equiv \begin{cases} Z & \text{if N=proton} \\ (A - Z) & \text{if N=neutron} \end{cases} \tag{38}$$

$$\frac{1}{2M} \int dE\, dk\, k^2 \cdot S_{\mathrm{N}}(k, E) = \langle T \rangle \tag{39}$$

where $n_{\mathrm{N}}(k)$ is the nucleon momentum distribution and $\langle T \rangle$ the mean kinetic energy of a nucleon inside the nucleus[4].
While a precise spectral function is usually determined by theoretical calculations, some additional assumptions can help to obtain an approximate spectral function or nucleon momentum density:

1) The neutron momentum density distribution $n_n(k)$ is equal to the proton momentum density distribution $n_p(k)$, hereafter named as $n(k)$. The momentum density distributions are normalised according to Z/A for the proton and $(A - Z)/A$ for the neutron.

2) The nucleus behaves like a Fermi gas.

Most of these approximations hold for nuclei with a mass number $A \gtrsim 20$. It is also assumed, that the momenta of the nucleons inside the nucleus do not vary strongly. Considering the analogy to statistical physics, a fermionic system at temperature $T = 0$ follows a distribution of energy levels that is given by the Heaviside function $\Theta(k - k_{\mathrm{fm}})$ with the Fermi momentum k_{fm}. For a quantum mechanical system a more sophisticated way is to blur the distribution at k_{fm}. The energy dependence can be eliminated by the assumption that most of the

4 (39) is often referred to as Koltun sum rule

strength of the energy dependence in the spectral function $S(k, E)$ is located at the mean separation energy E_s

$$S(k, E) \approx n(k)\, \delta(E - E_s) \quad . \tag{40}$$

This leads to a three-parameter distribution adopted from the Fermi-Dirac theory to describe a system of fermions of the form

$$n(k) = \frac{a_0}{(\exp(c(k - k_{\mathrm{fm}})) + 1)} \quad . \tag{41}$$

The parameter a_0 is adjusted by the normalisation to the nucleon number (38), while k_{fm} can be estimated in a semi-empirical way to $k_{\mathrm{fm}} = 252\,\mathrm{MeV}$. For the determination of c, the derivative of $n(k)$ can be used to obtain a variation of $\pm 5\,\mathrm{MeV}$ at $k \to k_{\mathrm{fm}}$, an approximate error for fermi momenta of intermediate heavy-mass nuclei:

$$\left| \left(\frac{d}{dk} n(k) \right) \right| = \left| \frac{-a_0 c \exp(c(k - k_{\mathrm{fm}}))}{(\exp(c(k - k_{\mathrm{fm}})) + 1)^2} \right| \overset{k \to k_{\mathrm{fm}}}{=} 5\,\mathrm{MeV} \quad . \tag{42}$$

Merging the obtained nucleon momentum distribution into (37) , the quasi-elastic continuum can be simulated including proton and neutron knock-out processes.
In order to investigate and improve the model of quasi-elastic scattering on ^{27}Al, all simulations so far containing elastic scattering on ^{27}Al and ^{4}He and quasi-elastic scattering on ^{27}Al are added to a combined simulation and compared to data. In this combined simulation $s(x, a)$ the part of quasi-elastic scattering on ^{27}Al was allowed to float by a constant factor a optimised to data:

$$s_{\mathrm{comb.}}(m_{\mathrm{miss}}, a) = s_{\mathrm{He\ el.}}(m_{\mathrm{miss}}) + s_{\mathrm{Al\ el.}}(m_{\mathrm{miss}}) + a \cdot s_{\mathrm{Al\ qu.el.}}(m_{\mathrm{miss}}) \quad . \tag{43}$$

Fig. 29 shows the region where the quasi-elastic continuum begins in the missing mass representation of ^{4}He. The break-up energy, i.e. the beginning of the continuum, is reproduced properly. The continuum of ^{27}Al extends to the ^{4}He elastic peak and its tail, making an absolute comparison and the distinction between these simulations difficult. In Fig. 30 the scaling factor a is shown in dependence of Q^2 for all empty-cell measurements in this experiment. Data and simulation show good agreement in the intermediate region of Q^2, where only little scaling is needed. At high and low Q^2, where the statistics of the data deteriorates, the agreement gets worse. To check the constistency, this procedure was also repeated for the production data to improve the model with better statistics.

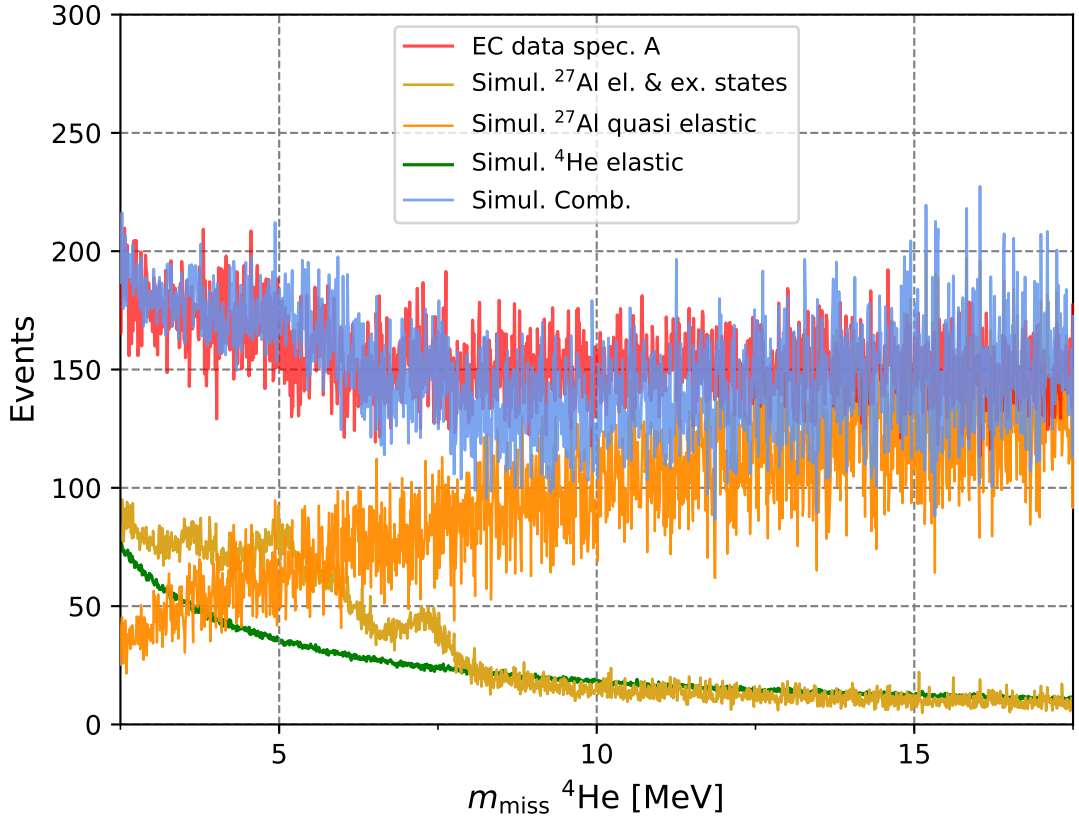

Figure 29: Comparison of data and quasi-elastic simulation of ^{27}Al in missing mass representation of ^{4}He. The radiative tails of ^{4}He and ^{27}Al, also added, decrease strongly while the ^{27}Al continuum increases steadily. In regions of higher missing mass quasi-elastic processes are dominating in the background. Smaller bumps in the simulation of ^{27}Al (yellow) belong to excited states of ^{27}Al. The combined simulation with optimised scaling a is shown in blue.

5.5 RESULTS OF EMPTY-CELL AND BACKGROUND STUDIES

By combining all parts of the background simulations, it is possible to completely reproduce the empty-cell data, including the elastic peak of ^{27}Al, the excited states of ^{27}Al, and the continuum, as well as the elastic peak of the residual ^{4}He gas in the cell.
Fig. 31 shows a typical ^{27}Al missing mass spectrum at a scattering angle $\theta = 24°$ and beam energy E = 690 MeV. The vertical lines labeled with numbers indicate the excited states or groups of excited states of ^{27}Al (listed by label in Tab. 3). With a spectrometer resolution of about $\delta \approx 2 \cdot 10^{-4}$ the first excited states of ^{27}Al can be reliably identified and compared to those given in [Bas11], lines at 5,7 and 8 are a combination of several states merged into one peak in the simulation. The number of excited states of ^{27}Al grows significantly at higher energy and makes a distinction more complicated in the missing mass spectrum. The elastic peak of ^{4}He, centered at around 7.5 MeV, overlaps with the excited states of ^{27}Al and makes a separation even more difficult. The position

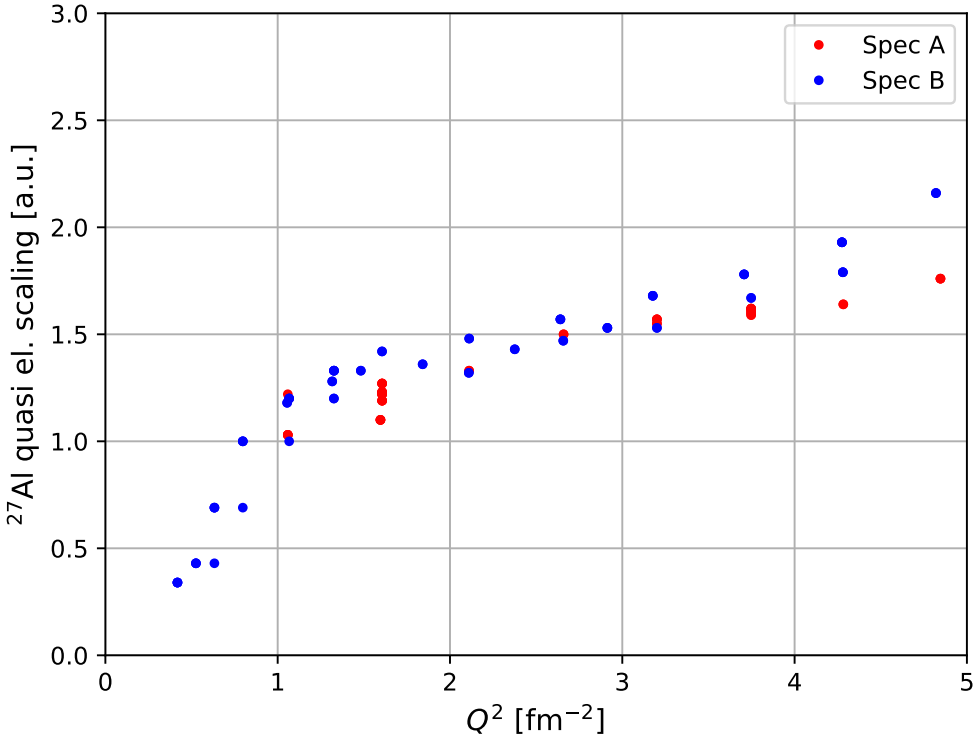

Figure 30: The scaling factor a (43) for spectrometer A and B. The largest deviation from data appears at low and high Q^2: lacking statistics in the empty-cell data can explain this behaviour. To achieve a high level of consistency, this factor was determined again in the production data.

is then on one hand determined by comparison to [Bas11] and by proceeding gradually from setup to setup with increasing Q^2. Fig. 32 shows the missing mass spectrum of ^{27}Al from an empty-cell setup with a scattering angle of 25.6° and a beam energy of 795 MeV. Here, the central momentum of spectrometer B is here to its maximum and the resolution of the excited states worsens due to saturation effects at a high magnetic field. At high Q^2-kinematics the statistics is also limited. The kinematic approaches a region, where the yield of excited states of ^{27}Al becomes comparable in magnitude to the elastic peak.
The examination of the empty-cell setups covers a wide range of typical processes observed in electron scattering. The combination of these processes to an effective model for cell background is a benefit for the analysis, because further software cuts for background separation are no longer necessary.

^{27}Al state	E_x [MeV]	J^π
1	0.844	$1/2^+$
2	1.015	$3/2^+$
3	2.212	$7/2^+$
4	2.735	$5/2^+$
5	2.982	$3/2^+$
	3.004	$9/2^+$
6	3.680	$1/2^+$
7	3.957	$3/2^+$
	4.054	$1/2^-$
8	4.410	$5/2^+$
	4.510	$11/2^+$
	4.580	$7/2^+$
9	4.812	$5/2^+$
10	5.510	$3/2^-$

Table 3: Excited states of ^{27}Al incorporated into the simulation of the aluminium cell with excitation energy $E_{\text{ex.}}$ and spin/parity quantum numbers J^π.

Up to this point, the analysis and the simulation of the elastic peak of ^{4}He played only a minor role. In order to simulate the elastic peak of helium, the form factor model from Otterman et al. [OKM+85] was used. The elastic peak of ^{4}He and its importance in the analysis will be examined in more detail in the next chapter.

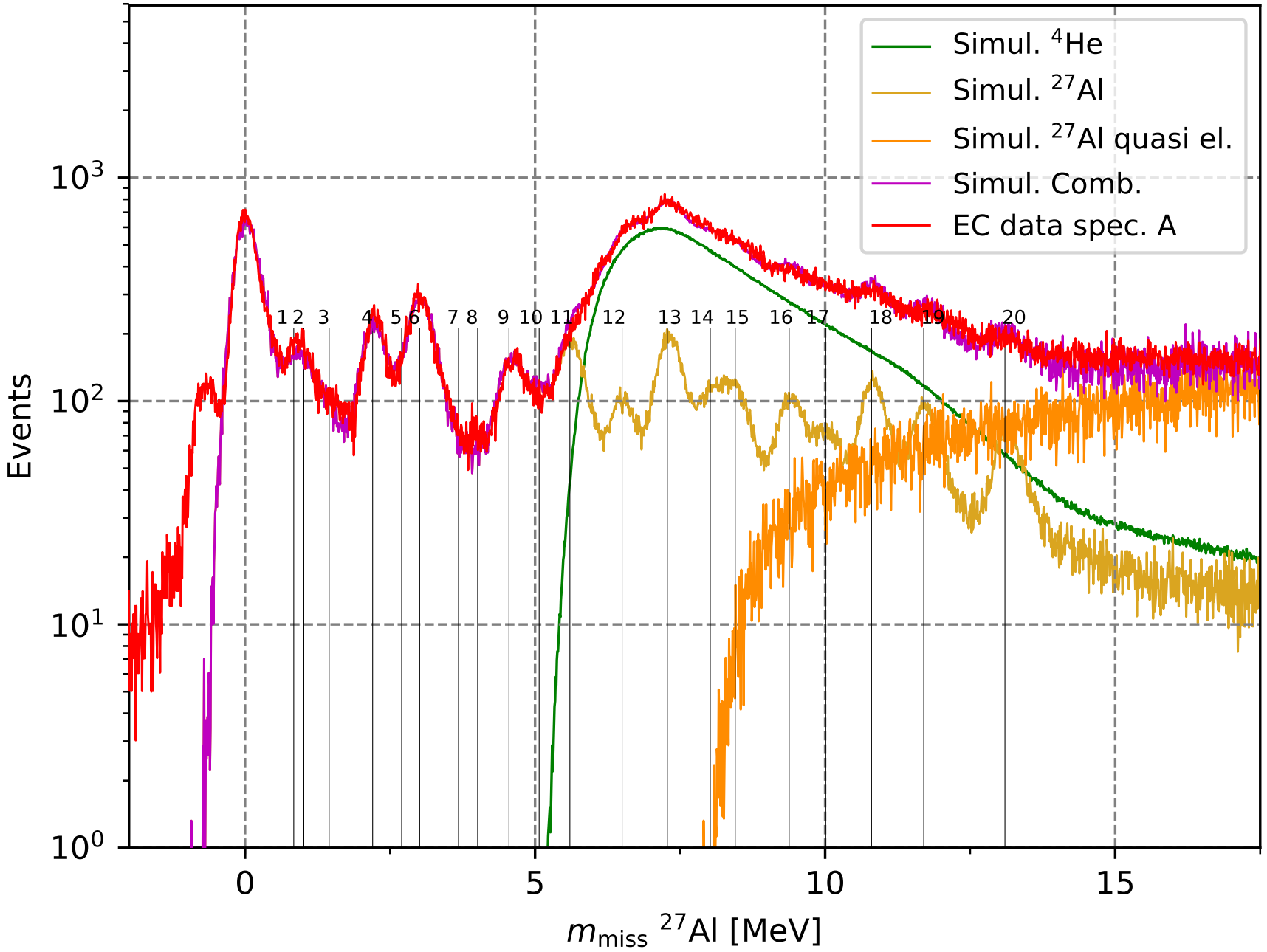

Figure 31: Complete spectrum of the empty-cell measurement at 690 MeV and 24°. The excited states of ^{27}Al are indicated by thin black lines. The ^{4}He elastic "bump" shown in green is washed-out in the missing mass representation of ^{27}Al. The continuum of ^{27}Al is shown in orange.

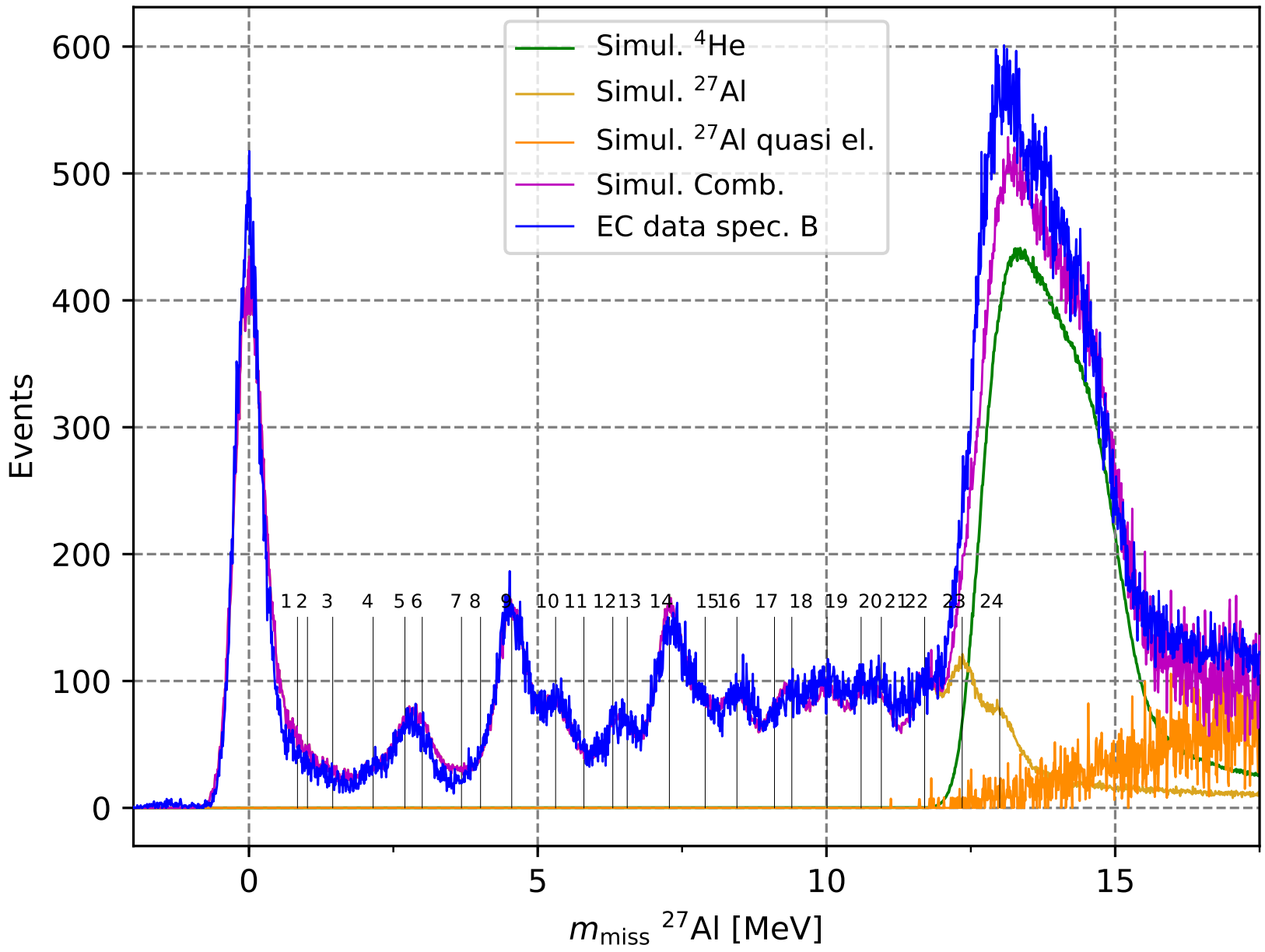

Figure 32: Complete empty-cell spectrum at beam energy 795 MeV and $\theta = 25.6°$. At higher energy transfer the excited states' yields increase and become comparable to that of the elastic peak. With increasing central momentum, it becomes more difficult to resolve single energy levels.

6

^{4}HE FORM FACTOR RATIOS

6.1 INTRODUCTION

Nuclear form factors can be extracted from the relevant differential cross sections for various Q^2 including background subtraction and detector efficiency (see Sec. 4.6):

$$|\mathcal{F}_{M0^+}(Q^2)|^2 = \frac{\left(\frac{d\sigma}{d\Omega}\right)_{exp}}{\left(\frac{d\sigma}{d\Omega}\right)_{Mott}} \tag{44}$$

For the determination of the transition form factor $|\mathcal{F}_{M0^+}(Q_0^2)|^2$, the procedure requires some additional steps due to the more complicated localisation and shape of the resonance in the spectra:

1. Contributions of the aluminium cell and the radiative tail of the ^{4}He elastic peak have to be subtracted from the data.
2. A first model of the transition form factor relative to the elastic form factor is developed using sophisticated models for the break-up continuum of ^{4}He.
3. A second iteration of the form factor ratio is performed to improve the model by simulating a more accurate Q^2 which serves as input for more precise simulations.
4. Monte-Carlo simulations with different parametrisations for the monopole resonance are developed and compared to the data. These simulations include radiative effects and energy loss, typical for electron scattering experiments, and try to emulate the data. Missing parameters required as input for the simulations are determined by adjustement to data.
5. These simulations are used to emulate the data in an extended m_{miss}-range to decrease the deviations of the initial transition form factor and obtain more precise results.

All these procedures follow in detail in the next sections and chapters.

6.2 ^{4}He and ^{27}Al elastic tail and ^{27}Al quasi-elastic background contribution

The first subtraction of background removes the radiative tails of ^{4}He and ^{27}Al from electrons scattering elastically on the target from the spectra, and also contributions from quasi-elastic scattering on ^{27}Al, respectively. In Fig. 33 the part of the ^{4}He m_{miss}-spectrum before the ^{4}He-continuum threshold is shown.

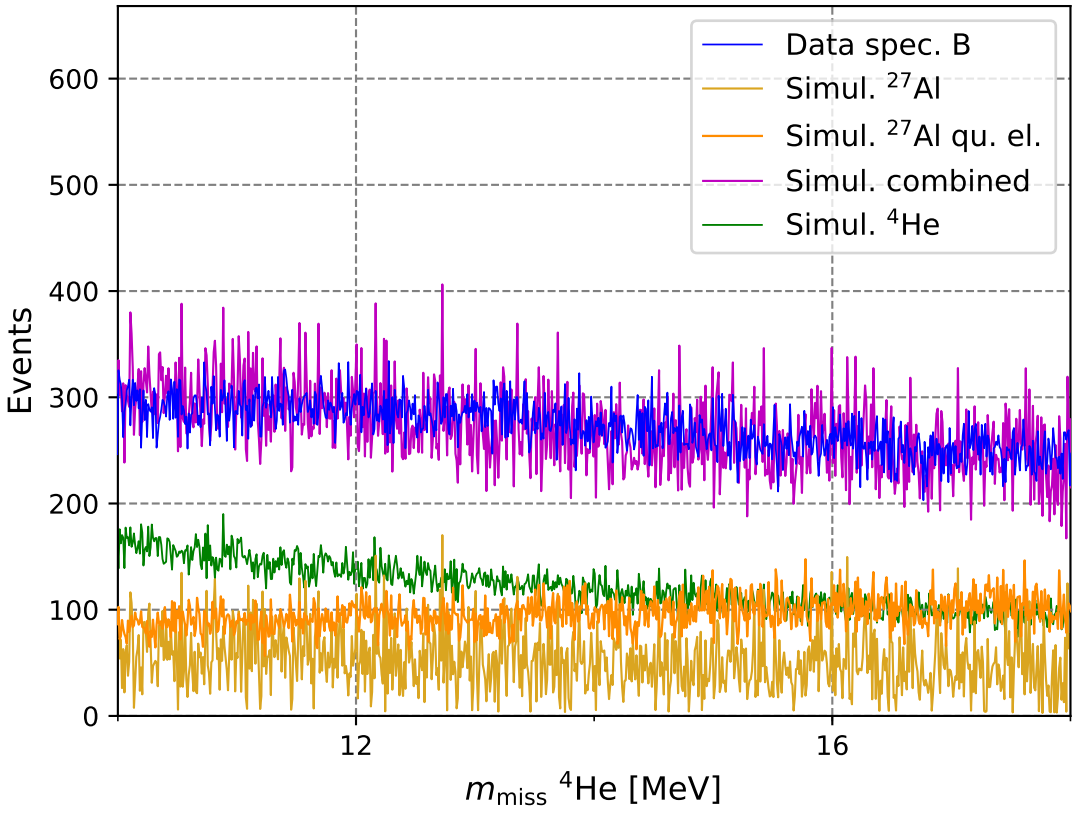

Figure 33: Background from ^{4}He and ^{27}Al below the continuum in missing mass representation. The ^{27}Al radiative tail is the smallest part, the ^{4}He radiative tail and the quasi-elastic ^{27}Al continuum are comparable in magnitude for the case of empty-cell measurements.

These background contributions extend to the ^{4}He continuum and are continued by simulations. This combination includes the simulation of elastic scattering on ^{4}He, elastic scattering on ^{27}Al and its excited states, as well as a simulation of quasi-elastic scattering on ^{27}Al. To achieve a smooth background subtraction, high computation costs would be required to avoid spikes caused by low statistics of the simulation. Instead, an appropriate model was used to fit the combined simulations (Fig. 33) and subtract a such obtained fit curve from the data.

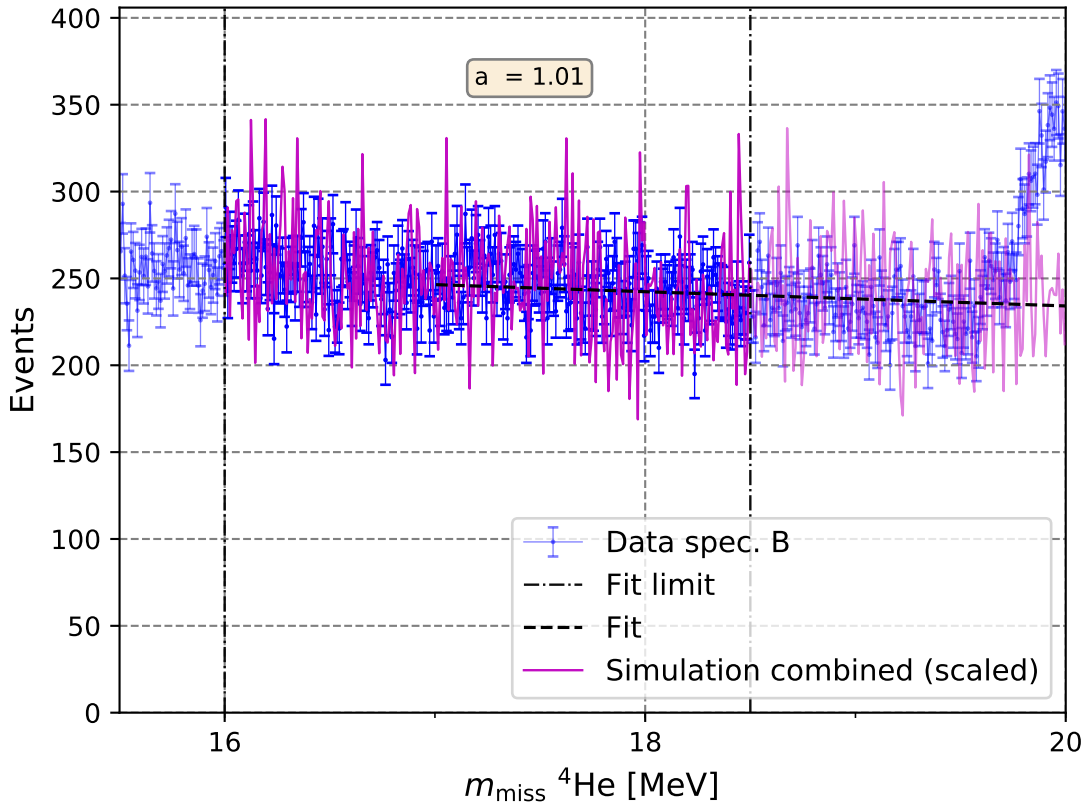

Figure 34: Section of m_{miss} close to the continuum. At 19.5 MeV the left tail of the monopole appears.

Fig. 34 shows an exemplary fit to the backgrounds. Before the fit, the combined simulation is scaled by a constant factor a determined in the range from 16 MeV to 18 MeV. Fig. 34 shows the truncated part in which the combined simulation is adjusted to data. The scaling factor is in this case $a = 1.01$, which means the combined simulation differs from the data by about 1%. The deviation obtained by a is in general observed to be very small, indicating that the simulations already have a good agreement with the data. After the combined simulation was corrected, the following model is used to fit the background:

$$f(m_{\text{miss}}) = \mathcal{A} \cdot \exp(b \cdot m_{\text{miss}}) + m \cdot m_{\text{miss}} + c. \tag{45}$$

The fit region is limited to an area between 17 MeV and 30 MeV. Larger values of missing mass are not relevant for the scope of this analysis (see Fig. 35). The result of the above described background subtraction is shown in Fig. 36 with the distinctive monopole centered at $m_{\text{miss}} = 20.21$ MeV.

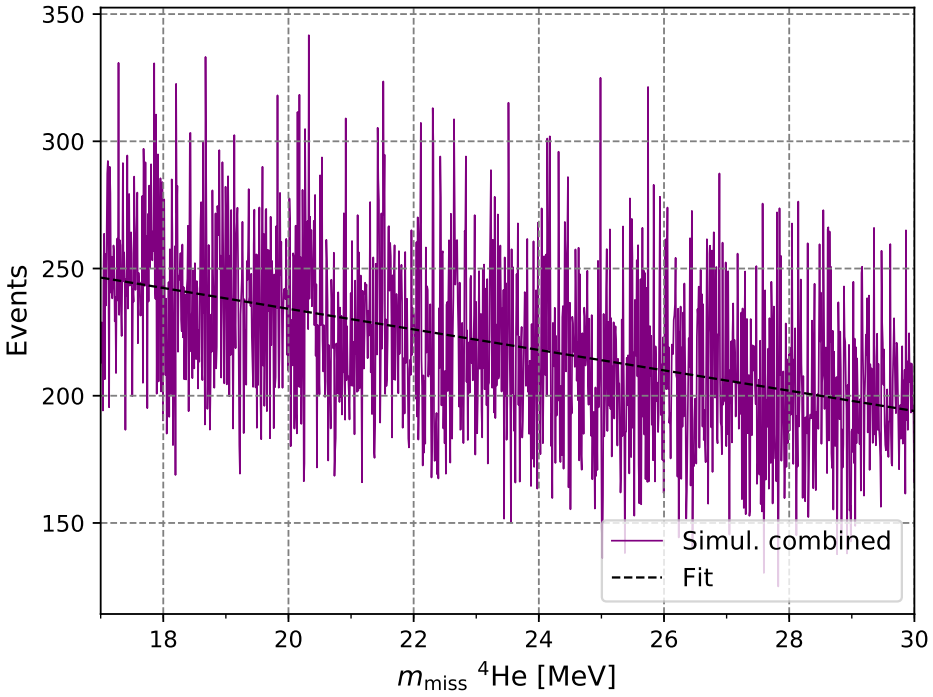

Figure 35: The combined simulation is fitted to extrapolate the background under the continuum smoothly. The fit extends from 17 MeV to 30 MeV. Larger $m_{miss} > 30$ MeV are not of interest for the further analysis and therefore are not considered.

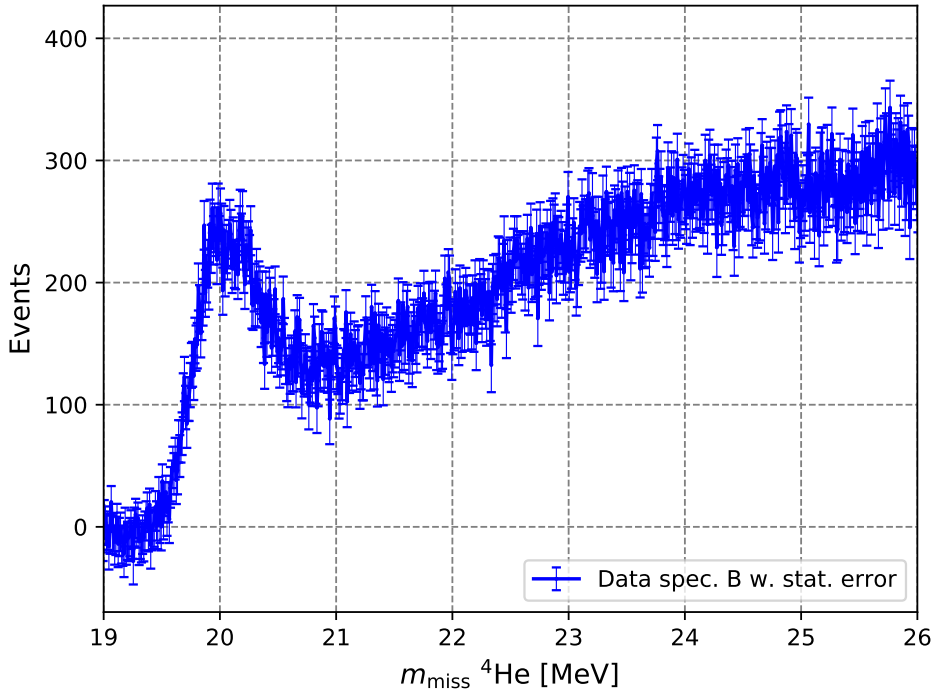

Figure 36: The monopole resonance located at the beginning of the continuum. All the contributions from ^{27}Al and the ^{4}He radiative tail have been subtracted.

6.3 ^{4}HE CONTINUUM BACKGROUND

After separating the background of the aluminium cell and the elastic processes of ^{4}He, the next task is to separate the ^{4}He-continuum from the resonant state. For this purpose a model for the continuum valid for the whole range of Q^2 needs to be found. This requires knowledge of knock-out reactions and other resonances of ^{4}He. An attempt to simulate the part of the quasi-elastic scattering processes on ^{4}He is described in App. B. This description of the continuum lacks in reliability and therefore was not used in the analysis: A giant resonance with quantum numbers $J^\pi = 1^-$ appears on top of the continuum at 25.95 MeV and is a dominant part of the background. Other resonances exist as well, but their Q^2-dependence is difficult to estimate, as well as other properties like their width and excitation energy. This requires to model the continuum with appropriate fit models.
For the resonance itself, the skewed Moyal function is in a first instance used to model the radiation losses, causing the resonance to deviate from the symmetric Breit-Wigner shape:

$$M0(m_{\text{miss}}) = \frac{\mathcal{A}}{\sqrt{2\pi}\sigma} \exp\left(-\frac{1}{2}\exp(-\frac{(m_{\text{miss}}-\mu)}{\sigma}) - \frac{(m_{\text{miss}}-\mu)}{2\sigma}\right) . \tag{46}$$

In order to achieve the vanishing of the continuum at the threshold of 19.815 MeV, an approximate Heaviside function was used:

$$\Theta_{\text{App}}(m_{\text{miss}} - x_0) = \frac{1}{\pi}\left(\arctan(a \cdot (m_{\text{miss}} - x_0)) + \frac{\pi}{2}\right) \ , \ a > 3 \ . \tag{47}$$

This function offers a smooth fade-out of the fit around the proton knock-out threshold and avoids numerical instability by a sharp "step-function" with discontinuous derivatives. The parameter a depends on the background model that is used, x_0 is constrained by the threshold of proton break-up of ^{4}He (E_p = 19.815 MeV) and the central value μ of the Moyal distribution with amplitude $\mathcal{A}$ and width σ. The two functions in (46) and (47) are part of every fit model presented in the following.

Background model 1

In the publication of Köbschall et al. ([KOM+83]) the fit model for the background subtraction was explicitly given as

$$f_{bg,KS}(m_{\text{miss}}) = \sum_i a_i (m_{miss} - E_p)^{i/2} \quad i = 0,1,2,3 \tag{48}$$

with $E_p = 19.815\,\text{MeV}$ as proton-threshold. In order to adopt (48) to already performed background subtractions, the function was modified to the following form:

$$f_{bg1}(m_{\text{miss}}) = \Theta_{\text{App}}(m_{\text{miss}} - E_p) \cdot a \cdot (|m_{miss} - E_p|)^{1/n}\ ,\ n \in \{\, \mathbb{R}^+ \mid n > 1\}. \tag{49}$$

Orders $i = 0, 2$ were omitted in (49), assuming that constant and linear parts were already subtracted by the tail contribution (see Sec. 6.2). In addition, exponents $i = 1, 3$ are combined to one parameter $n \in \mathbb{R}^+$ to be optimised, yielding (49) as model function for the remaining background. A fit of this function to data is shown in Fig. 37.

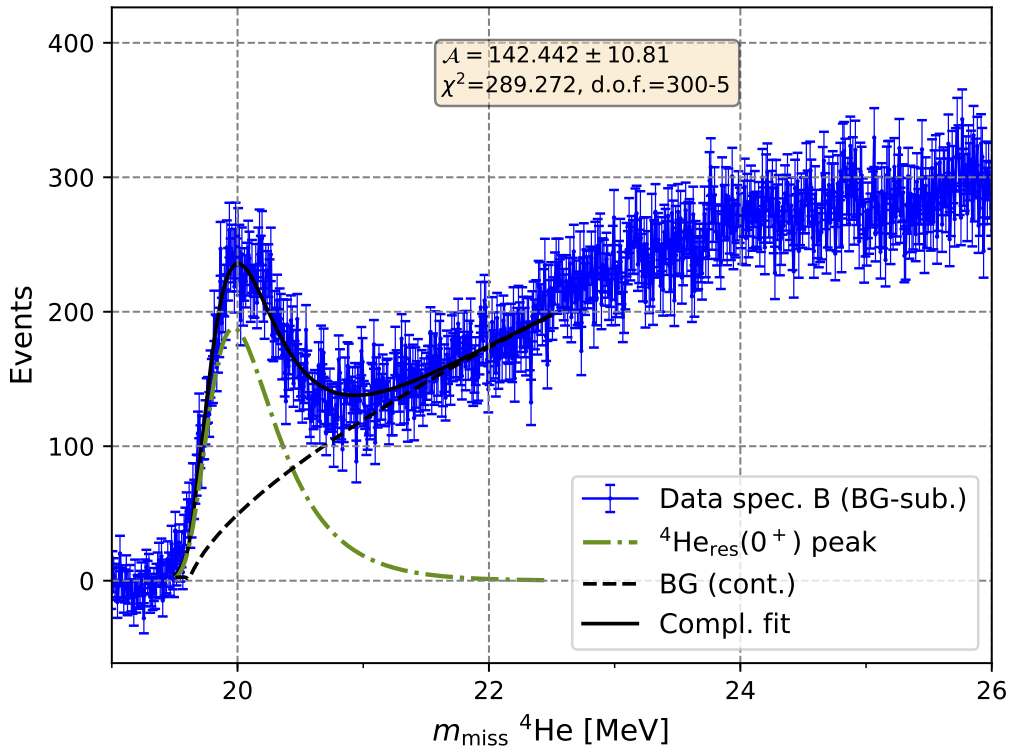

Figure 37: The fit model for monopole resonance and background by (49) compared to data with statistical error bars only. χ^2 and amplitude $\mathcal{A}$ are shown in the inset.

With the assumption of broad resonances occuring in the continuum of ^{4}He, a shallower tail progression fits the continuum better than a function $\propto x^{1/n}$. Though (49) is not used in this analysis, it serves as a first benchmark to compare to other models that exhibit this feature.

Background model 2

In a simple and stable approach, the continuum can be fitted with a linear function in the region close to the proton break-up threshold ($E_p = 19.815\,\mathrm{MeV}$):

$$f_{bg2} = \Theta_{\mathrm{App}}(m_{\mathrm{miss}} - E_p) \cdot \left(m \cdot (m_{\mathrm{miss}} - E_p) + n\right) \quad . \tag{50}$$

However, this approximation is limited: The continuum begins to approach a maximum at higher m_{miss} and thus the fit would lead to erroneous results. The fit region is therefore limited up to $m_{\mathrm{miss}} \leq 22\,\mathrm{MeV}$. In the truncated range this model is in good agreement with the data while only requiring a minimal set of parameters. Fig. 38 shows an example fit of (50), applied to the same data set as shown Fig. 37.

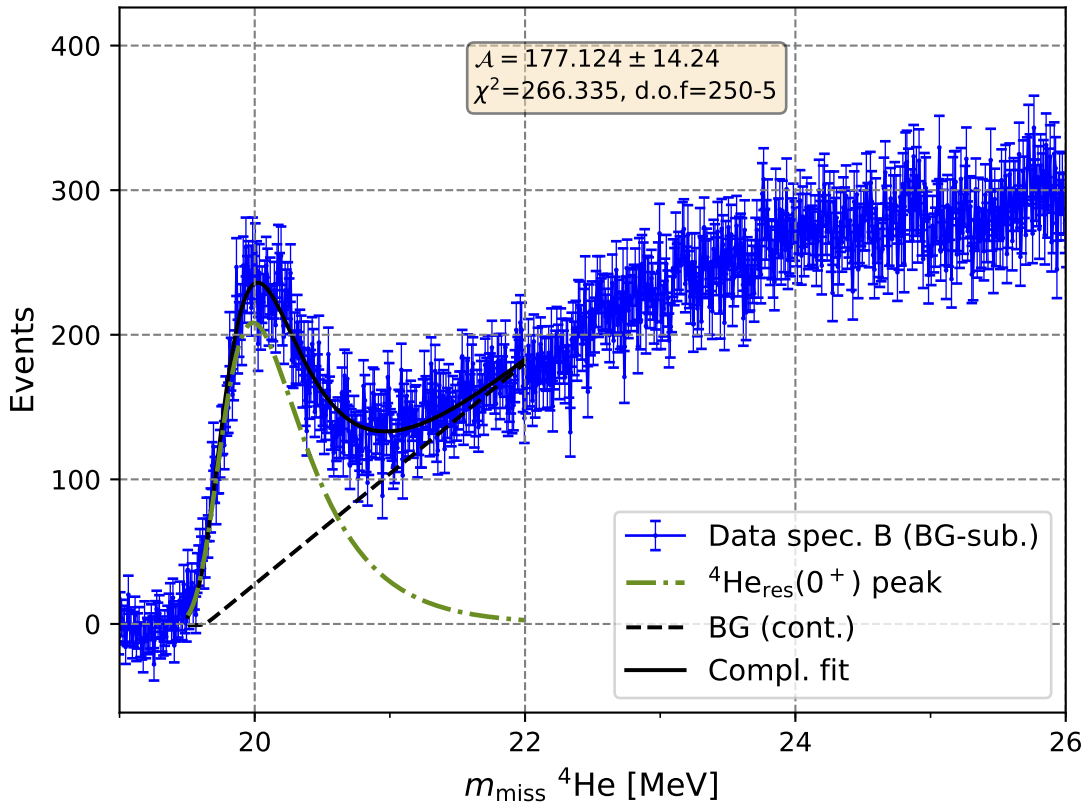

Figure 38: The fit model for the monopole resonance and background given by (50) and data with statistical error. χ^2 and amplitude $\mathcal{A}$ are shown in the inset.

Background model 3

The ^{4}He spectrum exhibits a broad giant resonance at 25.95 MeV [TWH92] with spin quantum numbers $J^P = (1^-)$ that can easily be excited by one-photon exchange at low Q^2. In order to include contributions of the giant resonance into the background model, the following function was constructed:

$$f_{bg3}(m_{\text{miss}}) = \Theta_{\text{a}}(m_{\text{miss}} - E_p) \cdot G(m_{\text{miss}}, \mathcal{A}, \sigma, \mu) \cdot \widetilde{\Theta}(m_{\text{miss}} - E_p) \tag{51a}$$

$$\widetilde{\Theta}(m_{\text{miss}} - E_p) = \Theta_{\text{App}} \cdot \Big(1 - \exp\big(b \cdot (m_{\text{miss}} - E_p) \cdot \Theta_{\text{App}}\big)\Big) \tag{51b}$$

In (51a) the influence of the resonance is represented by a Gaussian function $G(m_{\text{miss}}, \mathcal{A}, \sigma, \mu)$ with amplitude $\mathcal{A}$, central value μ and standard deviation σ. The modified, approximate Heaviside function $\widetilde{\Theta}(m_{\text{miss}} - E_p)$ forces the left side of the Gaussians tail to vanish at the threshold $E_p = 19.815\,\text{MeV}$ to avoid extending the contributions of the giant resonance's tail into areas of $m_{\text{miss}} < 19.815\,\text{MeV}$. Even if the function in (51a) is rather different from the linear background model in (50), they do not differ much in the result on the amplitude parameter $\mathcal{A}$.
Fit model 3 from (51a) is shown in Fig. 39 together with data also shown in Fig. 37 and Fig. 38.

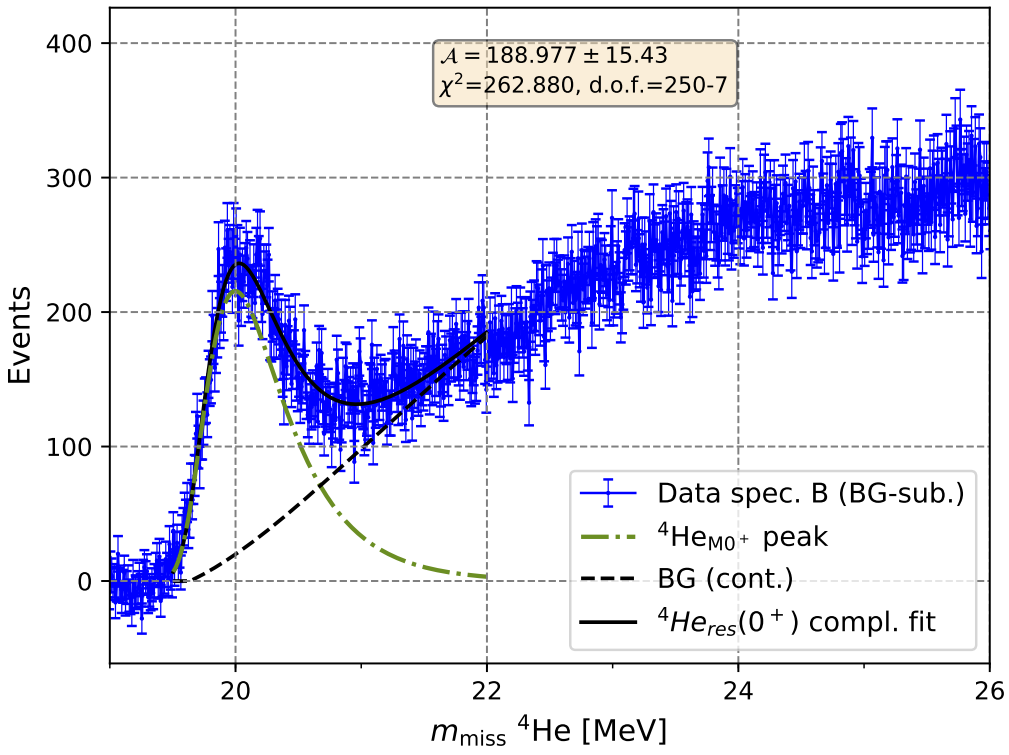

Figure 39: The fit model for the monopole resonance and background given by (51a) and data with statistical error. χ^2 and amplitude $\mathcal{A}$ are shown in the inset.

All described fit models, summarised in Tab. 4, are suitable for the background subtraction of the ^{4}He continuum. Due to their similarity and the structure of the continuum, background (BG) models 2 and 3 are preferred to be used in the further analysis.

Background model	Description	No. of free Param.	Eq. reference
BG1	root-like	2	(49)
BG2	linear	2	(50)
BG3	Gaussian tail	4	(51)

Table 4: Summary of the employed background models.

6.4 RATIO OF MONOPOLE- TO ELASTIC FORM FACTOR

The background models described in Sec. 6.3 are used to determine the transition form factor relative to the form factor of the ground state. Background models 2 and 3 have both shown numerical stability and agreement with the data. The difference when using background model 2 or 3 to determine the monopole integral (given by $\mathcal{A}$ in (46)) was shown to be very small (see Fig. 38 and Fig. 39). However, background model 3 with a gaussian tail is the more appropriate choice to describe broad resonances covering the continuum of ^{4}He. Background model 2 will be used as benchmark to test for model dependencies.

A small and narrow m_{miss}-cut of $\delta_{\text{ratio}} \pm 0.24\,\text{MeV}$ around the maximum of both, the elastic and monopole peak, to determine the monopole transition form factor relative to the elastic peak is applied. The value of the cut is chosen based on the monopole width of 0.24 MeV given by Köbschall et al. [KOM+83] to cover two *full-width-half-maxima* of the monopole. The events of both peaks passing this cut are then used to determine the ratio:

$$|\mathcal{F}_{\text{ratio}}(Q_0^2)|^2 = \frac{\int_{\delta_{\text{ratio}}} \text{resonance}}{\int_{\delta_{\text{ratio}}} \text{el. peak}} \quad . \tag{52}$$

A schematic picture of elastic and monopole peak with the applied cut range is shown in Fig. 40. The cut limits are indicated around pseudodata of elastic peak and monopole by the coloured area.

A first determination of the transition form factor relative to the elastic peak with a narrow cut eliminates two difficulties: Unnoticed variations in luminosity concern elastic peak and monopole resonance in the same manner and compensate each other when determining a relative quantity. The second issue of radiative effects observed in electron scattering is minimised by applying a very narrow cut around the peak maxima.

It is important to note the different squared four-momenta of elastic peak $\widetilde{Q}^2$ and monopole resonance Q_0^2. Both peaks are separated by around 20 MeV in

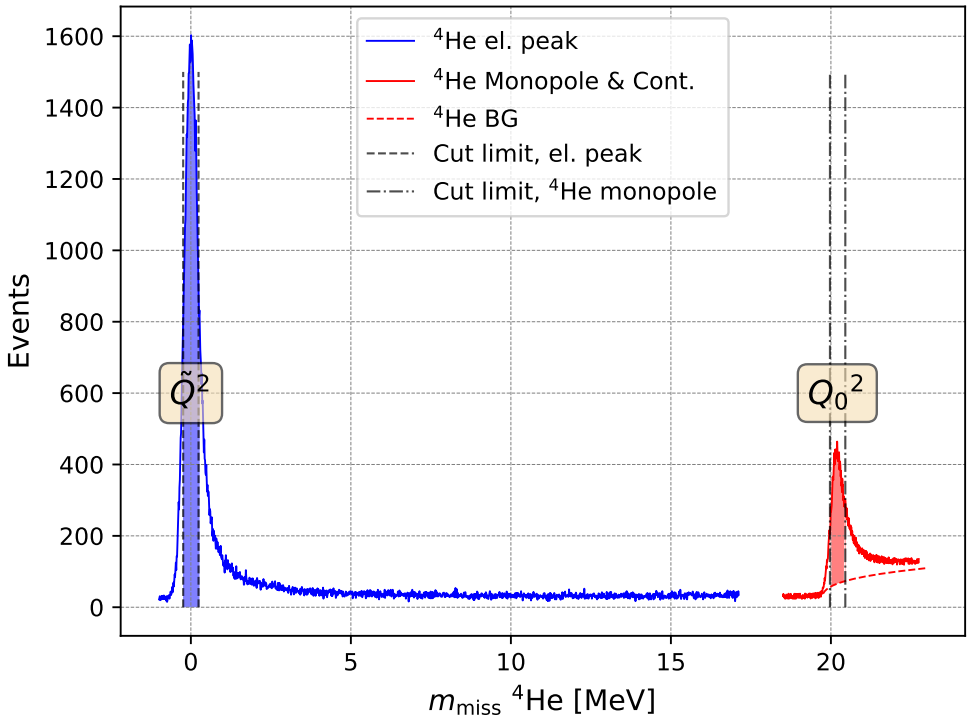

Figure 40: A schematic picture of the ratio determination with pseudo-data (not to scale). The monopole's background is indicated by the dashed red line. Both peaks exhibit different Q^2 which is accounted for in the form factor ratio.

the m_{miss}-spectrum leading to a slight but significant difference of the squared four-momenta. This is corrected by a factor $\phi(\tilde{Q}^2, Q_0^2)$, which accounts for the different elastic form factor at $\tilde{Q}^2$ compared to Q_0^2:

$$|\mathcal{F}_{\mathrm{ratio}}(Q_0{}^2)|^2 = \frac{\int_{\delta_{\mathrm{ratio}}} \text{resonance}}{\int_{\delta_{\mathrm{ratio}}} \text{el.peak} \cdot \phi(\tilde{Q}^2, Q_0{}^2)} \tag{53a}$$

$$\phi(\tilde{Q}^2, Q_0{}^2) = \frac{|\mathcal{F}_{\mathrm{g.s.}}(Q_0{}^2)|^2}{|\mathcal{F}_{\mathrm{g.s.}}(\tilde{Q}^2)|^2} \tag{53b}$$

The parametrisation of Otterman et al. [OKM+85] is used to evaluate the ^{4}He elastic form factor. Four-momenta of a particular kinematic are evaluated as median of a distribution. The large angular acceptance of spectrometer A elongates the distribution to higher Q_0^2. This can lead to a different central Q^2 in both spectrometers, although they are placed at the same central angle. Fig. 41 shows this effect for spectrometer A and B placed at the same scattering angle $\theta = 24.0°$ and beam energy of 690 MeV.

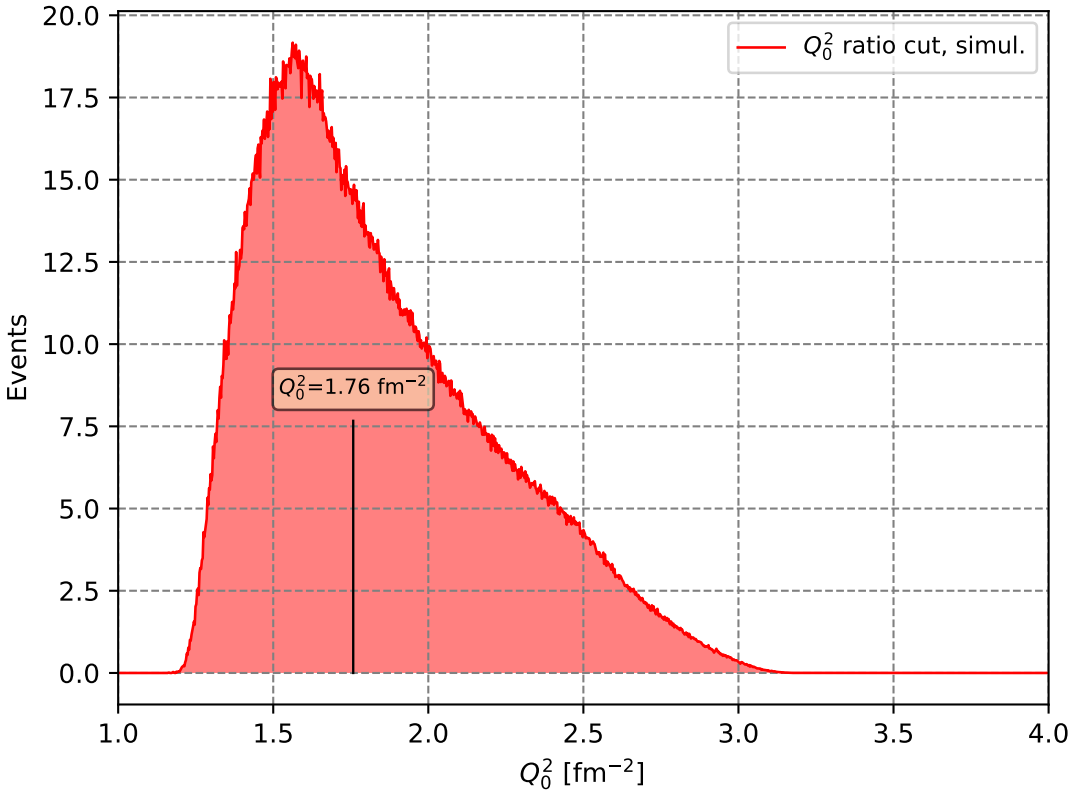

(a)

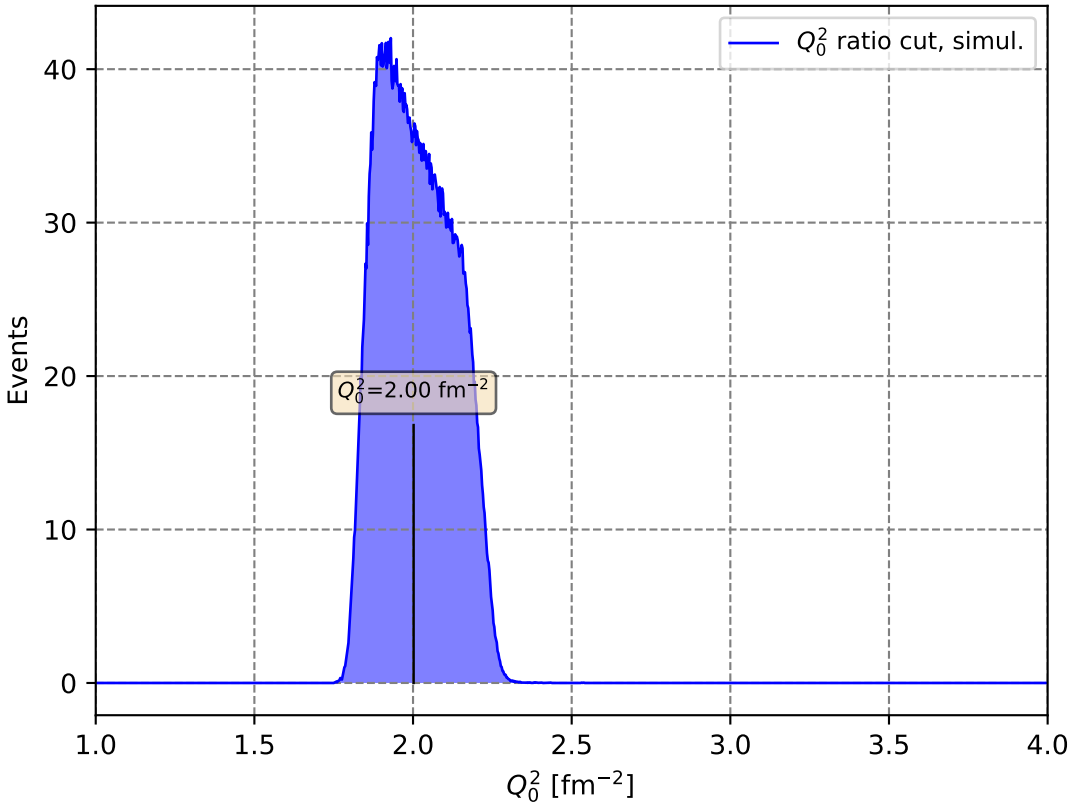

(b)

Figure 41: Q_0^2 distribution with ratio cut ± 0.24 MeV around the resonance maximum for spectrometer A *(a)* and B *(b)*. Although the Q_0^2 distributions for both spectrometers are determined at the same central angle $\theta = 24.0°$, they show a different shape. This results in a different central Q_0^2.

A polynomial of $\mathcal{O}(4)$ without constant term is used to fit the transition form factor ratio:

$$P_{\text{ratio}}(Q_0^2) = a_4 \cdot Q_0^4 + a_3 \cdot Q_0^3 + a_2 \cdot Q_0^2 + a_1 \cdot Q_0 \tag{54}$$

To determine the form factor ratio more precisely, one can repeat this procedure. This subdivides the determination of the transition form factor ratio in two iteration steps: a first iteration step, determining the from factor ratio solely by data, and a second iteration step using a simulation to improve the central value of Q_0^2. In this simulation, the transition form factor ratio of the first iteration, parameterised by (54), can already be embedded. The central Q_0^2 value is then determined by the simulated, background-free Q_0^2-distribution and not by the Q_0^2-distribution from data, where the latter one may also lack in statistics. Another advantage of this second iteration step with a simulated Q_0^2-distribution is the correct treatment of the form factor variation over the spectrometer's complete angular acceptance. The collimators of the spectrometers spread over a few degrees and do not allow to measure an infinitesimal angular phase space. But the difference of a few degrees in the mott cross section can lead to a significant variation of count rates, additionally enhanced by the variation of the form factor[1]. Fig. 42 shows the transition form factor ratio obtained in a first iteration step solely by data (see Fig. 42a) and in a second iteration step improved by a simulated Q_0^2-distribution (see Fig. 42b).
The differences between the points of spectrometer A and B after the second iteration, shown in Fig. 42b, are now decreased.
A further improvement of precision when determining the transition form factor can be achieved by using Monte-Carlo methods with appropriate resonance parametrisations and extending the m_{miss}-cut (see Chap. 7).

6.4.1 *Error estimates of* $|\mathcal{F}_{\text{ratio}}(Q_0^2)|^2$

The elastic from factor of ^{4}He contributes as factor to the calculation of the transition form factor ratio and is given by the authors in [OKM+85] with an uncertainty of 0.5% in the kinematic region of this experiment. The error from the background subtraction can be estimated as 1.0% by the uncertainty of the scaling factor a. The dominating systematic uncertainty originates from the cut limit of $\delta_{\text{ratio}} \pm 0.24\,\text{MeV}$ around the peak maxima. In order to minimise the influence of radiative effects on both of the peaks, the cut is kept close to the maxima. A variation on this cut by using a different width of $\Gamma = 0.27\,\text{MeV}$ obtained by [Wal70] yields a systematic uncertainty of 3.5%. These systematical errors were added to an overall uncertainty of 5% and added to the statistical error in the plots of Fig. 42.

1 This effect is less dramatic for the monopole transition form factor compared to e.g. the elastic form factor of ^{4}He. The effect still has to be considered for spectrometers with a large angular acceptance like spectrometer A.

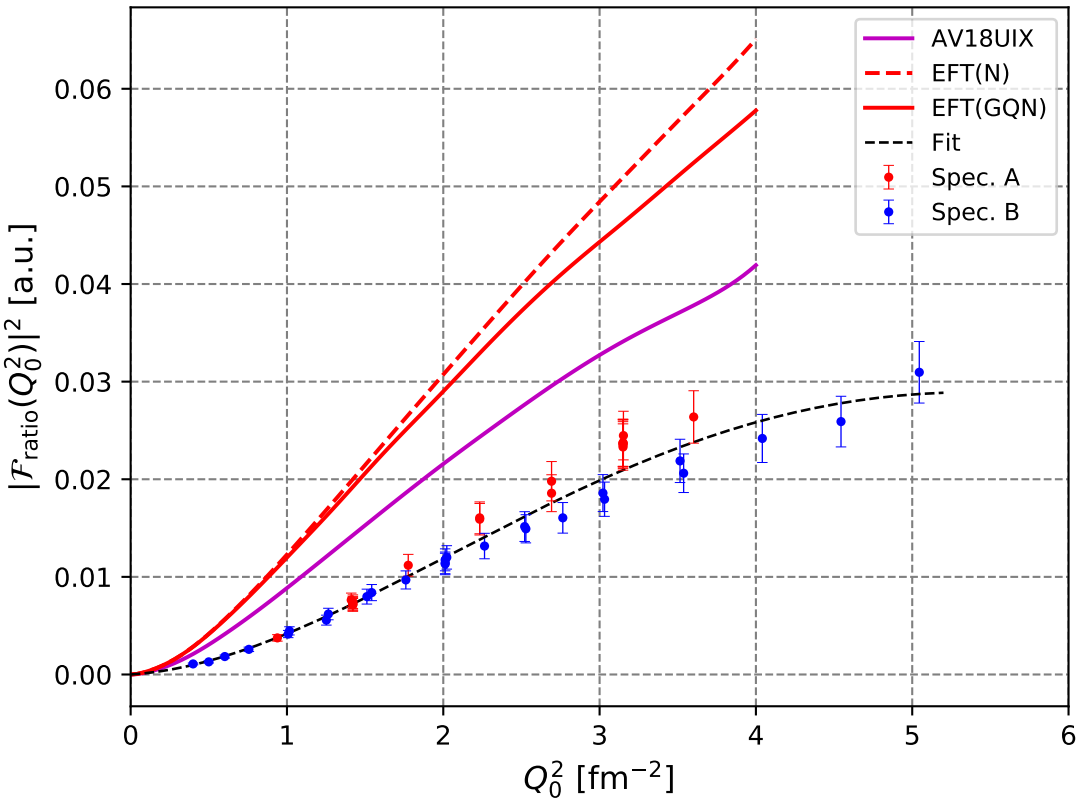

(a)

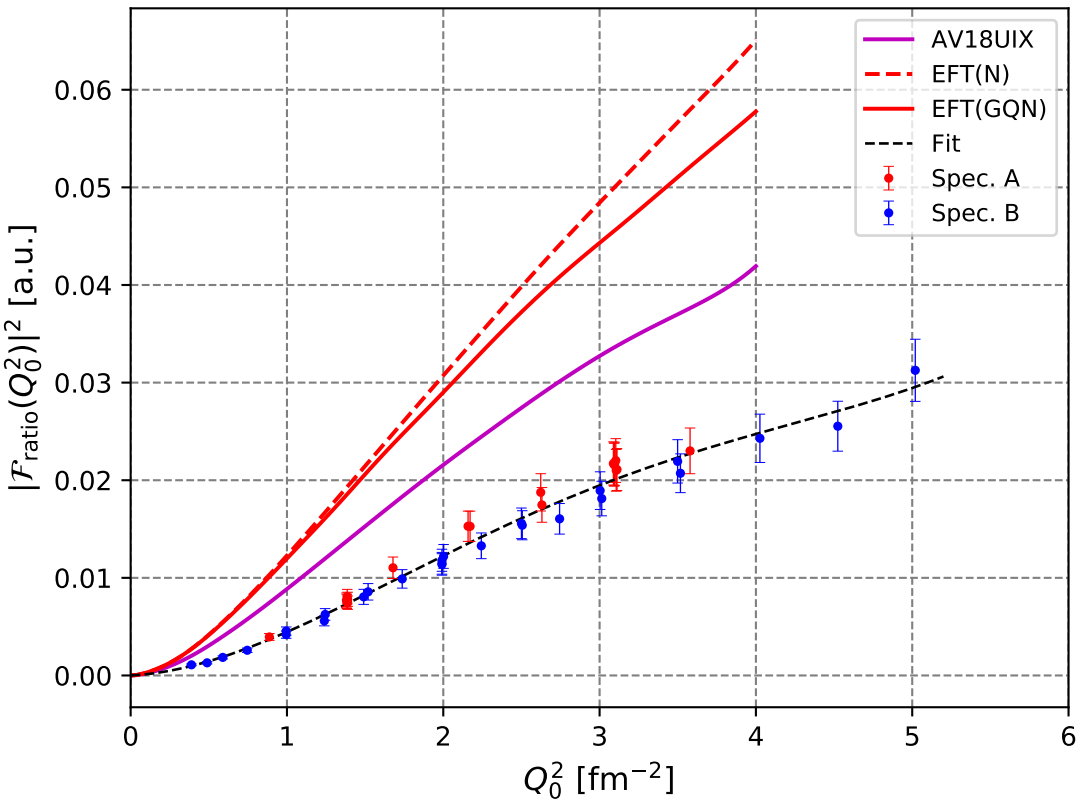

(b)

Figure 42: Transition form factor ratio $|\mathcal{F}_{\text{ratio}}(Q_0^2)|^2$ as a function of Q_0^2 for the 1$^{\text{st}}$ *(a)* and the 2$^{\text{nd}}$ *(b)* iteration with theoretical ratios for different potentials calculated by S. Bacca [Bac18].

7

SIMULATION OF THE ^{4}HE MONOPOLE RESONANCE

7.1 RESONANCE SHAPE PARAMETRISATIONS

The description of resonances in nuclear physics began with the work of G. Breit and E. Wigner [BW36], assuming the resonance to be an exponentially decaying state. Hence, the cross section is proportional to the Breit-Wigner formula (Sec. 2.1) in its fundamental form given as:

$$\left(\frac{d\sigma}{dE}\right) \propto \frac{\Gamma_0}{(E-E_0)^2 + \frac{\Gamma_0^2}{4}} \quad . \tag{55}$$

Effects of finite spectrometer resolution, energy loss and radiative corrections affect Γ_0 and lead to a broadening of the line-shape in general. This fading can be described by convolving the Breit-Wigner profile $B(x,\Gamma_0)$ with a Gaussian function $G(x,\sigma)$

$$V(x,\sigma,\Gamma) = \int G(x',\sigma)\cdot B(x-x',\Gamma_0)\,dx' \ , \tag{56}$$

with two parameters affecting the width: Γ_0, the intrinsic, natural width of the Breit-Wigner profile, and σ, causing the broadening by experimental resolution effects. This approach is called *Voigt profile* [WBWB74]. To avoid the convolution integral in (56), the *Pseudo Voigt profile* as a superposition of both distributions is usually prefered:

$$V_p(x,\sigma,\Gamma_0) = \eta\cdot B(x,\Gamma_0) + (1-\eta)\cdot G(x,\sigma) \quad . \tag{57}$$

The additional parameter $\eta \in (0,1)$ can be seen as mixing ratio between Gaussian and Breit-Wigner profile. Estimates for η depend on the particular widths of the Breit-Wigner and Gaussian part of (57) and can be calculated approximately [LLH+01]. Other physical constraints can be incorporated in (57) when using Monte-Carlo techniques to sample this distribution. Such a constraint is the exclusion of resonance events with an energy smaller than the proton threshold of ^{4}He. Consequently, all events with an energy smaller than 19.815 MeV need to be rejected for $B(x,\Gamma_0)$. Events propagating to smaller energy values originate only from $G(x,\sigma)$ and are related to resolution effects.

In [MP68], S. Marguiles and J.J. Phelan describe a parametrisation of resonances near particle knock-out threshold with a width Γ_0 by

$$\left(\frac{d\sigma}{d\mu}\right) \propto \frac{(\frac{\mu}{\mu_0})^{l+\frac{1}{2}}}{(\mu-\mu_0)^2 + \left[(\frac{\mu}{\mu_0})^{l+\frac{1}{2}} + r' + r'' + ...\right]^2} \quad . \tag{58}$$

Their formula, adopted from J.D. Jackson [Jac64], bears a certain resemblence to the Breit-Wigner formula (55) but has some remarkable differences:

1) The dependence on the energy is given by the parameter μ, where $\mu = \frac{E-E_{\text{thr}}}{\Gamma_0/2}$, i.e. the energy difference to the threshold energy $E - E_{\text{thr}}$ in units of $\Gamma_0/2$. Additionally $\mu_0 = \frac{E_0-E_{\text{thr}}}{\Gamma_0/2}$ is the energy difference from the resonance's central energy to the energy threshold E_{thr} in units of $\Gamma_0/2$.

2) $r', r'', ..$ are branching ratios for the width of other decay modes Γ^i with respect to the *observed mode* Γ_0, $r^i = \Gamma^i/\Gamma_0$. If only one decay channel is present or strongly dominating, these parameters can be neglected.

3) The cross section vanishes at $\mu = 0$, this means that there are no events related to the resonance at or even before the break-up threshold.[1]

4) l is the partial wave orbital angular momentum of the decay products from the resonance state. For simplicity, we assume $l = 0$.

The formula can be applied to the case of the M0^+-resonance of ^{4}He by substituting its parameters. The continuum begins with the proton knock-out $^4\text{He} + e \rightarrow {}^3\text{H} + \text{p} + e'$ at $E_p = 19.815\,\text{MeV}$, being the first particle knock-out threshold E_{thr}, and the resonance decays by the dominant channel of proton emission. Hence, (58) reduces to the simpler form[2]:

$$\left(\frac{d\sigma}{d\mu}\right) = \frac{1}{\pi}\frac{(\frac{\mu}{\mu_0})^{\frac{1}{2}}}{(\mu-\mu_0)^2 + (\frac{\mu}{\mu_0})} \quad . \tag{59}$$

In Fig. 43a plots for several values μ_0 are shown. The peak varies with the energetic distance from central resonance energy to threshold energy and shows a skewed appearence, in contrast to the symmetric Breit-Wigner form of resonant states.
Another interesting property, when describing the resonance with formula (59), is the shift of the resonance maximum beeing related to the distance between threshold and central resonance energy. In Fig. 43a it becomes evident that μ_0 and the resonance maximum do not coincide, even though for higher μ_0 this effect is reduced. The peak maximum is thus always shifted towards lower

1 For (57) this had to be included additionally.
2 Concerning the normalisation, it can be shown by a complicated integration, that $\int_0^\infty d\mu \left(\frac{d\sigma}{d\mu}\right)_r = \pi$ for $l = 0$ and $r' = r'' = ... = 0$

values, as can be seen by the derivative of (59). The effect of a shifted peak maximum, different from the central value μ_0, takes an extreme value at $\mu_0 = 0.5$. The magnitude of this shift is shown in Fig. 43b. For a central energy value of $E_0 = 20.21\,\text{MeV}$ and a FWHM of $\Gamma_0 \approx 0.24\,\text{MeV}$ of the monopole resonance, this effect is too small to be observed with the given experimental setup.

These two parametrisations, summarised in Tab. 5, are suitable to describe the monopole resonance and can thus be used in Monte-Carlo simulations to analyse the data.

-	Model	No. of free Param.	Eq. refrence
$d\sigma_1$	Gaussian-BW convolution	5(4)	(57)
$d\sigma_2$	Resonance near threshold	3	(59)

Table 5: Summary of the resonance parametrisations. For $d\sigma_1$ the parameters σ and η account for the resolution. Mixing parameter η is constrained by a function depending on σ and Γ_0, thus the number of free parameters is reduced by one (see value in brackets). The experimental resolution in $d\sigma_2$ is included by sampling the momentum resolution with two Gaussian distributions (see Sec. 8.1).

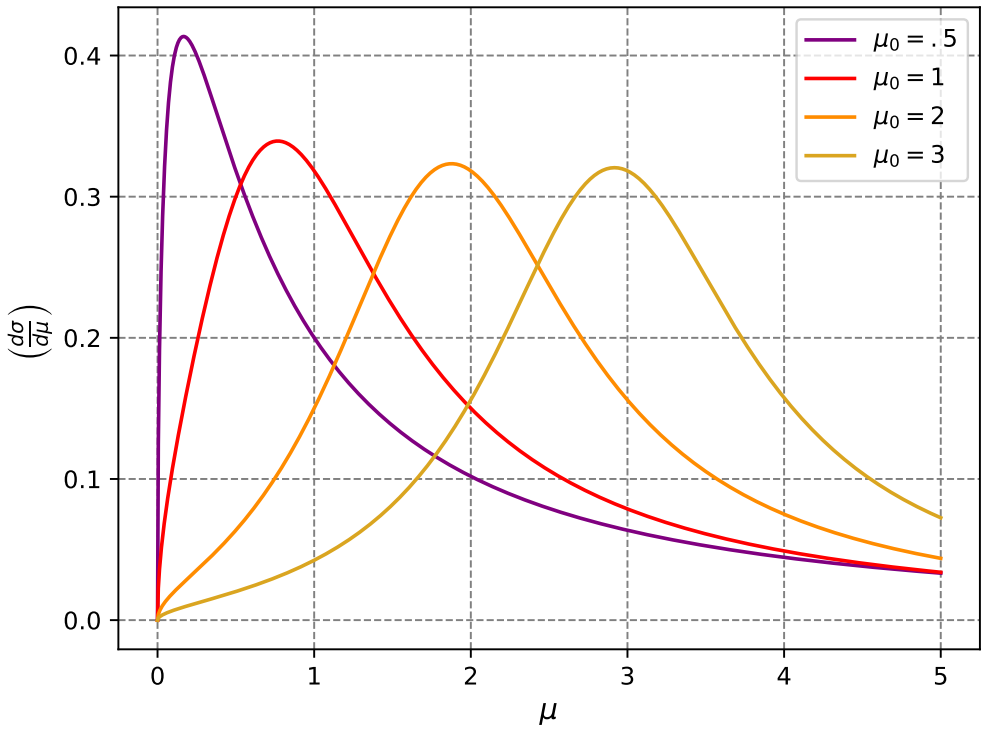

(a)

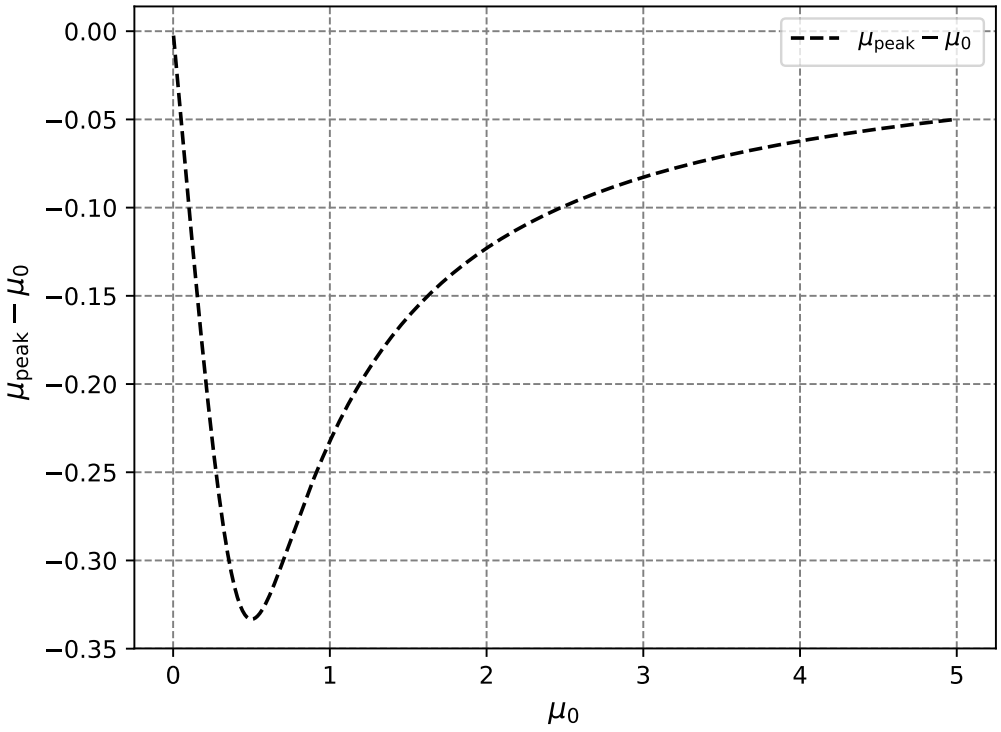

(b)

Figure 43: (a): Cross sections for several values of μ_0 versus parameter μ from (59). (b): Resonance peak shift as a function of parameter μ_0.

7.2 MONTE-CARLO SAMPLING OF RESONANCE PARAMETRISATIONS

Indeterministic effects like emission of photons from a scattered electron or the finite resolution of spectrometers leave Monte-Carlo techniques as a suitable choice to model these processes.
There are several ways to generate random numbers that cover a specific distribution. If the density function of a probability distribution has an analytic integral, i.e. its cumulative distribution function $F(x)$ is analytic,

$$\int_{-\infty}^{x} f(t)\,dt = F(x) = u \in \mathcal{U}(0,1) \tag{60}$$

the method of inverse transform sampling [BL13] can be used. This allows to project a uniformly distributed set of random numbers $\mathcal{U}(0,1)$ to a distribution following the density function $f(t)$. The integral in (60) will always be limited to $(0,1)$, so if $F^{-1}(x)$ exists, the random numbers $x_i = F^{-1}(u_i)$ will follow $f(t)$.

If the integral of $f(t)$ is not analytic or the function $F(x)$ is too complicated to invert, *brute force sampling* is used. With this method two uniformly distributed sets of random numbers $\mathcal{U}_i(0,1)$ and $\mathcal{U}_j(0,1)$ are used to generate a set of random numbers following a distribution density $f(t)$:

1) x_i is transformed in the interval $(a,b) : x_i = a + u_i \cdot (b-a)$, where $|a-b|$ should be large enough to avoid too limited output, but close enough to save computation costs.

2) c is a number chosen with the condition $c \geq \max\{f(x)|x \in (a,b)\}$. The closer c is to the maximum, the more efficient is the algorithm.

3) If $f(x_i) < c \cdot u_j$, x_i is rejected. Otherwise x_i is accepted as random number following $f(t)$.

Brute force sampling has, in comparison to inverse sampling, the disadvantage of requiring considerably more random numbers than finally appear in the output, because more events are rejected. For inverse transform sampling the input-output ratio is equivalent.
Both methods have been used to simulate the resonance parametrisations described in Sec. 7.1. In order to generate $d\sigma_1$ from (57), a Breit-Wigner and a Gaussian distribution[3] are generated with two independent widths Γ_0 and σ and superimposed with the ratio parameter η. The resonance parametrisation $d\sigma_2$ (59) needs to be generated by brute force sampling, because an inversion of $F(x)$ is not feasible. When generating the resonance by simulations, several parameters are required: E_0, the central energy of the resonance, the integral of the resonance and its width Γ_0. The Pseudo Voigt profile requires σ for resolution effects and η as mixing parameter, which can be calculated if Γ_0 and σ are

3 To obtain a sample of Gaussian-distributed random numbers, the Box-Muller algorithm was performed, which requires a slightly different approach of inverse transform sampling

known, see [LLH+01]. Parametrisation $d\sigma_2$ (58) considers the experimental resolution by including an uncertainty in the reconstructed particle momentum given by two Gaussian distributions.
The central energy of the monopole is known to be $E_0 = 20.21\,\text{MeV}$ [TWH92] and can be directly embedded in the simulations. Other parameters, like the resolution of the experimental setup, Γ_0, and the peak integral being directly dependent on the transition form factor, have to be determined. The form factor ratio, determined relative to the elastic peak (Sec. 6.4), is used to obtain the peak integral with already good accuracy. Fig. 44 shows a first set of generated resonance shapes for different Γ_0. The observed width Γ_{obs} is larger due to finite spectrometer resolution and energy loss. The simulated resonance shapes exhibit a long radiative tail caused by the applied radiative corrections (see Sec. 2.4). The determination of the resolution parameters and Γ_0 will be described in the next chapter.

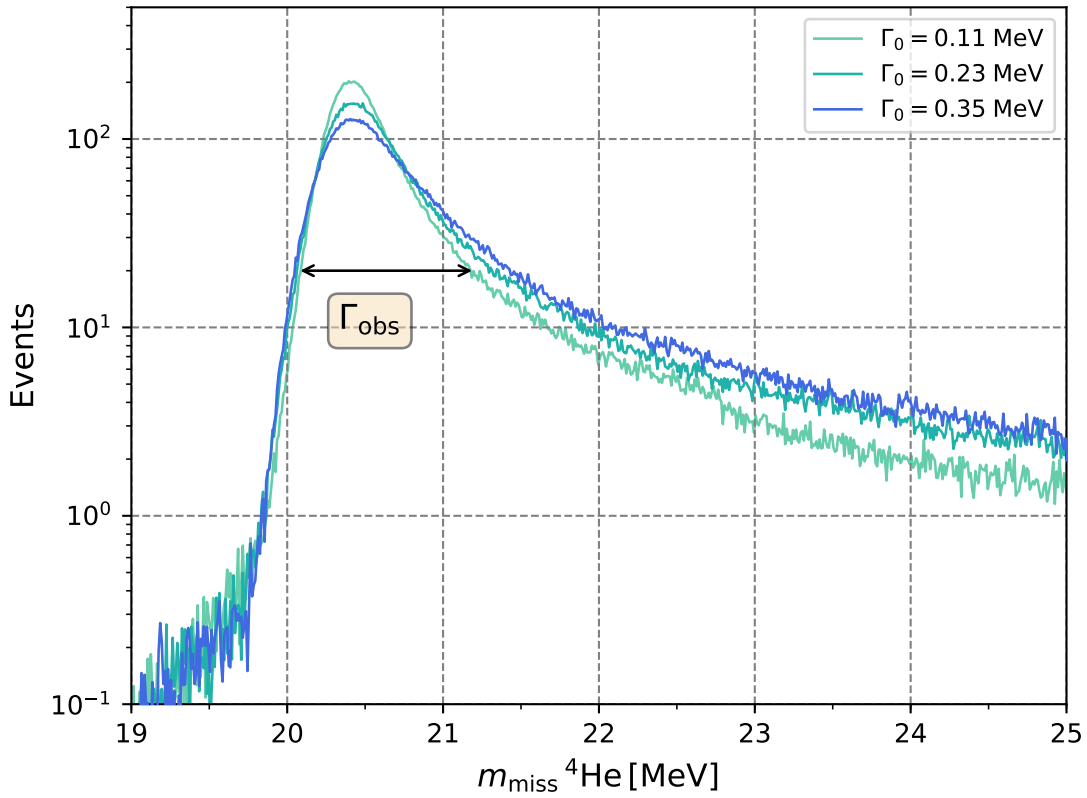

Figure 44: Resonance shapes for various Γ_0 sampled by (59). The tails of the resonances are extended to higher m_{miss} by radiative processes. The observed width of the resonances is broadened by radiative corrections and resolution effects.

8

DETERMINATION OF Γ_0 OF THE ^{4}HE MONOPOLE RESONANCE

8.1 DETERMINATION OF THE EXPERIMENTAL RESOLUTION

Characteristic quantities of the resonance are its central energy E_0, its intrinsic width Γ_0, and its amplitude $\mathcal{A}$, which is directly related to the transition form factor. Γ_0 and $\mathcal{A}$ are not independent from each other and, therefore, it is mandatory to determine Γ_0 as parameter for the simulations before the transition form factor can be extracted precisely.
To obtain Γ_0 the experimental resolution of the measurement apparatus has to be taken into account. As discussed in Sec. 2.4, radiative corrections have to be applied to the cross sections, which lead to a difference between natural and observed resonance shapes. Energy loss of the electrons passing through target and detector material also leads to a broadening of the resonance shape. The observed width Γ_{el} of the elastic peak is a good quantity to determine these effects. Γ_{el} is assumed to be composed of two widths: Γ^2_{exp} accounting for the experimental resolution, and Γ^2_{rad} originating from radiative losses of the electron:

$$\Gamma^2_{el} = \Gamma^2_{exp} + \Gamma^2_{rad} \quad . \tag{61}$$

Both widths are added quadratically to obtain Γ_{el}. A Gaussian fit

$$f_G(x) = \frac{A}{\sqrt{(2\pi\sigma^2)}} \exp(-\frac{(x-\mu)^2}{2\sigma}) \tag{62}$$

applied to a very narrow area around the elastic peak can be used to extract Γ_{el} as shown in Fig. 45a. Accordingly, Γ_{rad} is determined by a simulation of the elastic peak without resolution broadening but with radiative corrections. Parameter σ accounts for experimental resolution effects in the cross section $d\sigma_1$ (see Tab. 5), where $\sigma = \Gamma_{exp}/2\sqrt{2\ln 2}$. In Fig. 45b the results for σ are shown as a function of Q^2_0 for different energies. The values of σ were obtained separately for each beam energy and spectrometer, as shown in Tab. 6.

-	450 MeV	690 MeV	795 MeV
σ spec. A [MeV]	0.319	0.523	-
σ spec. B [MeV]	0.272	0.426	0.557

Table 6: Values for the experimental resolution σ for spectrometers A and B for different energies, applied to $d\sigma_1$.

In parametrisation $d\sigma_2$ (see Tab. 5) resolution effects are modeled with a different approach. Three parameters are used to generate two Gaussian distributions, which simulate a dispersion of the electron momentum. Two of these parameters are associated with the strength of this dispersion leading to a variance in all observables obtained from the electron momentum. The two Gaussian distributions are superimposed with a ratio parameter to allow a more precise emulation of the data. Thus only one parameter is dominating the resolution. These parameters had to be determined additionally for $d\sigma_2$, were scanned in a certain range, and optimised for the best χ^2 between data and simulation. The quantity to determine these parameters is again the ^{4}He elastic peak . The three determined momentum resolution parameters, separate for each energy and spectrometer, are used for simulations of the elastic peak and resonance parametrisation $d\sigma_2$. The obtained values are summarised in Tab. 7.

-	450 MeV	690 MeV	795 MeV
Spec. A	2.03×10^{-4}	2.02×10^{-4}	-
Spec. B	1.76×10^{-4}	1.52×10^{-4}	1.87×10^{-4}

Table 7: Values for the momentum resolution parameters of $d\sigma_2$, contributing most part to the experimental resolution.

In general, the resolution of spectrometer B is better than that for spectrometer A. For the 795 MeV beam energy a different optical matrix was used in spectrometer B, which is appropriate for high central momenta. This can cause the larger variation of the resolution in spectrometer B due to a different "sweet-spot" of each optical matrix used at a certain central momentum. For spectrometer A the same optical matrix was used for all beam energies. Due to the limited maximum central momentum $p_{\text{max.}} = 735\,\text{MeV/c}$ of spectrometer A, it is not possible to measure the elastic peak or the resonance of ^{4}He at the highest beam energy (795 MeV) during this experiment. Data at this energy can only be acquired from spectrometer B.

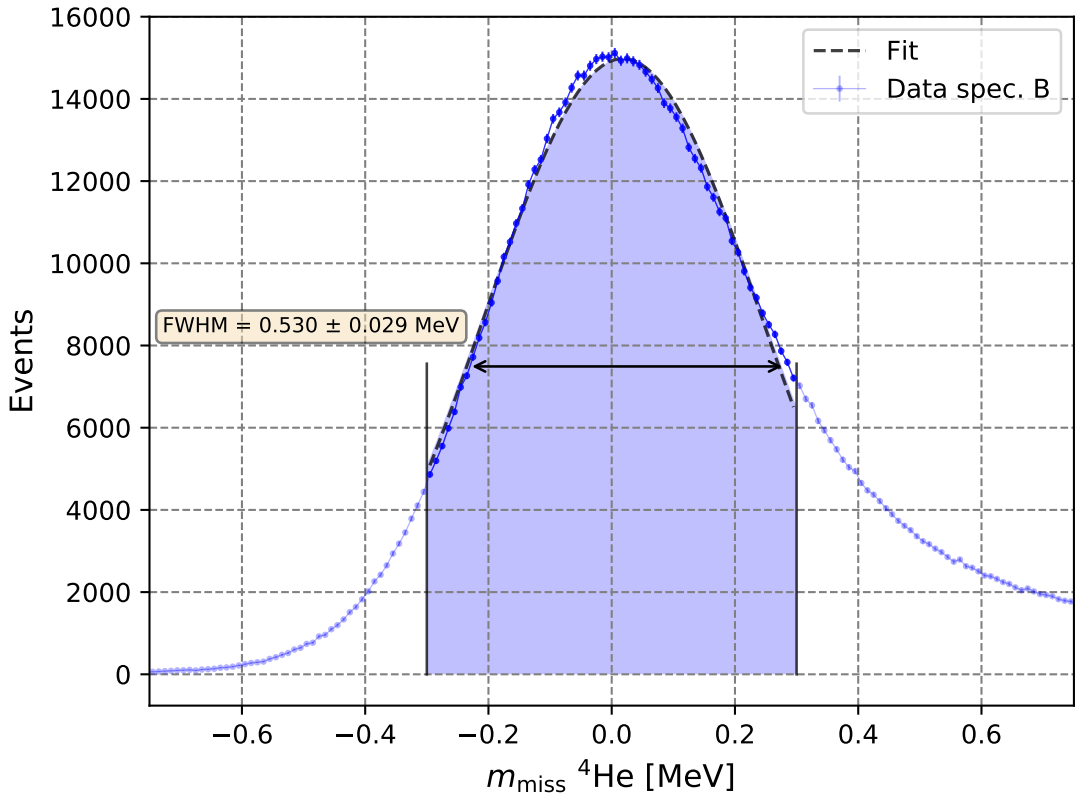

(a)

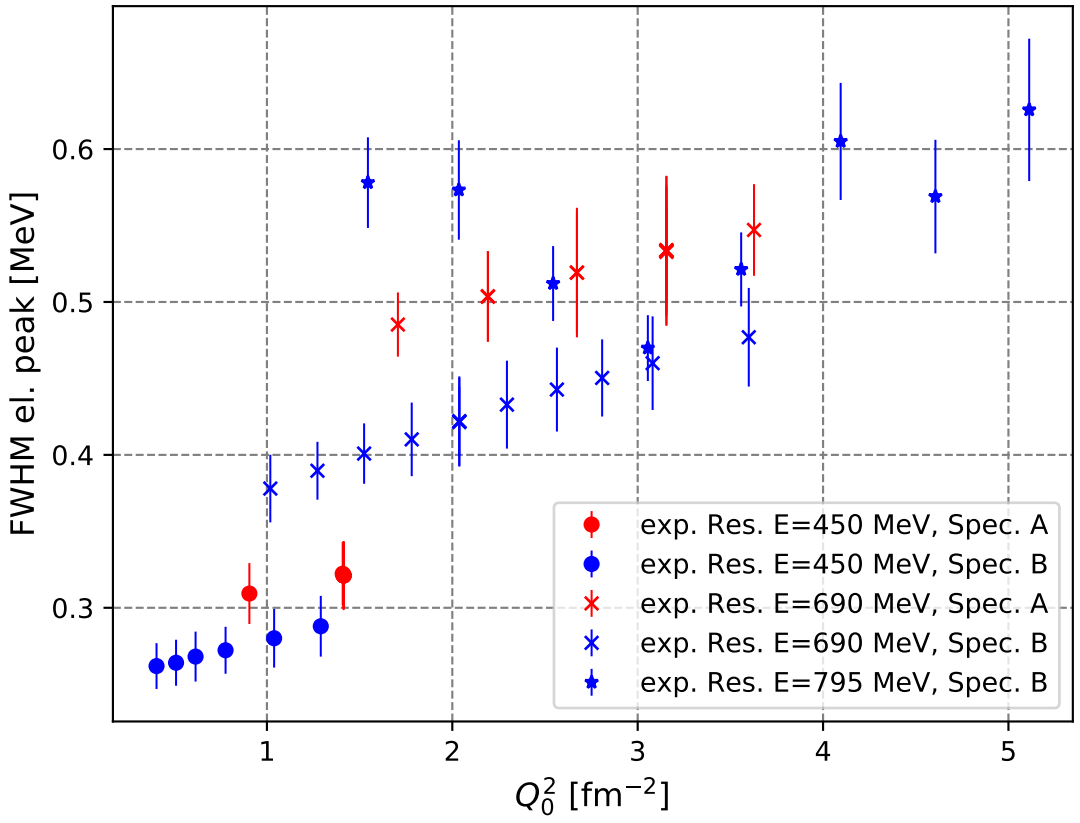

(b)

Figure 45: *(a)*: Gaussian fit to the elastic peak to determine Γ_{el}. The blue-shaded band marks the fit region. *(b)*: Overview of the experimental resolutions for spectrometers A and B determined with (61) at different beam energies.

8.2 OPTIMISATION OF Γ_0

With the resolution parameters determined in the previous section, one can proceed to establish the intrinsic width Γ_0 which plays a crucial role in extracting the transition form factor for each resonance model. The determination of Γ_0 uses backgrounds models 2 & 3 from Sec. 6.3 (see Tab. 4) while background model 1 was only used as benchmark. These two background models are combined with the resonance parametrisations $d\sigma_1$ and $d\sigma_2$ (see Sec. 7.2 and Tab. 5). The procedure to determine Γ_0 is as follows:

1) The data is fitted with background models 2 and 3 from Sec. 6.3 and using the Moyal function (46) to describe the resonance, which then is subtracted to obtain only the background. This background parametrisation is kept constant throughout the whole optimisation procedure.

2) Resonances are simulated for a set of widths $\Gamma_{0,i}$, varying around the anticipated value of the width $\Gamma_0 \approx 240\,\text{keV}$.

3) The simulated resonances are added to the background to obtain a complete model. At this point, the integral of the resonance is not known precisely enough due to the interference with Γ_0, and thus it is one adjusted to the data by a floating factor.

4) The best estimate for Γ_0 is given by χ^2_{min} according to the degrees of freedom.

Only Γ_0 is varied during this optimisation procedure, while the resolution is left constant. The ratio η to regulate the contribution of Gaussian to Breit-Wigner distribution (see (57)) is estimated by an approximation given in [LLH+01]

$$\eta = 1.366 \cdot (\Gamma_0 / \Gamma_{\text{Voigt}}) - 0.477 \cdot (\Gamma_0 / \Gamma_{\text{Voigt}})^2 + 0.111 \cdot (\Gamma_0 / \Gamma_{\text{Voigt}})^3 \tag{63a}$$

$$\begin{aligned}\Gamma_{\text{Voigt}} = (&\Gamma^5_{\text{Gauss}} + 2.693 \cdot \Gamma^4_{\text{Gauss}} \cdot \Gamma_0 + 2.428 \cdot \Gamma^3_{\text{Gauss}} \cdot \Gamma^2_0 \\ &+ 4.472 \cdot \Gamma^2_{\text{Gauss}} \cdot \Gamma^3_0 + 0.0784 \cdot \Gamma_{\text{Gauss}} \cdot \Gamma^4_0 + \Gamma^5_0)^{1/5} \ [\text{MeV}].\end{aligned} \tag{63b}$$

where $\Gamma_{\text{Gauss}} = \Gamma_{\text{exp}}$. When using (63), several difficulties appear: Γ_0 is actually the width to be determined, but as a prior estimate, Γ_0 is required in (63a) and (63b). For this estimate, the width $\Gamma_0 = 240\,\text{keV}$ from Koebschall et al. [KOM+83] was used in (63a) yielding $\eta = 0.53$. However, η does not vary strongly in the range close to χ^2_{min} and thus can be left constant throughout the whole optimisation procedure.
For resonance parametrisation $d\sigma_2$ (see Tab. 5), only Γ_0 needs to be optimised with regard to the momentum resolutions from Tab. 7.

In Fig. 46 and Fig. 47 the process to determine Γ_0 is shown using resonance parametrisation $d\sigma_2$ and background model 3. Simulated monopole resonances are generated with parameters $\Gamma_{0,i} \in \{50\,\text{keV}, 110\,\text{keV}, 170\,\text{keV}, 230\,\text{keV}, 290\,\text{keV}, 350\,\text{keV}\}$ (see Fig. 44). Background and simulated resonance are added and the χ^2 between data and model is determined by

$$\chi^2 = \sum_i \frac{(n_i - s_i)^2}{n_i} = \sum_i \frac{\Delta_i^2}{n_i} \tag{64}$$

where n_i,s_i is the number of events in bin i for data and simulation, respectively. In Fig. 46 this is illustrated for a resonance simulated with $\Gamma_0 = 110\,\text{keV}$. The second axis on the right shows the contribution Δ_i^2 / n_i of each bin to the χ^2 sum. In case of Fig. 46, the sum is large due to the value for Γ_0 (110 keV) which is (presumably) too small. All values of χ^2 corresponding to the $\Gamma_{0,i}$ are then fitted with a polynomial of 2$^{\text{nd}}$ order (see Fig. 47a), exhibiting a minimum for the best estimate of Γ_0. This value of Γ_0 is accordingly used to simulate the resonance again (see Fig. 47b). After the optimisation procedure, model and data show good agreement.

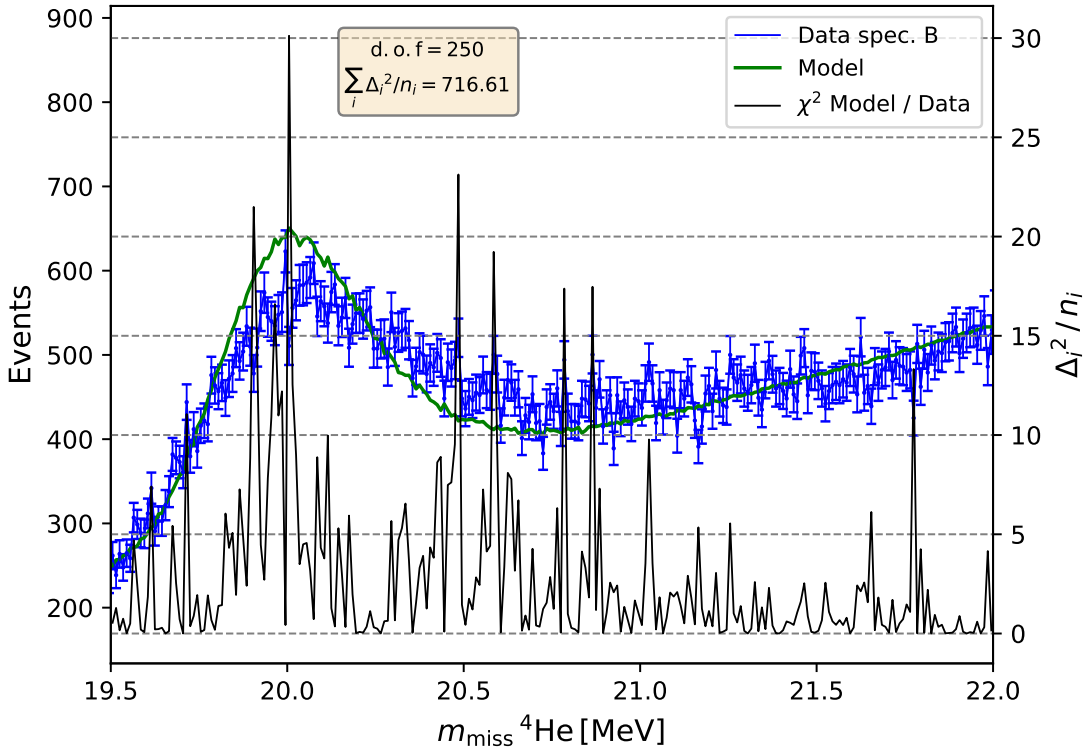

Figure 46: Evaluation of χ^2 for $\Gamma_{0,i} = 110\,\text{keV}$ with Δ_i^2 / n_i on the right axis. For the case shown, the agreement with the data is inadequate.

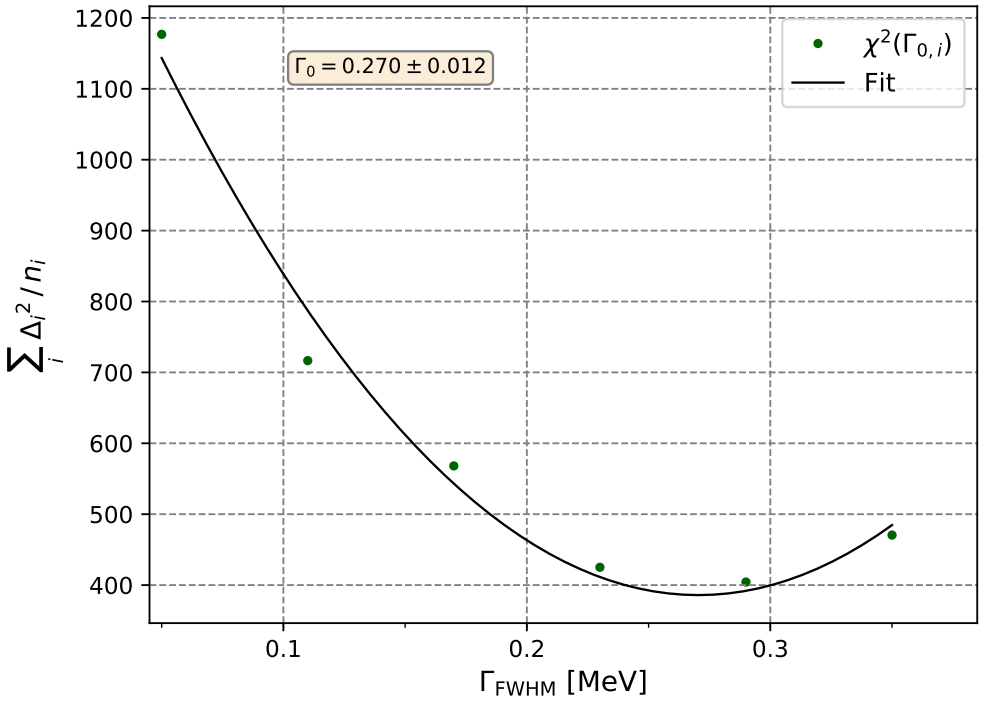

(a)

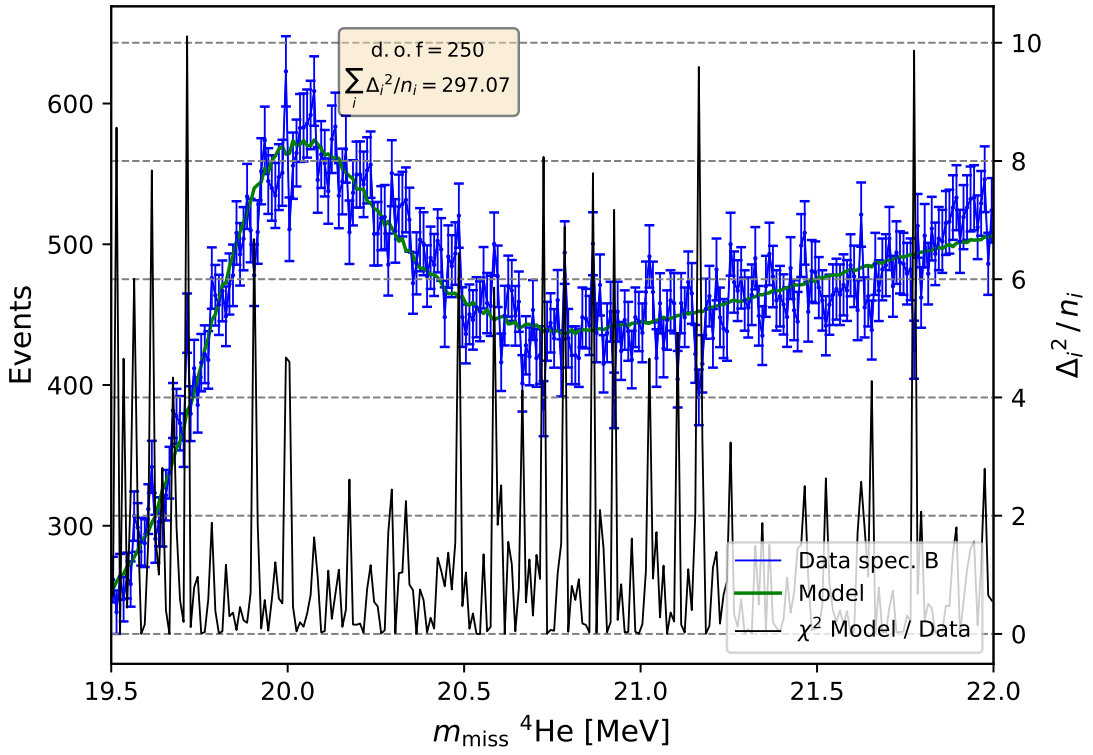

(b)

Figure 47: *(a)*: Fit to determine the optimal Γ_0 according to the minimmal χ^2 (b): Data and simulation in comparison for the optimal Γ_0, Δ_i^2 / n_i on right axis.

8.3 FINAL RESULTS OF Γ_0 AND COMPARISON TO FORMER RESULTS

To obtain Γ_0, the procedure outlined in Sec. 8.2 is applied for backgrounds of type 2 and 3 in combination with the two resonance parametrisations $d\sigma_1$ and $d\sigma_2$ for each setup and spectrometer. The values of Γ_0 are determined in the m_{miss}-range between 19.5 MeV and 22 MeV. The lower limit of this cut is chosen close to the proton knock-out threshold energy ($E_p = 19.815$ MeV), while the upper limit covers more than 99.5% of the relative integral (see Fig. 48).

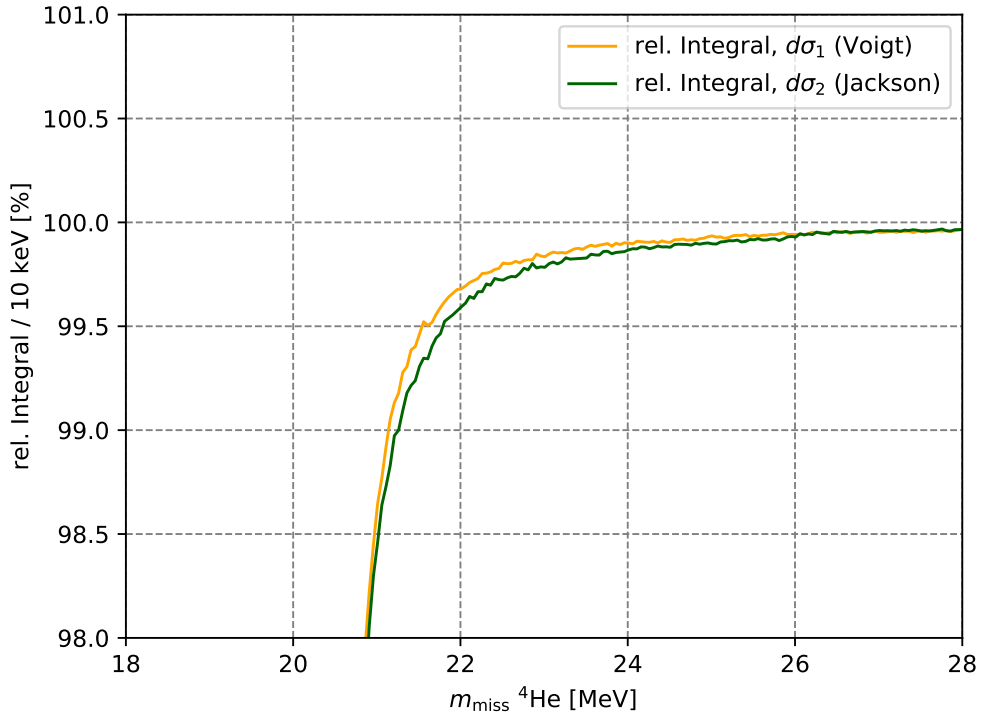

Figure 48: The relative integral of the two resonance peaks for $\Gamma_0 = 240$ keV. A cut in m_{miss} on the right tail of the peaks at 22 MeV is sufficient to cover more than 99.5% of the events of resonance model 1 (57) and model 2 (58).

The results for Γ_0 for different values of the central Q_0^2 are shown in Fig. 49a and Fig. 49b for $d\sigma_2$ in combination with backgrounds BG2 and BG3 (see Tab. 4), respectively. Statistical and systematic errors were added quadratically. Existing data for Γ_0 from [FRC+68, Wal70, KOM+83] are indicated in the plots by dashed lines, while the green solid lines show the results of this experiment. All values of Γ_0 (including the values from $d\sigma_1$ not shown here) can be found in the data tables of App. E. The final values for Γ_0 are summarised in Tab. 8, averaged for all setups, to obtain a final value for Γ_0, with the standard deviation as error.
The values show good agreement amongst each other within the experimental and statistical uncertainty. As can be infered by the obtained values, the (linear) background model BG2 leads to smaller values for Γ_0 compared to BG3, which uses a broad Gaussian tail (51).

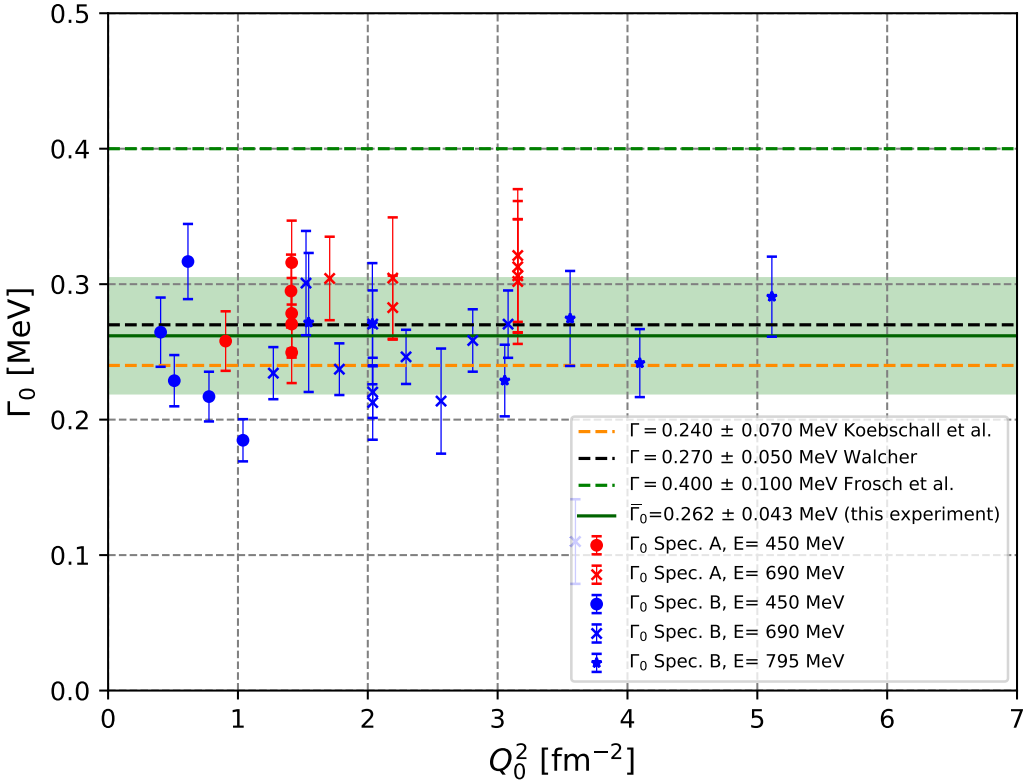

(a)

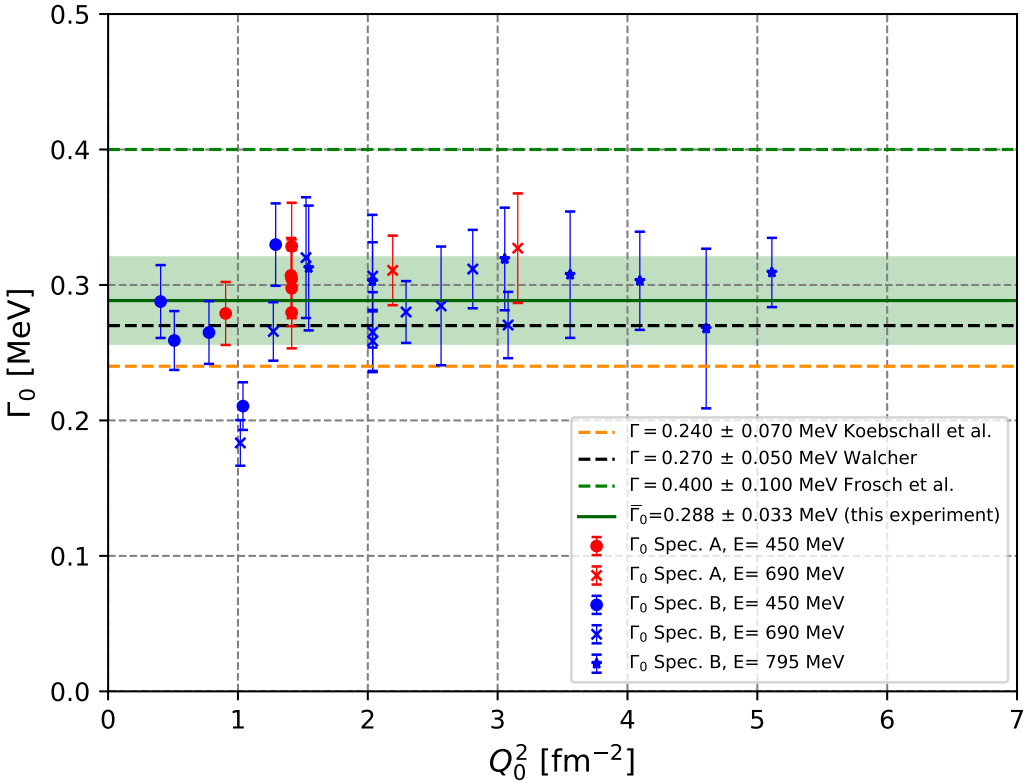

(b)

Figure 49: Γ_0 for resonance parametrisation $d\sigma_2$ and background model BG2 *(a)*, and BG3 *(b)*. The standard deviation of all points is indicated by the green-shaded area.

-	BG2	BG3
$d\sigma_1$	268 ± 43 keV	285 ± 33 keV
$d\sigma_2$	262 ± 47 keV	288 ± 39 keV

Table 8: Determined values for the intrinsic FWHM Γ_0 in keV for different background models and resonance parametrisations.

The obtained Γ_0 agree with the values from Walcher [Wal70] and Köbschall et al. [KOM+83]. The extracted Γ_0 with error bars according to the used background and resonance model are shown in Fig. 50 with the existing values from [FRC+68, Wal70, KOM+83].

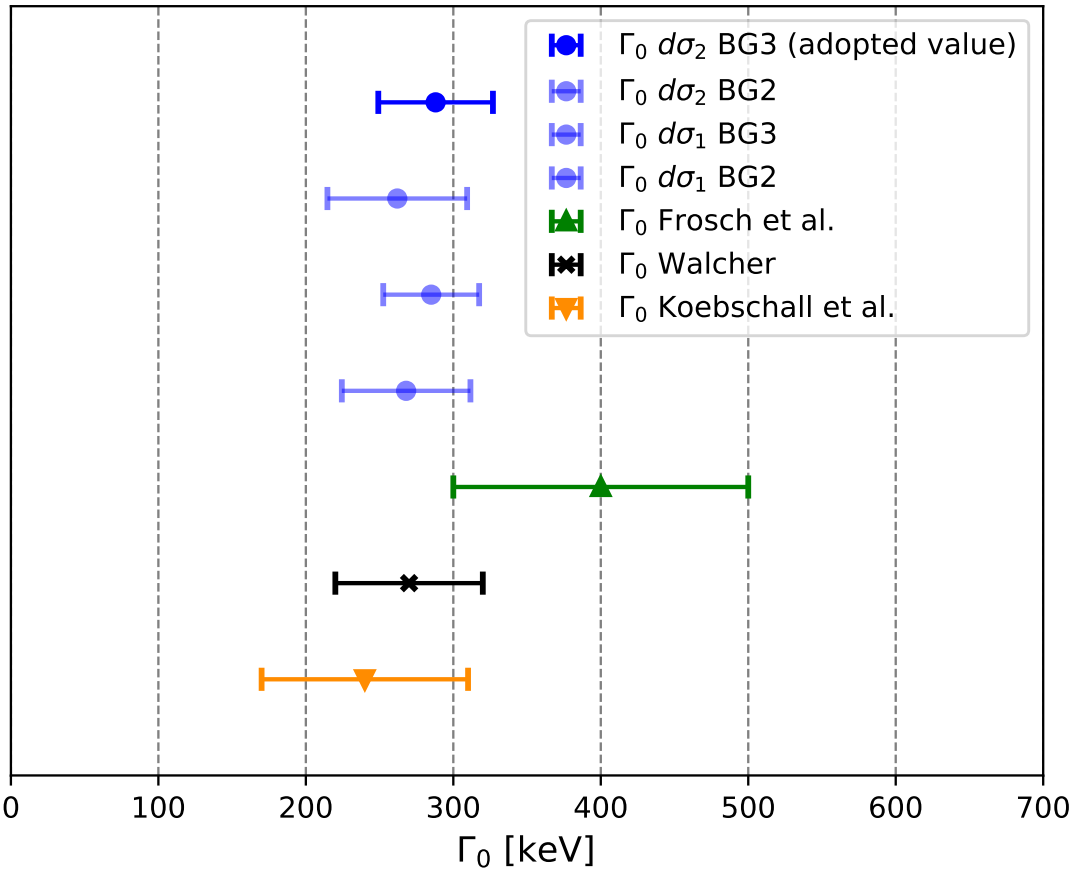

Figure 50: Γ_0 from this experiment with existing data from referenced authors [FRC+68, KOM+83, Wal70]. The model combination of $d\sigma_2$ with background BG3 will be the adopted choice for the further analysis. The error bars show systematical and statistical uncertainties.

An important point that must be emphasized when comparing the values of Γ_0 is the difference between the used parametrisations $d\sigma_1$ and $d\sigma_2$ of the monopole resonance (see Tab. 5). Parametrisation $d\sigma_2$ from (59) is skewed in its intrinsic form before the application of radiative corrections as shown in Sec. 7.1. The authors [FRC+68, Wal70, KOM+83] used the symmetric Breit-Wigner shape to describe the resonance obtained from the asymmetric line-

shape in the spectra by applying unfolding procedures. The plot in Fig. 51 shows parametrisation $d\sigma_2$ without the application of radiative corrections to emphasize its non-symmetric form. This begs the question if a comparison to Γ_0 obtained with parametrisation $d\sigma_2$ to the values from the symmetric form $d\sigma_1$, a superimposed Breit-Wigner and Gaussian distribution, is appropriate. However, the agreement amongst the existing values and the values extracted in this experiment is still remarkable.

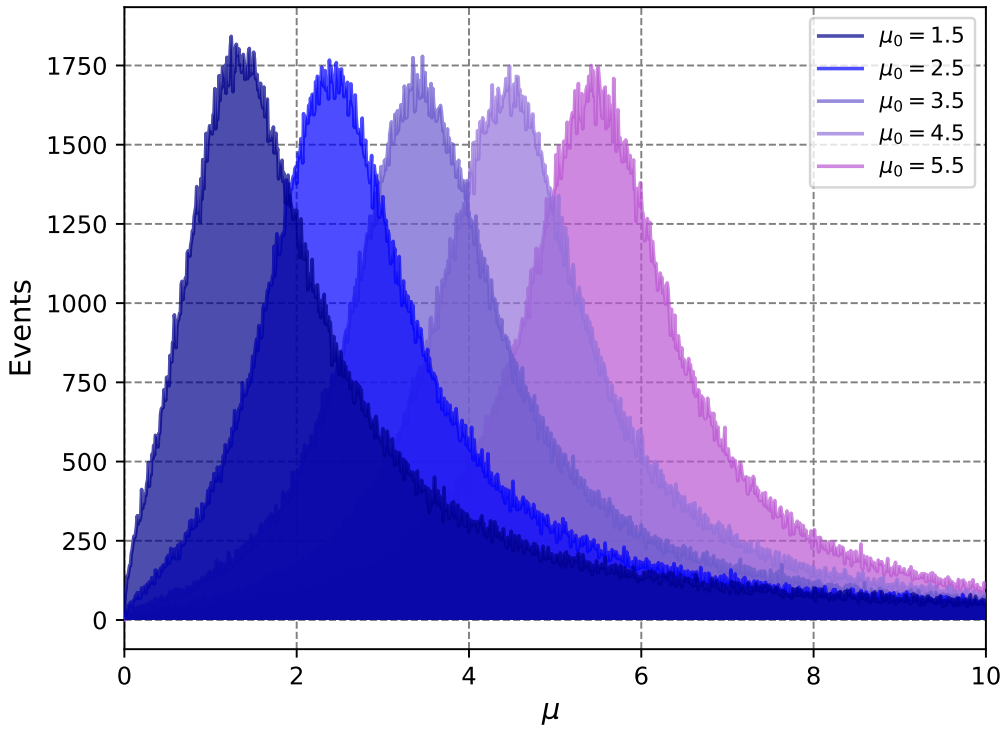

Figure 51: *(a)*: Monte-Carlo sampled histograms from (59) without radiative corrections, exhibiting the skewed nature of this parametrisation.

The resonance parametrisation $d\sigma_2$ (see (59) in Sec. 7.1) has been used in the further analysis. The reason for this choice is, that typical resonance properties are inherently embedded in this model. This resonance model is combined with background model BG3, (51), a broad Gaussian tail vanishing at the proton threshold ($E_{\text{thr}} = 19.815\,\text{MeV}$). The ^{4}He continuum shows several other resonances, partly with broad width, making this background model the most reasonable option. All remaining combinations of background and resonance models are analysed in parallel and serve as a benchmark to test model dependencies.
Angular and momentum resolution of the spectrometers are the major sources of systematic uncertainties in the determination of Γ_0. The momentum and angular resolution of the spectrometers enter into all optimisation steps of Γ_0 and influence the results. This was estimated by varying angular resolution (3 msr) and momentum resolution (see Tab. 6 and Tab. 7) in a range of 25 %.

Repeating the determination of Γ_0 with this variation leads to an uncertainty of $\pm 2.0\%$ due to the angular resolution and $\pm 7.0\%$ due to the momentum resolution in Γ_0. These values of the systematic errors are added to the statistical error.

9

DETERMINATION OF THE MONOPOLE TRANSITION FORM FACTOR $|\mathcal{F}_{M0^+}(Q_0^2)|^2$

9.1 OPTIMISATION OF $|\mathcal{F}_{M0^+}(Q_0^2)|^2$

With the obtained Γ_0 from Chap. 8 the error on the determination of the transition form factor $|\mathcal{F}_{M0^+}(Q_0^2)|^2$ can be reduced. This is done by minimising the χ^2 between simulated resonance with background model and data by keeping Γ_0 fixed. Here the background is fitted with one of the described models BG2 or BG3 (see Tab. 4), while the simulation $s(m_{\text{miss}})$ is varied with a floating factor a, thus yielding an overall model function

$$f_{\text{tot}}(m_{\text{miss}}, (a, \vec{p}_{\text{bg}})) = a \cdot s(m_{\text{miss}}) + f_{\text{bg}}(m_{\text{miss}}, \vec{p}_{\text{bg}}) \tag{65}$$

with background model $f_{\text{bg}}(m_{\text{miss}}, (\vec{p}_{\text{bg}}))$ depending on a set of parameters $\vec{p}_{\text{bg}}$. For the optimal set of parameters the χ^2 of this model function is minimised:

$$\chi^2 = \sum_i \frac{(n_i - f_{\text{tot}}(x_i, (a, \vec{p}_{\text{bg}})))^2}{n_i} \quad , \tag{66}$$

where n_i is the number of data events in bin i. Parameter a is a factor multiplied to every bin of the simulation and thus the quantity to regulate the integral of the simulated resonance $s(m_{\text{miss}})$ and to adjust the transition form factor:

$$|\mathcal{F}_{M0^+}({Q_0}^2)|^2 = \left(|\mathcal{F}_{\text{ratio}}(Q_0^2)|^2 \cdot |\mathcal{F}_{\text{g.s.}}(Q_0^2)|^2\right) \cdot a \tag{67}$$

determined in Sec. 6.4. Applying this procedure in an extended m_{miss}-range from 19.5 MeV to 22 MeV now allows to include more contributions of the resonance's radiative tail.
In Fig. 52 the results of such an exemplary optimisation procedure are illustrated for background models BG2 and BG3, and resonance parametrisation $d\sigma_2$. The extension of the radiative tail propagates into the continuum and is now taken into account when matching model to data. These events in the radiative tail contribute significantly, resulting in $a > 1$ and increase the value of the transition form factor $|\mathcal{F}_{M0^+}({Q_0}^2)|^2$.

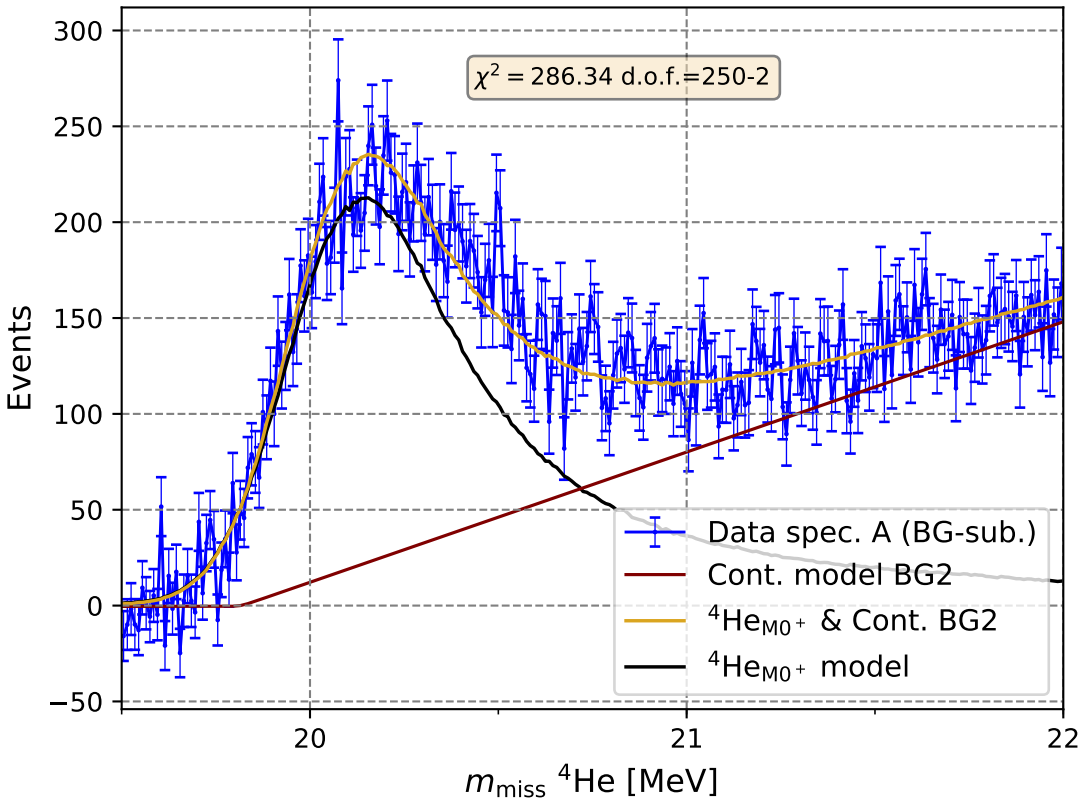

(a)

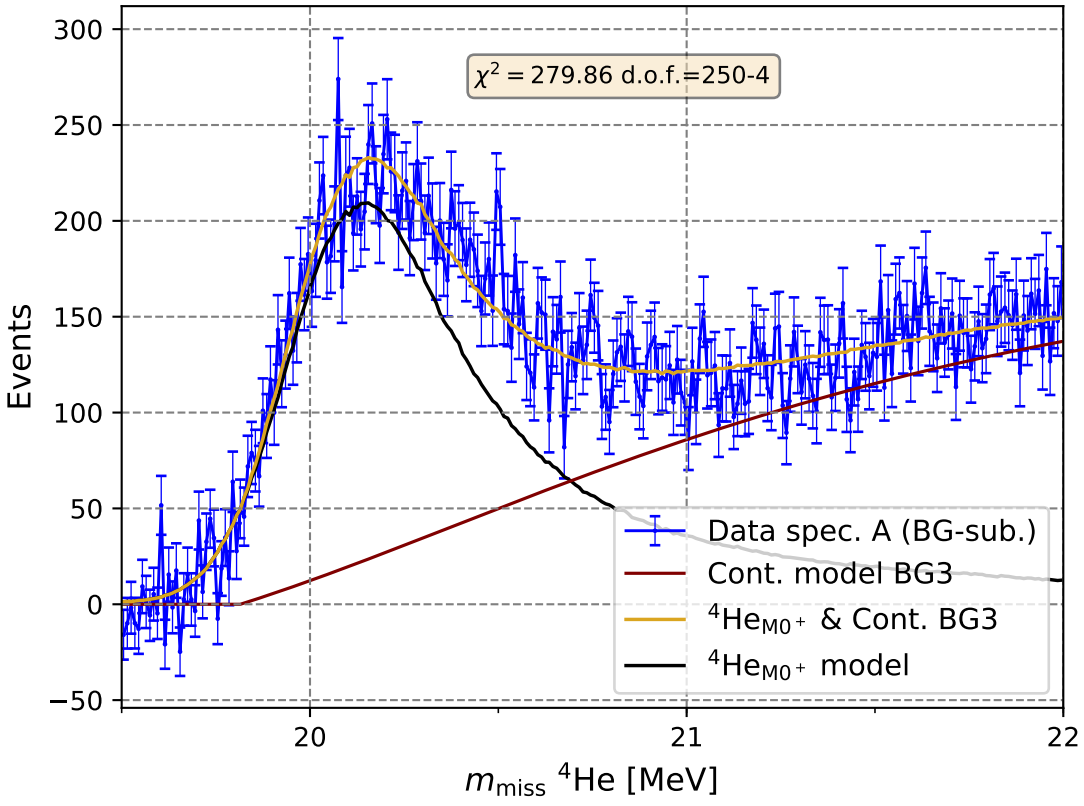

(b)

Figure 52: Adjustement of model to data (w. stat. error) for background model BG2 *(a)* and background model BG3 *(b)*. Radiative corrections in the simulation of the monopole resonance (black) lead to a long radiative tail.

9.2 RESULTS OF $|\mathcal{F}_{M0^+}(Q_0^2)|^2$

In Fig. 53 the results for the transition form factor $|\mathcal{F}_{M0^+}(Q_0^2)|^2$ obtained with resonance model $d\sigma_2$ and background model BG3 are shown with two fit models.
The first model uses basis-splines $b_i(Q_0^2)$, forming a set of third-order polynomials constructed on knots $k_i \in \{0, 0.5, 1.5, 2.5, 7\}$ supplemented by two boundary conditions:

$$B(Q_0^2 = 0\ \text{fm}^{-2}) = 0, \tag{68a}$$
$$B'(Q_0^2 = 7\ \text{fm}^{-2}) = 0. \tag{68b}$$

The boundary condition in (68a) originates from the condition that there is no excitation possible at $Q_0^2 \equiv 0$. With (68b), the fit is directed to converge to zero for high Q_0^2. The second model is a $\mathcal{O}(2)$-polynomial without constant term multiplied with an exponential function:

$$f_{\text{exp}}(Q_0^2) = \left(a_1 \cdot Q_0^2 + a_2 \cdot (Q_0^2)^2\right) \cdot \exp(-\alpha \cdot Q_0^2). \tag{69}$$

A detailed determination of the basis-spline parameters with error band and the parameters of the second model can be found in App. C.

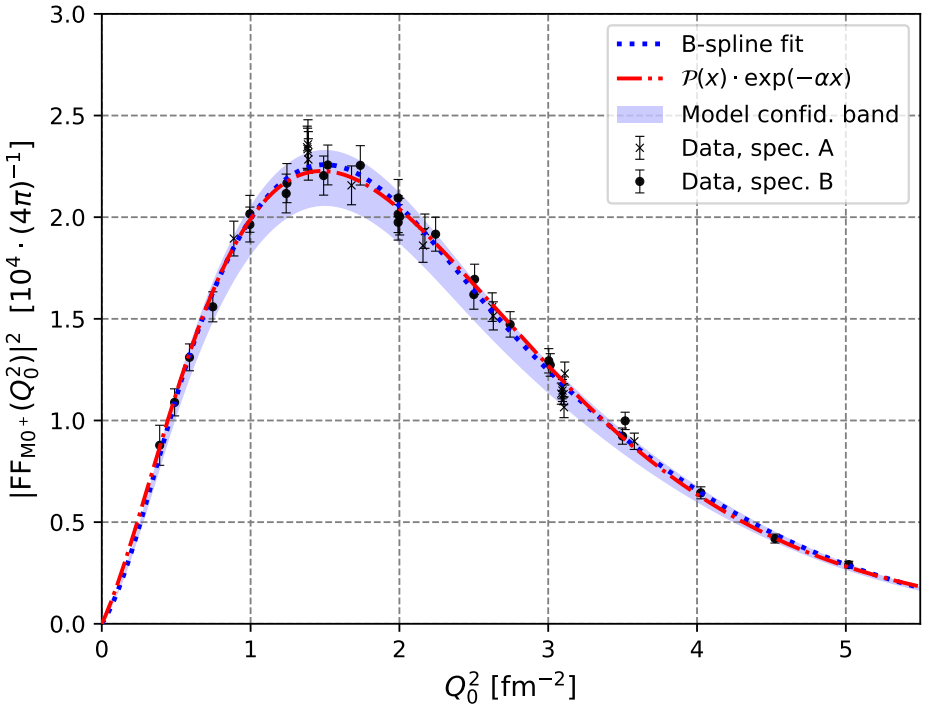

Figure 53: Best fit to the data of $|\mathcal{F}_{M0^+}(Q_0^2)|^2$ with basis splines and conditions (68), and (69). The blue band represents model uncertainties.

Systematic errors of the transition form factor are the uncertainty of the elastic form factor of the ^{4}He ground state, the background subtraction described in Sec. 6.2 and the FWHM Γ_0.
The elastic form factor of ^{4}He is a well measured quantity. The parametrisation of Ottermann et al. [OKM+85] is used in simulations of the ^{4}He ground state and form factor ratio (see Sec. 6.4). The error of the ^{4}He elastic form factor in the Q^2-range in which this data was taken can be estimated to 0.5%, as given by the authors in [OKM+85]. Another systematical uncertainty is caused by the background subtraction of the ^{4}He tail and the target cell contributions. This background is subtracted with a fit to combined simulations that include typical processes of electron scattering on ^{4}He and the target cell material ^{27}Al (see Sec. 6.2). A clear validation of these simulations in the region of $m_{\text{miss}} > 19.5\,\text{MeV}$ is not possible. Here the monopole begins to overlap with the ^{4}He tail and the cell background contributions, not allowing for a clear distinction. Thus, the systematic uncertainty can only be estimated with the uncertainty of the background fit to 1.0%. The error propagation of Γ_0 on the transition form factor was investigated by repeating the analysis with values of Γ_0 ranging from the upper to the lower limit of the uncertainty of Γ_0 (see Chap. 8). With the obtained differences on the result of $|\mathcal{F}_{\text{M0}^+}(Q_0^2)|^2$, the uncertainty due to Γ_0 could be estimated to 4.0%. All errors shown in the plots take into account statistical and systematic errors. When analysing the data with the two available models for background BG2 and BG3 and the two resonance models $d\sigma_1$ and $d\sigma_2$, it is possible to establish model uncertainties of the transition form factor and provide a model confidence band. The relative deviation of the transition form factor, analysed by different models, is used as quantity to estimate these dependencies. This is achieved by comparing the result for $|\mathcal{F}_{\text{M0}^+}(Q_0^2)|^2$ with either the background parametrisation (and leaving the resonance model fixed to $d\sigma_2$) or the resonance model (and leaving the background model fixed to BG3). Fig. 54 shows the results of these comparisons for each setup and spectrometer with their average value $\Delta_{\text{bg/res. mod.}}$ and the standard deviation $\sigma_{\text{bg/res. od.}}$ around the average.
As shown in Fig. 54a, using either BG2 or BG3 for the background leads only to slight fluctuations on $|\mathcal{F}_{\text{M0}^+}(Q_0^2)|^2$ with the largest deviation observed at low and high Q_0^2. In these kinematic, the transition form factor is strongly suppressed compared to the background, making these setups more sensitive to variations caused by a different background parametrisation. The other deviations are compatible with 0% with an average deviation estimated to $\Delta_{\text{bg.}} = 0.5\%$. A strong influence on the transition form factor by using different background models is thus restricted to low and high Q_0^2. To consider the background model dependency in the model confidence band, the standard deviation $\sigma_{\text{bg}} = \pm 3.2\%$ is included in the model confidence band.
However, the use of a different resonance parametrisation leads to a shift in the transition form factor (see Fig. 54b). Resonance model $d\sigma_2$ leads to larger values of $|\mathcal{F}_{\text{M0}^+}(Q_0^2)|^2$ by an average estimate of $\Delta_{\text{res.mod.}} = 5.8\%$ with a standard de-

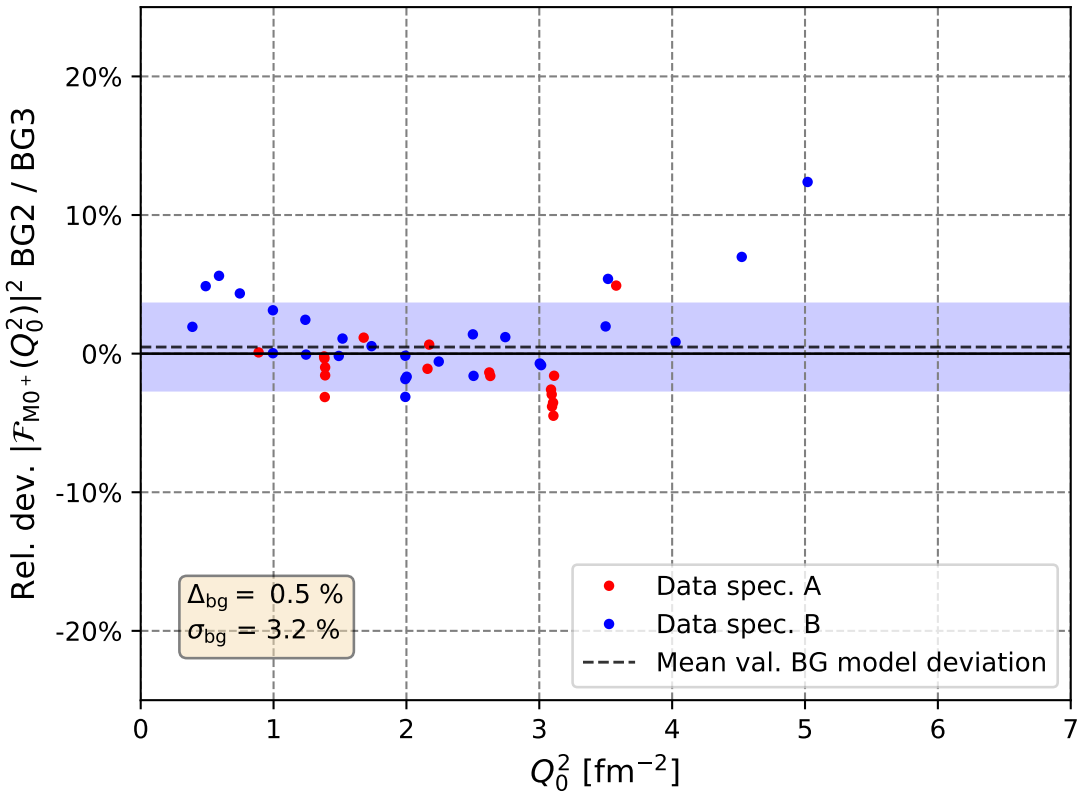

(a)

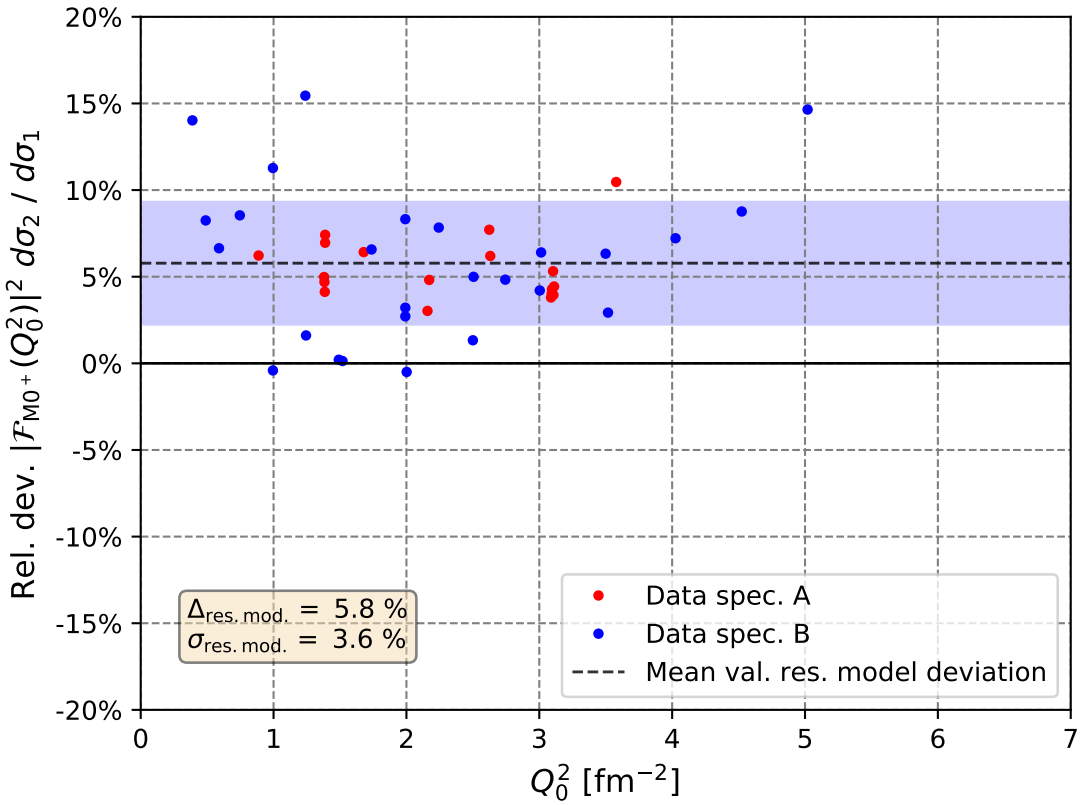

(b)

Figure 54: Relative deviation between the two models for background BG2 and BG3 *(a)* and resonances $d\sigma_1$ and $d\sigma_2$ *(b)* on the transition form factor. The blue band indicates the standard deviations $\sigma_{bg/res.\,mod.}$ between the values, while the mean values $\Delta_{bg/res.\,mod.}$ are shown by the dashed black lines.

viation $\sigma_{\text{res. mod.}} = \pm 3.6\%$. This leads to the assumption that the resonance parametrisation $d\sigma_2$ from (59) tends to yield higher values of $|\mathcal{F}_{M0^+}(Q_0^2)|^2$ than $d\sigma_1$. The setups with a statistically suppressed monopole again exhibit the largest fluctuations if different resonance models are applied.
These two model dependencies are added linearly to a model confidence band of the data extending from -9% to $+3.2\%$ around the best fit. In Fig. 55 the data for the transition form factor is shown together with theoretical calculations and previous measurements.

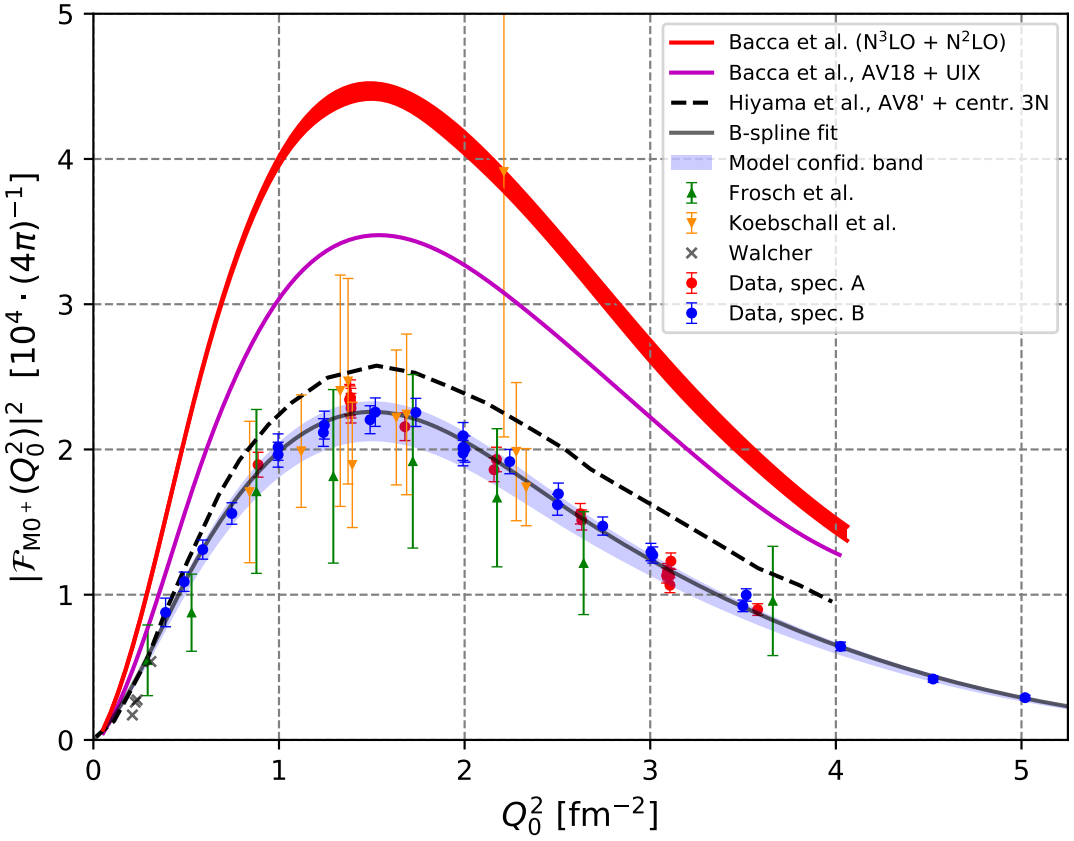

Figure 55: Comparison of $|\mathcal{F}_{M0^+}(Q_0^2)|^2$ with previous measurements ([FRC+68], [KOM+83], [Wal70]) and theoretical predictions from [BBLO13] and [HGK04].

Existing data of the transition form factor $|\mathcal{F}_{M0^+}(Q_0^2)|^2$ are provided by Frosch et al. [FRC+68], Koebschall et al. [KOM+83] and Th. Walcher [Wal70].
The results of our experiment are in good agreement with existing data and reduce the previous systematic uncertainties on the transition form factor significantly. By covering the complete Q_0^2-range of interest, it is possible to compare the different existing calculations to our results of $|\mathcal{F}_{M0^+}(Q_0^2)|^2$ systematically. The theoretical predicitions of Hiyama et al. [HGK04], using an Argonne AV8' two-body force in combination with a phenomenological three-body-force potential, show the smallest deviation to our data. The data at low Q_0^2 can be reproduced by this calculation, but a significant deviation of more than 20% is observed at $Q_0^2 \gtrsim 1.0\,\text{fm}^{-2}$.

For calculations with Argonne AV18 and Urbana-Illinois UIX potentials the deviation increases to more than 60%, observed at the maximum of the transition form factor. This finding leads to the conclusion that established potentials of phenomenological forces, which exhibit good agreement for various topics of nuclear structure, fail to describe the ^{4}He monopole. The ab-initio calculations based on χEFT potentials by Bacca et al. [BBLO13] show a deviation from the data of this experiment up to a factor 2. On the contrary, the same potentials reproduce the elastic form factor of the ^{4}He ground state within a few percent. At the time of writing, this discrepancy is unresolved and raises questions about the strength of terms so far not included in the χ-expansion of these potentials.

9.4 MONOPOLE MATRIX ELEMENT AND TRANSITION RADIUS

Theoretical calculations on the ^{4}He monopole do not only differ in the outcome of the transition form factor, but also about its spatial structure. The ongoing discussion distinguishes between either considering the monopole as a *breathing mode* [BBLO15] or as a loosely bound $3N + N$ system [HGK04].
With the transition form factor data at low Q_0^2 it is possible to determine the monopole matrix element ME and the transition radius $\mathcal{R}_{\mathrm{tr}}$ of the monopole resonance as terms of a low-Q_0^2 expansion. These terms provide information about the spatial structure and, in particular, about the spatial extension of the ^{4}He monopole by the transition radius $\mathcal{R}_{\mathrm{tr}}$. The monopole matrix element ME is defined as

$$\mathrm{ME} = \langle r^2 \rangle_{\mathrm{tr}} = 4\pi \int \rho_{\mathrm{tr}}(r) r^4 dr \ , \tag{70}$$

and the transition radius $\mathcal{R}_{\mathrm{tr}}$ reads as

$$\mathcal{R}_{\mathrm{tr}} = \frac{\langle r^4 \rangle_{\mathrm{tr}}}{\langle r^2 \rangle_{\mathrm{tr}}} \ . \tag{71}$$

Both observables can be obtained by a fit [Che08] to the transition form factor data at a low-Q_0^2. This low-momentum transfer analysis is model independent and it can be compared to the systematics of monopole transitions in light nuclei [The72]. At low momentum transfer the spherical Bessel function in

$$|\mathcal{F}_{\mathrm{M0^+}}(q)|^2 = \left[\frac{1}{Z} \langle \Psi_{\mathrm{M0^+}} | \int \rho(r) j_0(qr) d^3r | \Psi_0 \rangle \right]^2 \tag{72}$$

can be represented as a series expansion in the four-momentum. Accounting for orthogonality of initial and final state wave functions, one gets

$$\begin{aligned} \frac{\sqrt{4\pi \mathrm{B}(\mathrm{M0}, Q_0)}}{Q_0^2} = \frac{\mathrm{ME}}{6} \Bigg[1 - \frac{Q_0^2}{20} \mathcal{R}_{\mathrm{tr}}^2 + \frac{(Q_0^2)^2}{840} \frac{\langle r^6 \rangle_{\mathrm{tr}}}{\langle r^2 \rangle_{\mathrm{tr}}} - \\ \frac{(Q_0^2)^3}{60480} \frac{\langle r^8 \rangle_{\mathrm{tr}}}{\langle r^2 \rangle_{\mathrm{tr}}} + \mathcal{O}((Q_0^2)^4) \Bigg] \ , \end{aligned} \tag{73}$$

where $4\pi\,\mathrm{B(M0}, Q_0) = Z^2|\mathcal{F}_{\mathrm{M0^+}}(Q_0^2)|^2$ is the reduced transition probability of monopole transitions. If the data is limited to low Q_0^2, it is common to truncate (73) to orders of $\mathcal{O}((Q_0^2)^2)$ while terms of $\mathcal{O}((Q_0^2)^3)$ or higher are neglected. In order to supplement the data of this experiment, the data from Walcher [Wal70] at lower Q_0^2 are integrated into the fits of (73) to determine ME and $\mathcal{R}_{\mathrm{tr}}$. To estimate variations of the results, the fits are repeated with only the data of this experiment and with a different range of Q_0^2 extending from $0\,\mathrm{fm}^{-2}$ to either $1.0\,\mathrm{fm}^{-2}$ or $1.5\,\mathrm{fm}^{-2}$. Theoretical values for ME and $\mathcal{R}_{\mathrm{tr}}$ are also obtained by fitting (73) to the predictions of Hiyama et al. [HGK04] and Bacca et al. [BBLO15]. The plots are shown in Fig. 57 and the obtained values are presented in Tab. 9.

		ME [fm^2]	$\mathcal{R}_{\mathrm{tr}}$ [fm]
Bacca et al. (1)	($Q_0^2 < 1.1\,\mathrm{fm}^{-2}$)	1.799 ± 0.002	3.869 ± 0.010
Bacca et al. (2)	($Q_0^2 < 1.1\,\mathrm{fm}^{-2}$)	1.518 ± 0.017	3.673 ± 0.133
Hiyama et al.	($Q_0^2 < 1.2\,\mathrm{fm}^{-2}$)	1.498 ± 0.029	4.321 ± 0.149
This work & Walcher	($Q_0^2 < 1.0\,\mathrm{fm}^{-2}$)	1.160 ± 0.093	3.097 ± 0.958
This work & Walcher	($Q_0^2 < 1.5\,\mathrm{fm}^{-2}$)	1.170 ± 0.054	3.264 ± 0.371
This work	($Q_0^2 < 1.0\,\mathrm{fm}^{-2}$)	1.544 ± 0.053	4.575 ± 0.152
This work	($Q_0^2 < 1.5\,\mathrm{fm}^{-2}$)	1.383 ± 0.037	3.994 ± 0.105

Table 9: Best estimate for monopole matrix element ME and transition radius $\mathcal{R}_{\mathrm{tr}}$ with errors for exp. data and theoretical predictions [BBLO15], performed for χ- (1) and AV18+UIX (2) potentials and [HGK04].

The agreement of the two theory approaches is within the errors reasonable, yet with marked differences.
Inspection of Fig. 57 and Tab. 9 shows, that both theoretical calculations fail to accurately reproduce the experimental matrix element ME, with the deviation from the experimental data being the largest for the calculation of Bacca et al. [BBLO15]. Due to the lack of reliable and consistent experimental data at very low Q_0^2, no firm conclusion on the nature of the monopole resonance can be drawn from this comparison. On the other side, the deviations from the experimental data are not as large as when solely comparing the transition form factor (see Fig. 55). Here, the deviation is most serious at large Q_0^2 and thus at short distances. Since the monopole transition ME is more sensitive to the long-range part of the nucleon-nucleon interaction than to the short-range part, this new finding might indicate that in both, χ- and phenomenological potentials the small hard core in the nucleon-nucleon interaction is not modeled correctly.
As already pointed out, the transition radius can also be regarded as a model independent quantity parameterising the experimental information about a nuclear level [The72]. In particular, it has been shown that the ratio $\mathcal{R}_{\mathrm{tr}}/\mathcal{R}_{\mathrm{m}}$ (with $\mathcal{R}_{\mathrm{m}}$ being the root-mean-square radius of the ground state) is considered to be approximately independent on the mass number A for E0, E1 and M1 transi-

tions, respectively (see Fig. 56). It should be noted that at the time of [The72] the case of the ^{4}He monopole resonance could only be inferred from the known systematics of other nuclei.
Using one of the most recent extractions of the root-mean-square radius of the ^{4}He ground state $\mathcal{R}_m = 1.681 \pm 0.004\,\text{fm}$ [Sic15] and our result for $\mathcal{R}_{tr}$, we obtain

$$\mathcal{R}_{tr}/\mathcal{R}_m = 1.94 \pm 0.22 \tag{74}$$

for the ratio, which nicely agrees with the expectation of $\mathcal{R}_{tr}/\mathcal{R}_m = 1.94$ from Theissen [The72].

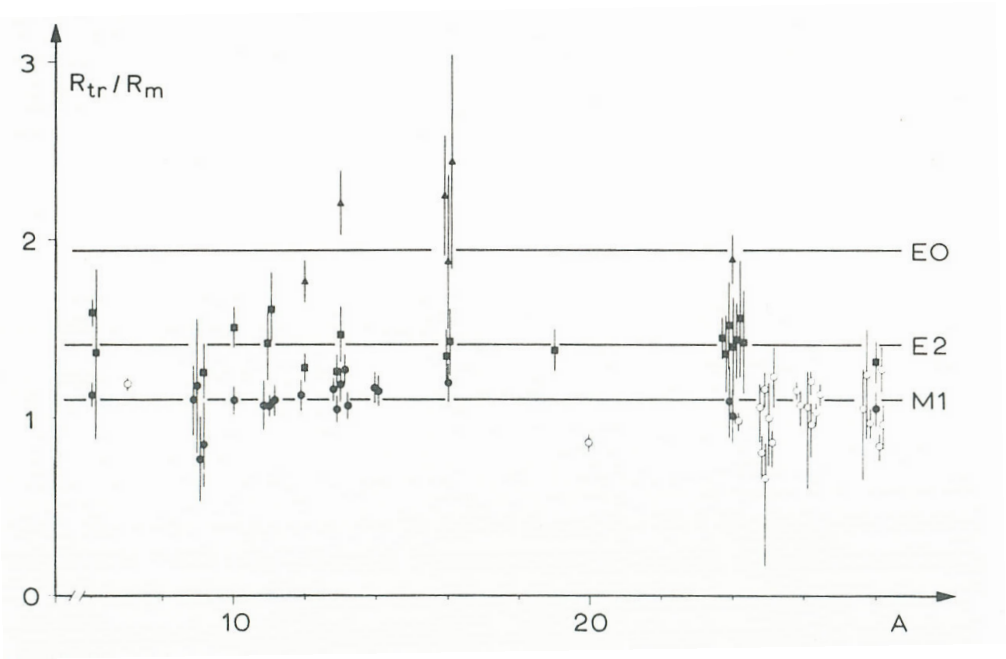

Figure 56: Ratio between the transition- and rms-radii of light nuclei for E0, E1 and M1 transitions [The72].

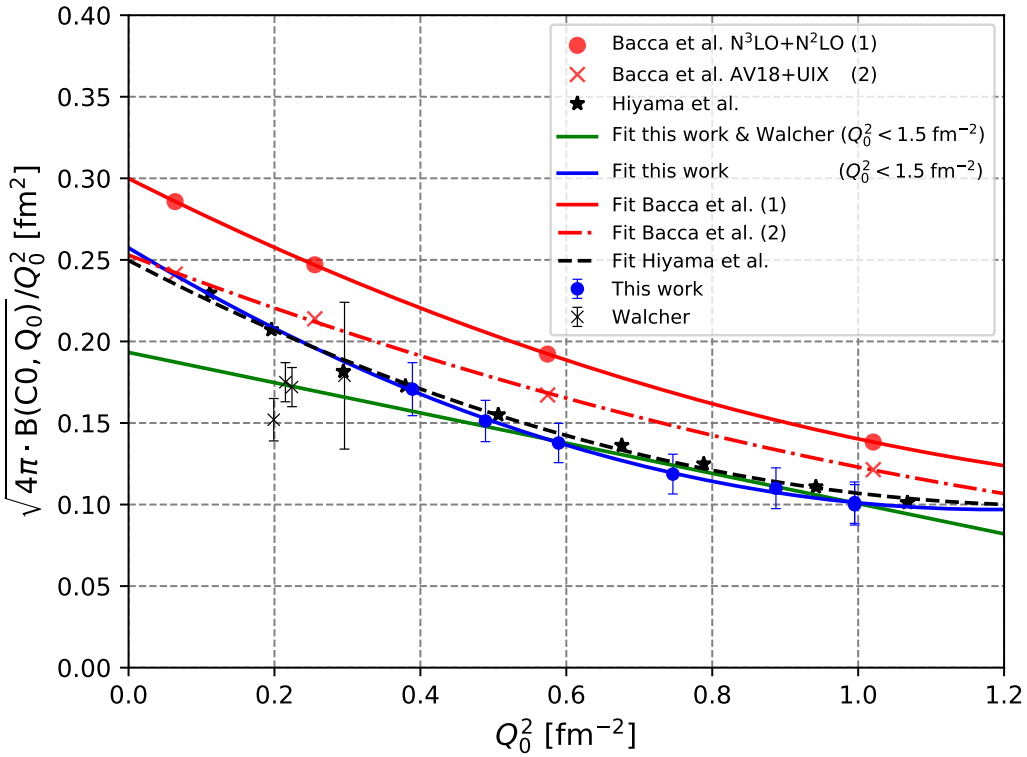

(a)

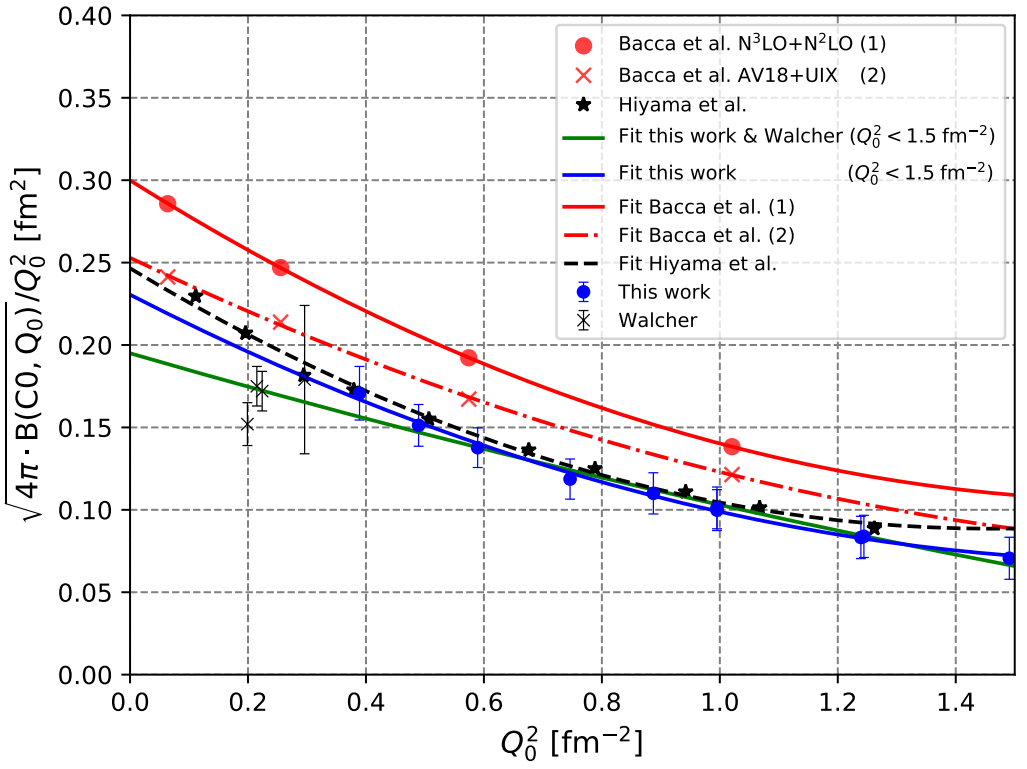

(b)

Figure 57: *(a)*: Fit at low Q_0^2 of the reduced transition probability divided by Q_0^2. The plot shows experimental data from Frosch et al. [FRC+68], Walcher [Wal70] and this experiment with theoretical calculations from Hiyama et al. [HGK04] and Bacca et al. [BBLO15], performed for χ- (1) and AV18+UIX (2) potentials. *(b)*: The same fits, with or without data from Walcher [Wal70], for extended range of $Q_0^2 < 1.5\,\mathrm{fm}^{-2}$.

10

SUMMARY & OUTLOOK

Within the scope of this work, elastic and inelastic processes of ^{4}He and also of ^{27}Al were investigated over a wide range of missing mass m_{miss} at Q^2 from $0.5\,\mathrm{fm}^{-2}$ to $5.0\,\mathrm{fm}^{-2}$.

The primary goal to extract the transition form factor $|\mathcal{F}_{\mathrm{M0}^+}(Q_0^2)|^2$ of the ^{4}He monopole was achieved with significantly decreased uncertainties compared to existing results by measuring the ground state of ^{4}He in parallel with the 0^+-resonance. Empty cell measurements with substantially reduced helium density inside the cell were used for detailed background studies of the ^{27}Al target walls. The background was extensively studied with Monte-Carlo simulations leading to an improvement in the separation of data to background. The maximum resolution of spectrometers A and B could be tested by verifying various excited states of ^{27}Al. The monopole resonance of ^{4}He was modeled by simulations using different parametrisations. The resonance model $d\sigma_2$ of J.D. Jackson, J.J. Phelan and S. Marguiles (see [Jac64], [MP68]), which describes resonances near threshold, was favoured in this analysis. Monte-Carlo simulations using this model included radiative corrections of leading orders. The intrinsic *full-width-at-half-maximum* Γ_0 of the monopole was determined with these Monte-Carlo techniques. The results for Γ_0 agree with existing values of Frosch et al. [FRC$^+$68], Walcher [Wal70], and Köbschall et al. [KOM$^+$83]. Although the continuum of ^{27}Al could be described in the theoretical framework of off-shell-electron-scattering by T. deForest [For83], the continuum of ^{4}He could not be completely described due to the presence of other resonances. Therefore, a phenomenological model of the background based on sophisticated physical properties of the continuum was used to fit the continuum. The influence of the different background and resonance models on the transition form factor was investigated by analysing different combinations of models in parallel. The model uncertainty on the results of the width Γ_0 and the transition form factor are small and have been incorporated into a model confidence band for the transition form factor $|\mathcal{F}_{\mathrm{M0}^+}(Q_0^2)|^2$. The experimental systematic errors are based on the uncertainty of the elastic ^{4}He form factor, the background subtraction to isolate the monopole resonance and the ^{4}He continuum, and on the uncertainty of the width Γ_0 (which is the major systematic uncertainty).
On the basis of the extracted transition form factor values with considerably reduced uncertainty it can be concluded that no existing theoretical model is sensitive to describe the processes of the monopole excitation completely. The results of this work, extracted over the full Q_0^2-range of interest, might open

the possibility to tune the existing theoretical models. The high precision of the data allows a better validation of improved calculations tuned by either an extension of the χ-expansion to higher orders or a modified nucleon-nucleon interaction.

Multiple projects can be influenced by the results of this thesis.
On the experimental side, improvements to electron scattering on gas targets are proposed and implemented by the gas jet target MAGIX[1] [MAG15]. The clear advantage of this target is its windowless design which allows a large improvement on the experimental resolution by avoiding background from the target walls. At MESA[2] [Exc16] the low-energy range will allow an extension of these studies to very low Q^2 and thus a more precise extraction of the monopole matrix element ME and the transition radius $\mathcal{R}_{\text{tr}}$.
The new, more precise data has inspired theoreticians to recalculate the transition form factor and search for the reasons of the deviation between data and predictions, which is, at the time of writing, unresolved.

1 **M**es**a** **G**as **I**nternal Target E**X**periment
2 **M**ainz **E**nergy-Recovering **S**uperconducting **A**ccelerator

A

Q_0^2 OF RESONANCES

The Q^2 for low-lying excited states and the ground state do not differ much. There are still two differences:

i) The recoil energy of the nucleus, with its mass being increased by the excitation energy, is slightly different compared to the case of elastic scattering.

ii) The Q_0^2 of the resonance is corrected by the excitation energy E_{ex}, which is in addition transferred to the nucleus by the virtual photon.

The first effect is small, because the (central) energy $E_{\text{ex}} = 20.21\,\text{MeV}$ to excite the resonance is negligible compared to the rest mass of ^{4}He with $M = 3727.38\,\text{MeV}$. Concerning the second point, Q_0^2 needs to be reduced by the energy, which the electron looses to excite the resonance. For the calculation of E', the formulaes from [Ueb71] are adopted

$$E_f = \frac{(E_i - K)}{1 + (\frac{2 \cdot E_i}{M})} \cdot \sin^2 \frac{\theta}{2} \tag{75a}$$

$$K = E_{\text{ex}} \cdot (1 + \frac{E_{\text{ex}}}{2 \cdot M}) \tag{75b}$$

where E_i is the initial and E_f the final electron energy, M the ^{4}He rest mass, θ the scattering angle and K a recoil-corrected excitation energy. These modifications are applied to the calculation of four-vectors for the monopole resonance. The excitation energy E_{ex} follows the distribution of the parametrisations $d\sigma_1$ and $d\sigma_2$ (see Tab. 5), which is accounted for in the calculation of Q_0^2, the squared four-momentum of the monopole. This leads to a more accurate determination of Q_0^2, compared to simply using the central energy $E_{\text{ex}} = 20.21\,\text{MeV}$ of the resonance. In Fig. 58 distributions of squared four-momenta for spectrometer B are shown, for the monopole resonance (see Fig. 58a) and for the elastic peak (see Fig. 58b), respectively. The kinematic parameters are the same for both distributions, which exhibit a slightly different central four-momentum for both scattering processes. The distribution of the elastic peak also shows a steeper decrease at larger $\widetilde{Q}^2$-values caused by a stronger decrease of the elastic form factor of ^{4}He at larger four-momenta.

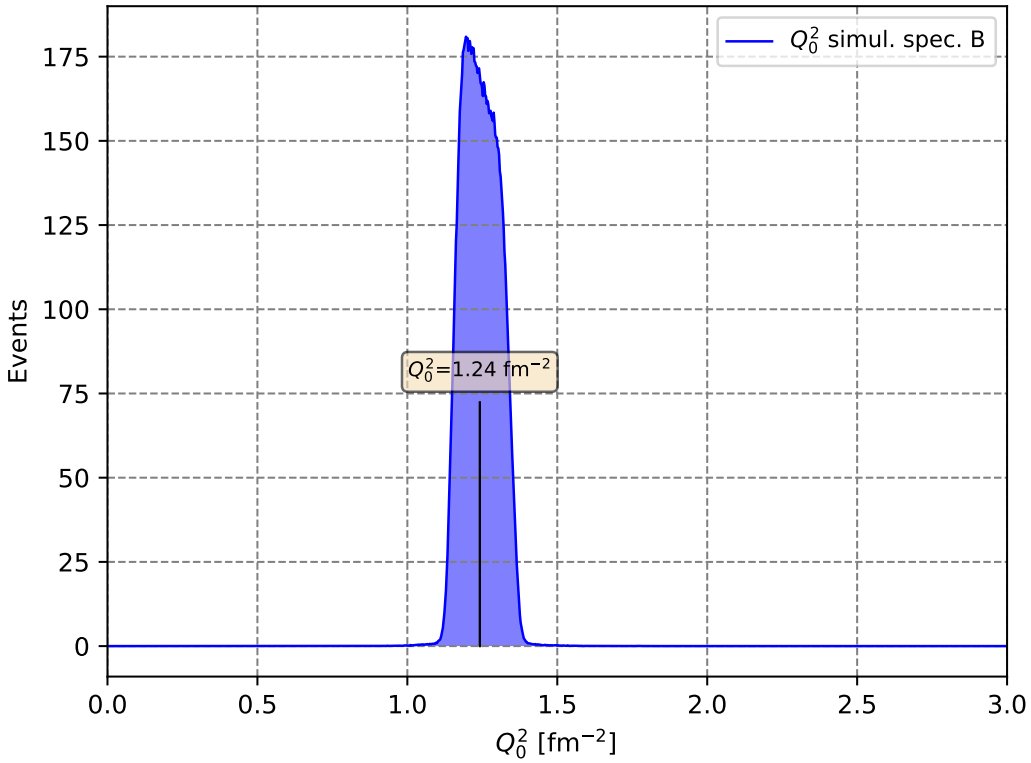

(a)

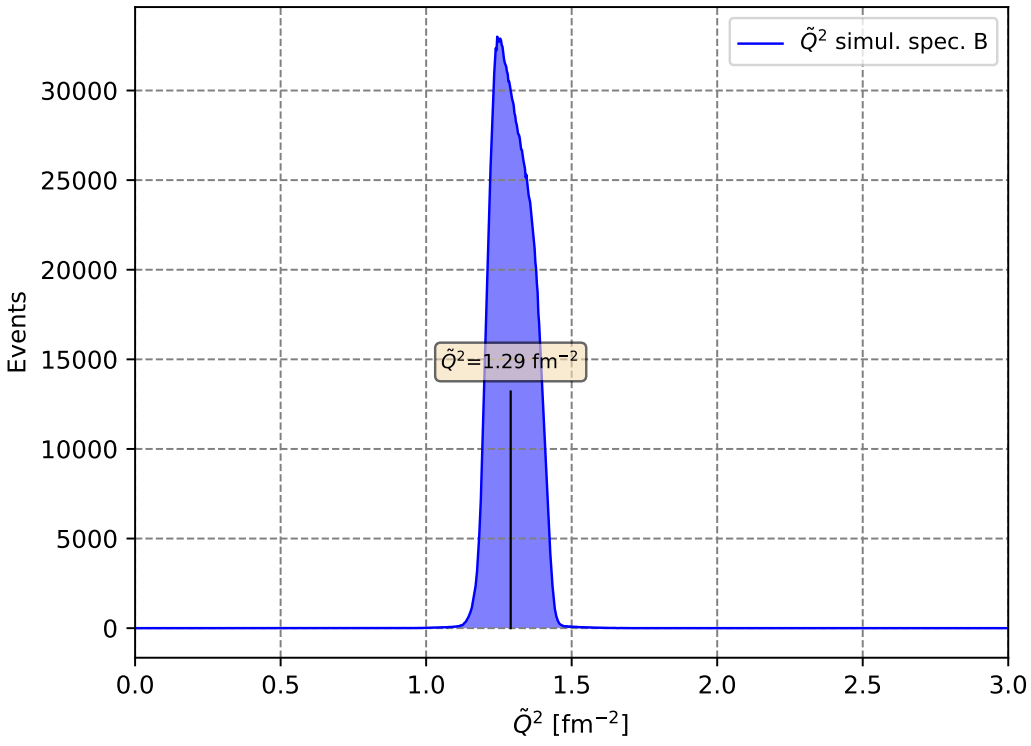

(b)

Figure 58: *(a)*: Distribution of squared four-momentum Q_0^2 of the monopole resonance. *(b)*: squared four-momentum $\tilde{Q}^2$ from elastic scattering. The central values and the shapes of the distributions show differences due to the distinction of the two underlying quantities.

B

^{4}HE CONTINUUM

The investigation of resonances located in the continuum requires to deal with quasi-elastic processes. Quasi-elastic scattering refers to the scattering of electrons with enough energy to interact with particular nucleons inside the nucleus as quasi-free. The quasi-elastic peak is a component in nuclear spectra related to these processes, centered at $\omega \approx Q^2/2M + E_{\text{thr}}$ with nucleon mass M, break-up energy E_{thr}, and squared electron four-momentum Q^2. Quasi-elastic scattering reveals information about momentum distributions of protons and neutrons inside the nucleus. The following part shall give a brief introduction into quasi-elastic processes in electron scattering in general and in particular in the case of ^{4}He.
The framework for nucleon-knock-out reactions is usually embedded in PWIA[1] under the following assumptions:

- only one-photon exchange is considered in the interaction of the virtual photon and the nucleon. Higher photon-exchange terms are discarded.
- *Final State Interactions* (FSI) of the nucleon with the residual nucleus after its ejection are neglected.

Another assumption is, that the momentum of the emitted nucleon and $\vec{q}$, the vector of the virtual photon, are parallel. Fig. 59 shows a Feynman diagram of the interaction.
As already pointed out in Sec. 5.4, the cross section of quasi-elastic scattering

$$\frac{d\sigma^6}{d\Omega_e dE'_e d\Omega_p dE'_N} = k'_N E'_N \sigma_{eN} S(k_m, E_m) \tag{76}$$

can be factorised into an elementary electron-nucleon cross section σ_{eN}, a spectral function $S(k_N, E_N)$, and a kinematic factor $k'_N E'_N$ [For83].

1 **P**lane-**W**ave-**I**mpulse-**A**pproximation

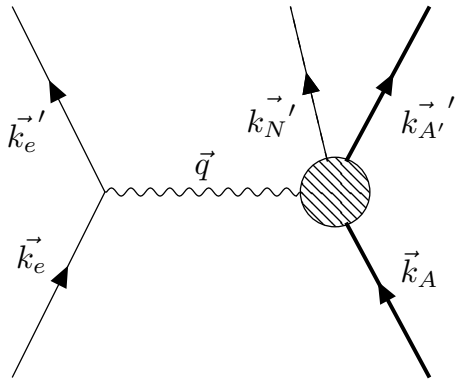

Figure 59: Feynman graph of nucleon knock-out. The angle between knocked-out nucleon and $\vec{q}$ is assumed to be close to 0°, an assumption called parallel kinematics.

The notation is as follows:

- $\vec{k_e}$ and $\vec{k'}_e$ are the initial and final three-momenta of the electron interacting with the nucleon, E_e and E'_e its initial and final energy.
- $\vec{k_N}$ and $\vec{k'}_N$ are the initial and final three-momenta of the nucleon interacting with the electron, E_N and E'_N its initial and final energy.
- $\vec{k_A}$ and $\vec{k'}_{A'}$ are the initial and final three-momenta of the nucleus, E_A and $E'_{A'}$ its initial and final energy, where usually $\vec{k_A} = 0$ and $E_A = M_0$.
- The four-momentum transfer is given by $q_\mu = (\omega, \vec{k'}_e - \vec{k_e}) = (\omega, \vec{q})$, with $Q^2 = -q_\mu q^\mu$.
- M_A, M_N, and $M_{A'}$ are the rest masses of the nuclei or nucleons.

The missing momentum $\vec{k}_{\text{miss}}$ can be calculated due to momentum conservation at the vertex

$$\vec{k}_{\text{miss}} = -\vec{k}_N = \vec{q} - \vec{k}'_{A'} \ . \tag{77}$$

The missing energy E_{miss} is the excitation energy transfered to the (A-1)-residual nucleus:

$$E_{\text{miss}} = \omega - \left(\sqrt{{k_N}'^2 + {M_N}^2} - M_N\right) - \left(\sqrt{{k_{A'}}'^2 + {M_{A'}}^2} - M_{A'}\right) \tag{78}$$

For the simulation of quasi-elastic processes, ${k'}_N$ and ${E'}_N$ can be calculated with the given assumptions, where the initial target mass is at rest and the electron energy and momentum are determined by the kinematic. For the elementary electron-nucleon cross section σ_{eN}, the more commonly $\sigma_{\mathrm{eN}} = \sigma_{\mathrm{CC1}}$ is used (see [For83]). The spectral function $S(k_{\mathrm{miss}}, E_{\mathrm{miss}})$ in (76) is often replaced by a nucleon momentum distribution $n(k_{\mathrm{miss}})$. Those two quantities are related via

$$S(k_{\mathrm{miss}}, E_{\mathrm{miss}}) \approx \frac{1}{A} n(k_{\mathrm{miss}}) \cdot \delta(E - \bar{E}_s - \frac{|\vec{q}|}{2M_A}) \,, \tag{79}$$

where $\bar{E}_s$ is the average nucleon removal energy:

$$\bar{E}_s = \int E \cdot S(k_{\mathrm{miss}}, E_{\mathrm{miss}}) \, d^3k \, dE. \tag{80}$$

The approximation concerning the two-body break-up of ^{4}He, only proton or neutron knock-out processes are taken into account:

- $^4\mathrm{He} + e \rightarrow X + p + e'$
- $^4\mathrm{He} + e \rightarrow X + n + e'$

The momentum-density distribution $n(k_{\mathrm{miss}})$ of protons and neutrons is assumed to be equivalent. However, the residual 3N-system can undergo further break-up reactions like three- or four-body break-up. The authors of [ELO98] calculated the spectral function of the ^{4}He residual 3N-system for the full excitation spectrum embedded in this simulation.
In Fig. 60a and Fig. 60b, the proton momentum-density distribution from [WSPC14] and spectral function from [ELO98] used for the simulation are shown. The corresponding values of $n(k_{\mathrm{miss}})$ and $S(k_{\mathrm{miss}}, E_{\mathrm{miss}})$ are interpolated by cubic- or bicubic-spline interpolation, respectively.
Quasi-elastic processes have been simulated with (76) using these interpolated values of the proton momentum-density distribution from [WSPC14] and the spectral function from [ELO98] (see Fig. 60).
In Fig. 61a a comparison of the simulations for quasi-elastic scattering at $Q^2 = 2.0\,\mathrm{fm}^{-2}$ is shown for proton or neutron knock-out only and for both knock-out reactions added. The final state of the residual nucleus is in this case either ^{3}He or ^{3}H. Fig. 61b shows the simulations in comparison to data for the same kinematic. The contribution from the ^{4}He tail and the background from ^{27}Al have been subtracted as described in Sec. 6.2. While the simulation at higher missing mass emulates the data, the part close to the monopole includes unknown contributions. These unknown contributions are supposed to originate from other resonances such as a giant resonance of ^{4}He at 25.98 MeV. A full simulation of the continuum would also include the D-D break-up of ^{4}He, which was not investigated in this work. The strength of this contribution to the spectra thus remains unknown. These circumstances make it necessary to fit the continuum with an appropriate parametrisation (see Sec. 6.3).

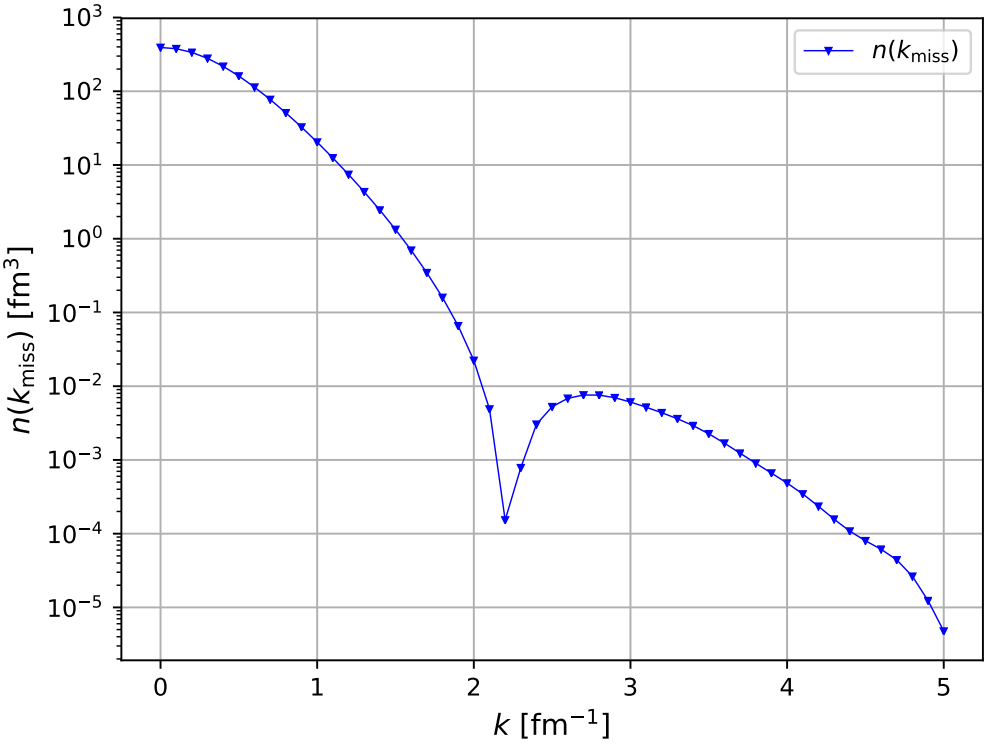

(a)

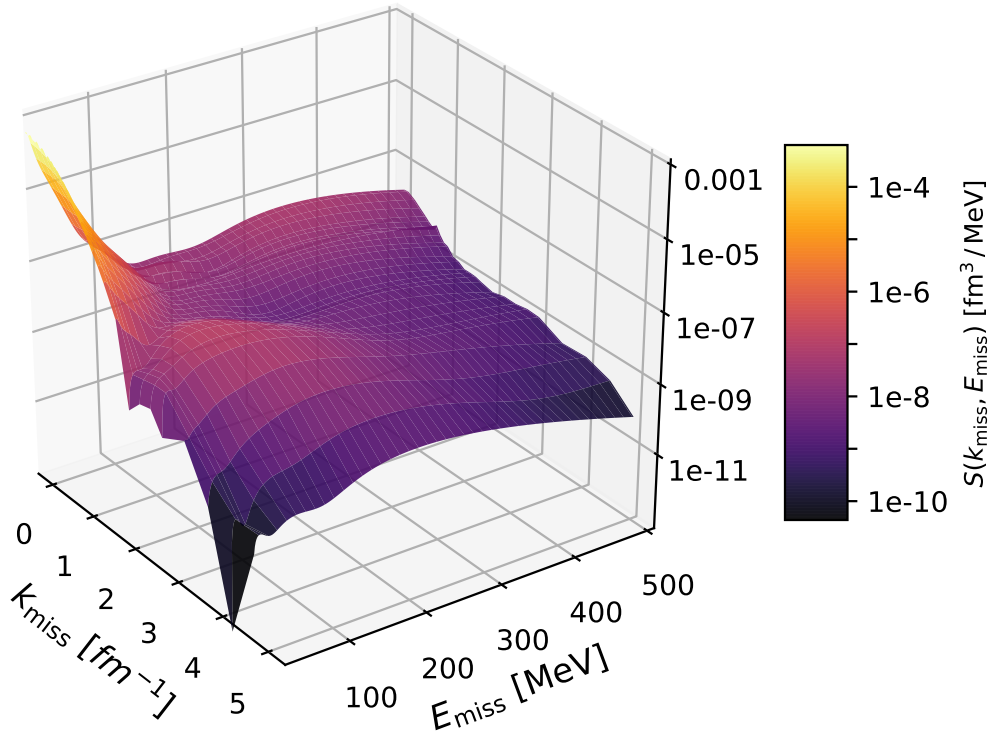

(b)

Figure 60: (a): Proton momentum density distribution $n(k_{\text{miss}})$ [WSPC14] (b): spectral function $S(k_{\text{miss}}, E_{\text{miss}})$ for 3-& 4-body break-up of the residual 3N-system of ^{4}He [ELO98].

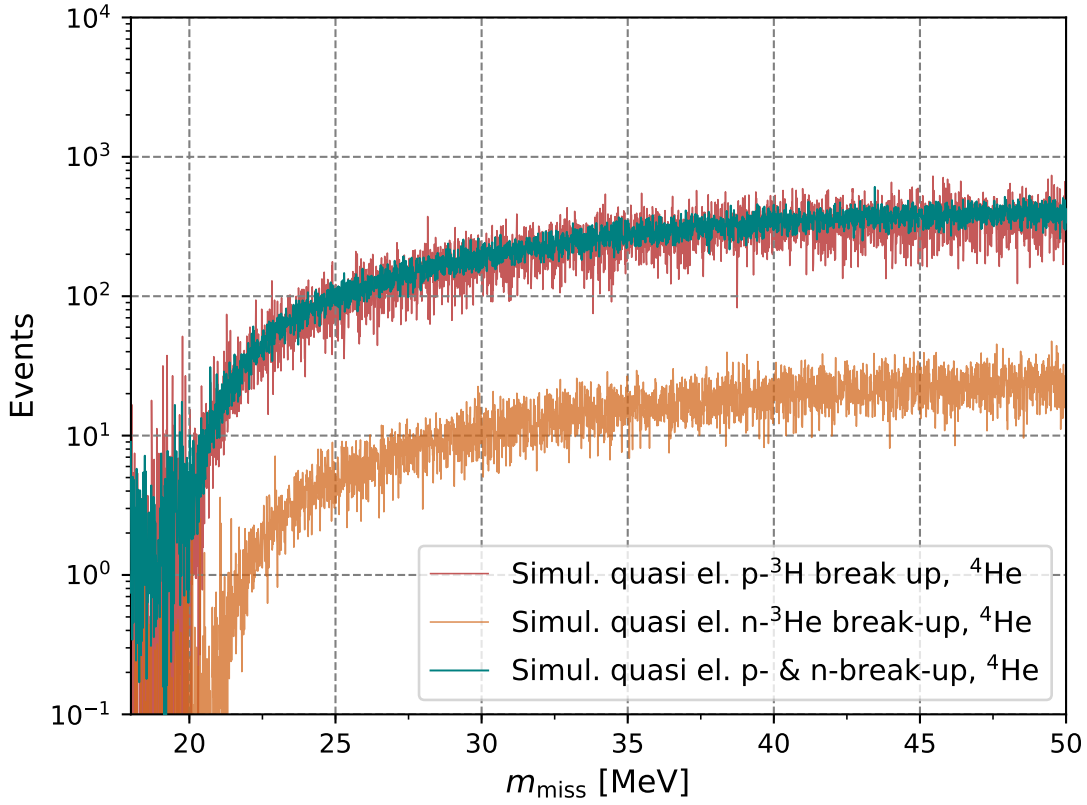

(a)

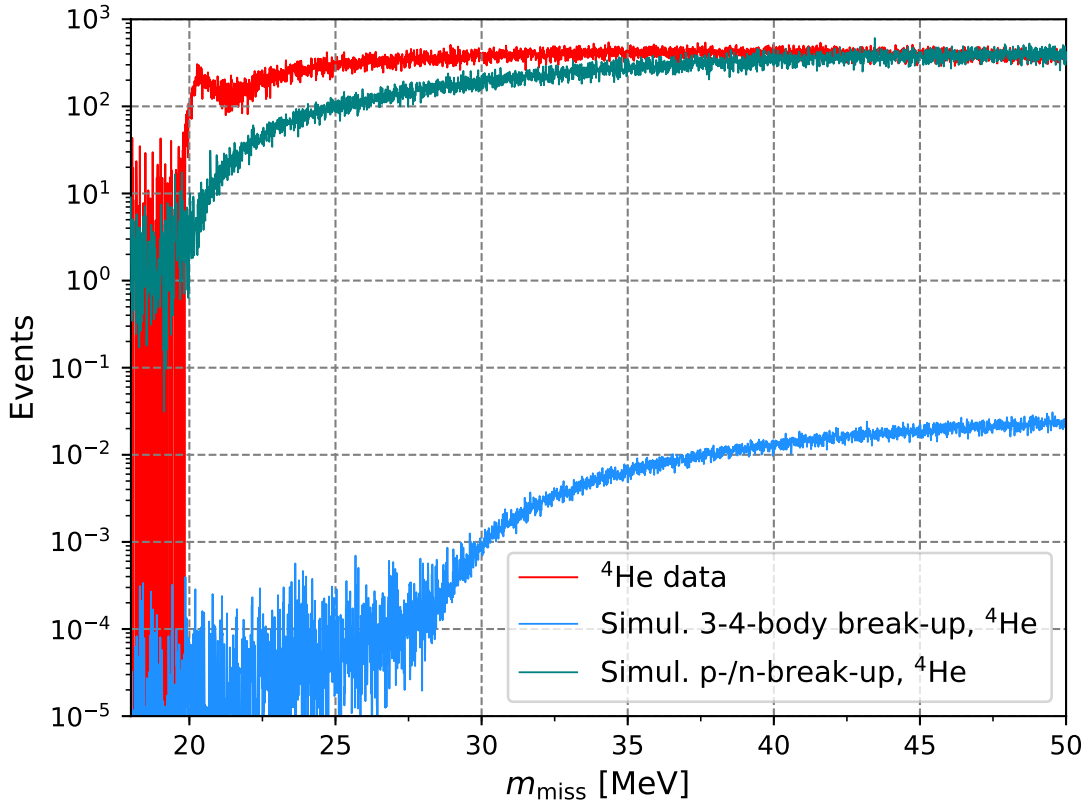

(b)

Figure 61: (a): Comparison between simulations with proton or neutron break-up and both break-up configurations added. (b): Comparison of the simulations to data at $Q^2 = 2.0\,\mathrm{fm}^{-2}$.

C

FORM FACTOR PARAMETRISATIONS

Two models are used to describe the transition form factor in Sec. 9.2: A 3$^{\text{rd}}$ order polynomial $B(Q_0^2)$ composed of basis-splines $b_{i,p=3,k}(Q_0^2)$ with knot-vector k, and an approach of a low-order polynomial multiplied by an exponential function.
The first step of the basis-spline procedure is to choose m knots $k_l \in \{0, 0.5, 1.5, 2.5, 7\}$ in the given data set. Once these knots are fixed, the basis-spline polynomials are calculated by recursive formulaes where p is the order of the polynomial:

$$b_{i,0,k}(x) = \begin{cases} 1, & x \in [k_i, k_{i+1}[\\ 0, & \text{otherwise} \end{cases} \tag{81a}$$

$$b_{i,p,k}(x) = \frac{x - k_i}{k_{i+p} - k_i} b_{i,p-1,k}(x) + \frac{k_{i+1} - x}{k_{i+p+1} - k_{i+1}} b_{i+1,p-1,k}(x) \ , \ p > 0 \tag{81b}$$

$$\frac{d}{dx} b_{i,p,k}(x) = \frac{p}{k_{i+p} - k_i} b_{i,p-1,k}(x) - \frac{p}{k_{i+p+1} - k_{i+1}} b_{i+1,p-1,k}(x) \ , \ p > 1 \tag{81c}$$

In order to obtain the coefficients of the polynomials, one creates a knot vector by adding k_0 and k_m p times at the beginning and end to the knot vector, yielding $\vec{k} = \{0, 0, 0, 0, 0.5, 1.5, 2.5, 7, 7, 7, 7\}$ with $\dim(\vec{k}) = m + 2p$. The number of basis splines $b_{i,p,k}(x)$ is then given by $m + p - 1$, in this particular case yielding seven basis splines for five knots (see Fig. 62).
If the data set to fit has N data points (x_i, y_i), the minimisation can be calculated with the matrix method and solved for the basis-spline coefficients with the system matrix $\mathbf{A}_{ij} = b_{j,p,k}(x_i)$ with $j = 1..(m + p - 1)$ and $i = 1..N$. Boundary conditions $B(0) = 0$ and $B'(7) = 0$ (see (68) in Sec. 9.2) are included into matrix $\mathbf{A}_{ij}$ by adding rows with these specific conditions to $\mathbf{A}$.

$$\vec{c} = (\mathbf{A}^\top \cdot \mathbf{W} \cdot \mathbf{A})^{-1} \cdot \mathbf{A}^\top \cdot \mathbf{W} \vec{y} \tag{82a}$$

$$\mathbf{V} = (\mathbf{A}^\top \cdot \mathbf{W} \cdot \mathbf{A})^{-1} \tag{82b}$$

Here, the matrix $\mathbf{W}$ is a weight matrix with $1/(y_i)^2$ as diagonal elements, where y_i are the errors of the data. The covariance matrix $\mathbf{V}$ is required for the error

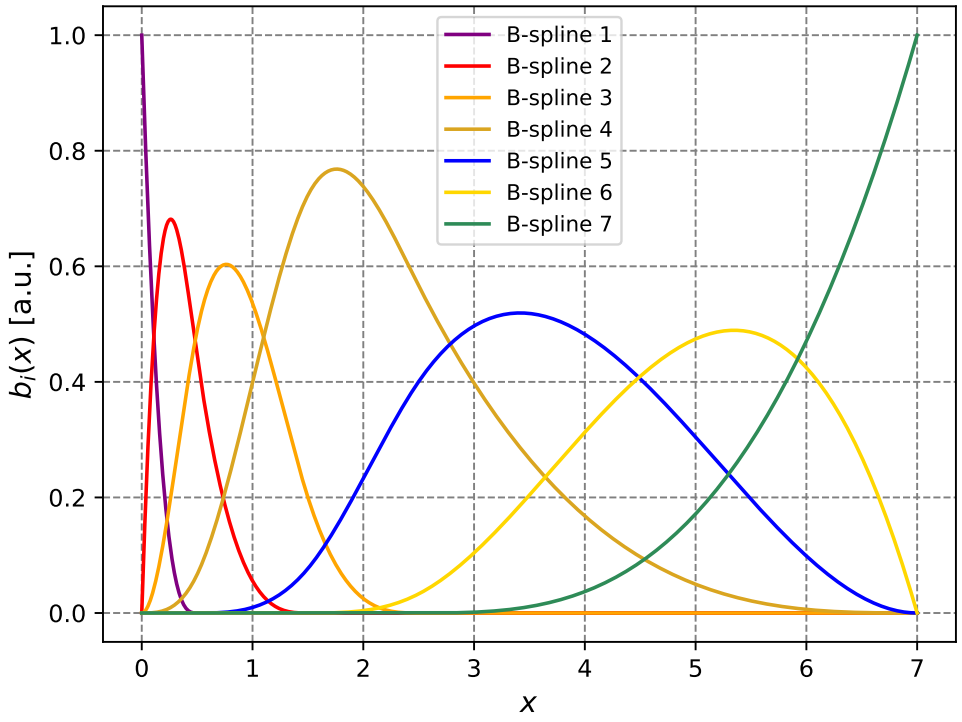

Figure 62: Basis of splines calculated by the recursion formulas from (81).

calculation of parameters c_i with $\Delta c_i = \mathbf{V}_{ii} c_i$ and the error band of the spline fit. The coefficients $\vec{c}$ obtained to fit the transition form factor with the conditions from Sec. 9.2 are shown in Tab. 10. These coefficients c_i are multiplied to $b_{i,p,k}(x)$ to get a parametrisation of the transition form factor $|\mathcal{F}_{\mathrm{M0^+}}(Q_0^2)|^2$ with basis-splines as shown in Fig. 53.

	c_i	Δc_i
c_0	0.000	$\pm$ 0.000
c_1	0.184	$\pm$ 0.026
c_2	1.761	$\pm$ 0.158
c_3	2.591	$\pm$ 0.120
c_4	0.423	$\pm$ 0.022
c_5	0.051	$\pm$ 0.002
c_6	0.052	$\pm$ 0.003

Table 10: Coefficients c_i of the basis splines.

The second model to fit the transition form factor is a product of a polynomial with an exponential function with a negative exponent ($\alpha > 0$):

$$f_{\mathrm{FF2}}(Q_0^2) = \underbrace{(a_0 + a_1 \cdot Q_0^2 + a_2 \cdot (Q_0^2)^2 + a_3 \cdot (Q_0^2)^3)}_{\mathcal{P}(Q_0^2)} \cdot \exp(-\alpha Q_0^2). \tag{83}$$

This model has the advantages, that $f_{\mathrm{FF2}}(0) = 0$ if $a_0 = 0$, and that with the exponential function the transition form factor vanishes at large Q_0^2. In order to investigate which coefficients a_i to keep or omit in $\mathcal{P}(Q_0^2)$, all combinations of coefficients have been tried with regard to the minimal χ^2. Accordingly, the final form of (83) reduces to

$$f_{\mathrm{FF2}}(Q_0^2) = (a_1 \cdot Q_0^2 + a_2 \cdot (Q_0^2)^2) \cdot \exp(-\alpha Q_0^2)\ . \tag{84}$$

The final parameters to fit the transition form factor with $f_{\mathrm{FF2}}(Q_0^2)$ are given in Tab. 11. In Fig. 63 the final parametrisations by basis-splines and polynomial function from (84) is shown with the transition form factor data from this work.

Parameter	Value	Error
a_1	0.930	$\pm$0.203
a_2	5.505	$\pm$0.292
α	1.260	$\pm$0.015

Table 11: Fit parameters of (84) with errors.

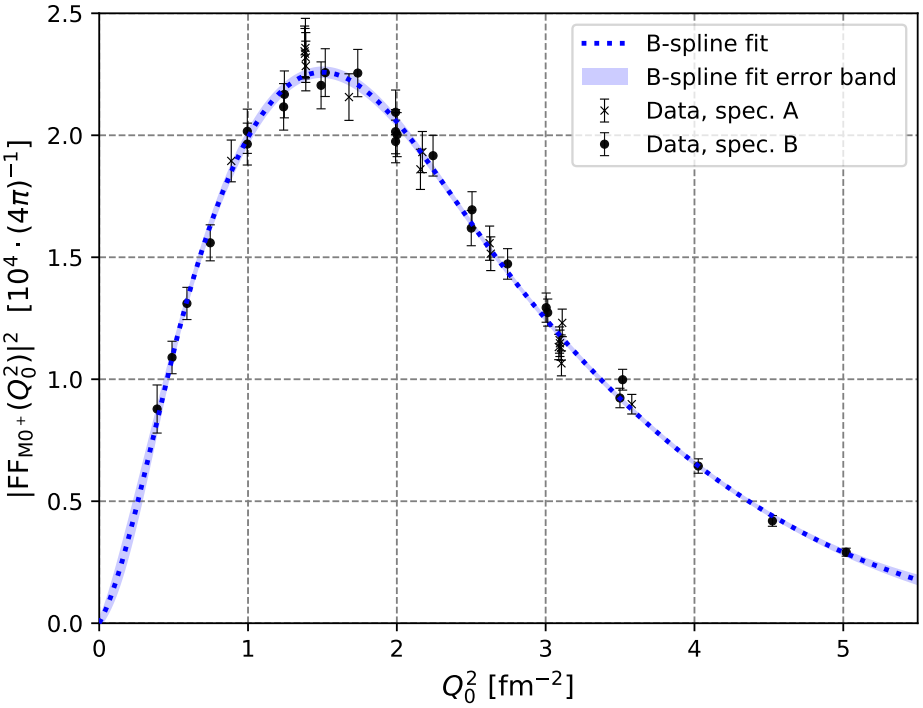

(a)

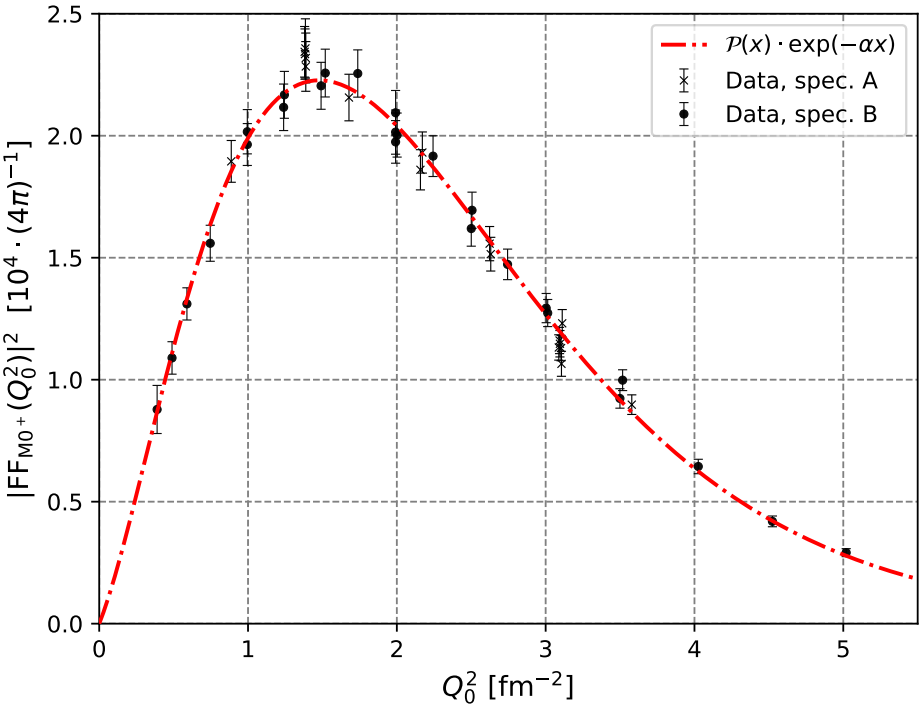

(b)

Figure 63: Both fit models for $|\mathcal{F}_{\mathrm{M0}^+}(Q_0^2)|^2$ with data. *(a)* Basis-spline fit. *(b)*: Polynomial function (84).

D

SETUPS INCLUDED IN THE ANALYSIS

Setup	E [MeV]	θ_A [°]	θ_B [°]	$p_{cent.,A}$ [MeV/c]	$p_{cent.,B}$ [MeV/c]
4HE450A261B293EC	450.20	26.10	29.29	435.344	435.792
4HE450A322B163EC	450.20	32.21	16.31	415.363	430.763
4HE450A323B164EC	450.20	32.31	16.40	431.325	440.536
4HE450A323B183EC	450.20	32.31	18.30	431.345	440.007
4HE450A323B201EC	450.20	32.31	20.10	431.346	438.583
4HE450A323B226EC	450.20	32.31	22.60	431.340	438.583
4HE450A323B262EC	450.20	32.31	26.20	431.344	435.764
4HE690A240B240EC	690.18	24.01	24.00	644.935	673.027
4HE690A270B255EC	690.18	27.01	25.50	644.915	671.978
4HE690A297B270EC	690.18	29.70	27.00	644.878	670.949
4HE690A297B283EC	690.18	29.70	28.30	644.862	668.948
4HE690A322B169EC	690.18	32.21	16.90	644.898	679.174
4HE690A322B189EC	690.18	32.21	18.90	644.888	677.075
4HE690A322B207EC	690.18	32.21	20.07	644.885	676.045
4HE690A322B224EC	690.18	32.21	22.40	644.905	675.006
4HE690A322B297EC	690.18	32.21	29.70	644.868	667.909
4HE690A345B322EC	690.18	34.51	32.21	644.844	664.936
4HE690A368B345EC	690.18	36.80	34.50	644.819	661.862
4HE795A337B181EC	795.18	33.71	18.11	644.886	781.424
4HE795A337B208EC	795.18	33.71	20.80	644.786	778.275
4HE795A337B233EC	795.18	33.71	23.30	644.867	776.002
4HE795A337B256EC	795.18	33.71	25.60	644.857	772.728
4HE795A337B277EC	795.18	33.71	27.70	644.854	769.777
4HE795A337B298EC	795.18	33.71	29.80	644.854	766.729
4HE795A337B317EC	795.18	33.71	31.70	644.845	763.818

Table 12: List of empty cell setups for spectrometer A and B used in this analysis.

Setup	E [MeV]	θ_A [°]	θ_B [°]	$p_{cent.,A}$ [MeV/c]	$p_{cent.,B}$ [MeV/c]
4HE450A261B293	450.20	26.10	29.31	435.060	435.468
4HE450A322B163	450.20	32.21	16.31	414.962	429.970
4HE450A323B183	450.20	32.31	18.30	431.032	439.287
4HE450A323B201	450.20	32.31	20.10	431.023	438.197
4HE450A323B226	450.20	32.31	22.60	431.030	438.237
4HE450A323B262	450.20	32.31	26.20	431.033	435.454
4HE690A240B240	690.18	24.01	24.00	644.607	672.798
4HE690A270B240	690.18	27.01	24.00	644.591	672.758
4HE690A270B255	690.18	27.01	25.50	644.570	671.777
4HE690A297B270	690.18	29.70	27.00	644.562	670.756
4HE690A297B283	690.18	29.70	28.30	644.564	668.709
4HE690A322B169	690.18	32.21	16.90	644.617	678.765
4HE690A322B189	690.18	32.21	18.90	644.588	676.805
4HE690A322B207	690.18	32.21	20.71	644.582	675.874
4HE690A322B224	690.18	32.21	22.40	644.557	674.773
4HE690A322B240	690.18	32.21	24.00	644.552	672.773
4HE690A322B297	690.18	32.21	29.70	644.499	667.705
4HE690A345B322M2	690.18	34.51	32.21	644.550	664.744
4HE795A337B181	795.18	33.71	18.11	644.876	780.824
4HE795A337B208	795.18	33.71	20.80	644.850	777.837
4HE795A337B233	795.18	33.71	23.30	644.845	775.764
4HE795A337B256	795.18	33.71	25.60	644.819	772.728
4HE795A337B277	795.18	33.71	27.70	644.874	769.347
4HE795A337B298	795.18	33.71	29.80	644.874	766.595
4HE795A337B317	795.18	33.71	31.70	644.811	763.665
4HE795A337B335	795.18	33.71	33.50	644.887	761.837

Table 13: List of setups for spectrometer A and B used in this analysis.

Legend:

- Setup: (EC-)setup name in data acquisition and data base
- E: beam energy [MeV]
- $\theta_{<A,B>}$: nominal spectrometer angle [°]
- $p_{cent.,<A,B>}$: spectrometer central momentum [MeV/c]

E

DATA TABLES

Setup	$\widetilde{Q}^2$ [fm^{-2}]	Q_0^2 [fm^{-2}]	$\lvert\mathcal{F}_{\text{ratio}}({Q_0}^2)\rvert^2$	$\Delta\lvert\mathcal{F}_{\text{ratio}}({Q_0}^2)\rvert^2$
4HE450A261B293	0.92	0.94	0.003 749	0.000 332
4HE450A322B163	1.45	1.41	0.007 631	0.000 707
4HE450A323B183	1.44	1.42	0.007 205	0.000 674
4HE450A323B201	1.44	1.42	0.007 462	0.000 694
4HE450A323B226	1.44	1.42	0.007 130	0.000 655
4HE450A323B262	1.44	1.42	0.007 313	0.000 687
4HE690A240B240	1.60	1.78	0.011 189	0.001 117
4HE690A270B240	2.09	2.23	0.016 048	0.001 631
4HE690A270B255	2.09	2.23	0.015 907	0.001 615
4HE690A297B270	2.56	2.69	0.019 798	0.002 015
4HE690A297B283	2.56	2.69	0.018 571	0.001 890
4HE690A322B169	3.02	3.15	0.023 507	0.002 392
4HE690A322B189	3.02	3.15	0.023 708	0.002 413
4HE690A322B207	3.02	3.15	0.023 655	0.002 407
4HE690A322B224	3.02	3.15	0.023 303	0.002 371
4HE690A322B240	3.01	3.15	0.023 747	0.002 417
4HE690A322B297	3.01	3.15	0.024 476	0.002 491
4HE690A345B322M2	3.48	3.60	0.026 382	0.002 685

Table 14: List of Q^2 and form factor ratio $\lvert\mathcal{F}_{\text{ratio}}({Q_0}^2)\rvert^2$ of the first iteration, spectrometer A.

Setup	$\widetilde{Q}^2$ [fm^{-2}]	Q_0^2 [fm^{-2}]	$\lvert\mathcal{F}_{\text{ratio}}(Q_0{}^2)\rvert^2$	$\Delta\lvert\mathcal{F}_{\text{ratio}}(Q_0{}^2)\rvert^2$
4HE450A261B293	1.30	1.25	0.005 568	0.000 509
4HE450A322B163	0.41	0.40	0.001 083	0.000 091
4HE450A323B183	0.51	0.50	0.001 293	0.000 114
4HE450A323B201	0.62	0.60	0.001 838	0.000 156
4HE450A323B226	0.78	0.76	0.002 576	0.000 226
4HE450A323B262	1.04	1.01	0.004 145	0.000 370
4HE690A240B240	2.04	2.01	0.011 745	0.001 125
4HE690A270B240	2.04	2.01	0.011 321	0.001 097
4HE690A270B255	2.30	2.26	0.013 159	0.001 305
4HE690A297B270	2.60	2.53	0.014 926	0.001 444
4HE690A297B283	2.81	2.76	0.016 048	0.001 567
4HE690A322B169	1.03	1.02	0.004 469	0.000 419
4HE690A322B189	1.27	1.26	0.006 195	0.000 590
4HE690A322B207	1.53	1.51	0.007 979	0.000 764
4HE690A322B224	1.80	1.76	0.009 687	0.000 927
4HE690A322B240	2.04	2.01	0.011 437	0.001 109
4HE690A322B297	3.10	3.03	0.017 954	0.001 755
4HE690A345B322M2	3.61	3.54	0.020 617	0.001 977
4HE795A337B181	1.56	1.54	0.008 390	0.000 826
4HE795A337B208	2.05	2.02	0.011 995	0.001 200
4HE795A337B233	2.57	2.52	0.015 153	0.001 524
4HE795A337B256	3.08	3.02	0.018 583	0.001 893
4HE795A337B277	3.57	3.51	0.021 881	0.002 217
4HE795A337B298	4.11	4.04	0.024 180	0.002 463
4HE795A337B317	4.61	4.54	0.025 907	0.002 594
4HE795A337B335	5.14	5.05	0.030 958	0.003 152

Table 15: List of Q^2 and form factor ratio $\lvert\mathcal{F}_{\text{ratio}}(Q_0{}^2)\rvert^2$ of the first iteration, spectrometer B.

Setup	$\widetilde{Q}^2$ [fm^{-2}]	Q_0^2 [fm^{-2}]	$\lvert\mathcal{F}_{\text{ratio}}(Q_0{}^2)\rvert^2$	$\Delta\lvert\mathcal{F}_{\text{ratio}}(Q_0{}^2)\rvert^2$
4HE450A261B293	0.91	0.89	0.003 948	0.000 350
4HE450A322B163	1.42	1.39	0.008 072	0.000 748
4HE450A323B183	1.42	1.38	0.007 568	0.000 708
4HE450A323B201	1.42	1.39	0.007 802	0.000 725
4HE450A323B226	1.42	1.39	0.007 454	0.000 685
4HE450A323B262	1.42	1.38	0.007 717	0.000 725
4HE690A240B240	1.72	1.68	0.011 032	0.001 102
4HE690A270B240	2.20	2.17	0.015 277	0.001 553
4HE690A270B255	2.20	2.16	0.015 286	0.001 552
4HE690A297B270	2.69	2.62	0.018 759	0.001 909
4HE690A297B283	2.69	2.63	0.017 472	0.001 778
4HE690A322B169	3.18	3.11	0.021 097	0.002 147
4HE690A322B189	3.17	3.10	0.021 683	0.002 207
4HE690A322B207	3.17	3.09	0.021 583	0.002 196
4HE690A322B224	3.17	3.11	0.021 014	0.002 138
4HE690A322B240	3.17	3.09	0.021 718	0.002 210
4HE690A322B297	3.18	3.10	0.022 019	0.002 241
4HE690A345B322M2	3.65	3.58	0.023 008	0.002 341

Table 16: List of Q^2 and form factor ratio $\lvert\mathcal{F}_{\text{ratio}}(Q_0{}^2)\rvert^2$ of the second iteration, spectrometer A.

Setup	$\widetilde{Q}^2$ [fm^{-2}]	Q_0^2 [fm^{-2}]	$\lvert\mathcal{F}_{\text{ratio}}({Q_0}^2)\rvert^2$	$\Delta\lvert\mathcal{F}_{\text{ratio}}({Q_0}^2)\rvert^2$
4HE450A261B293	1.30	1.24	0.005 594	0.000 511
4HE450A322B163	0.41	0.39	0.001 091	0.000 091
4HE450A323B183	0.51	0.49	0.001 296	0.000 114
4HE450A323B201	0.62	0.59	0.001 851	0.000 157
4HE450A323B226	0.78	0.75	0.002 582	0.000 226
4HE450A323B262	1.05	1.00	0.004 184	0.000 374
4HE690A240B240	2.06	1.99	0.011 800	0.001 130
4HE690A270B240	2.06	1.99	0.011 374	0.001 102
4HE690A270B255	2.31	2.24	0.013 283	0.001 317
4HE690A297B270	2.58	2.51	0.015 388	0.001 489
4HE690A297B283	2.83	2.74	0.016 048	0.001 567
4HE690A322B169	1.03	1.00	0.004 543	0.000 426
4HE690A322B189	1.28	1.24	0.006 253	0.000 595
4HE690A322B207	1.54	1.49	0.008 054	0.000 771
4HE690A322B224	1.80	1.74	0.009 893	0.000 947
4HE690A322B240	2.06	1.99	0.011 491	0.001 114
4HE690A322B297	3.11	3.01	0.018 124	0.001 771
4HE690A345B322M2	3.63	3.52	0.020 715	0.001 986
4HE795A337B181	1.56	1.52	0.008 568	0.000 843
4HE795A337B208	2.05	2.00	0.012 194	0.001 220
4HE795A337B233	2.56	2.50	0.015 585	0.001 568
4HE795A337B256	3.08	3.00	0.018 935	0.001 929
4HE795A337B277	3.58	3.50	0.021 932	0.002 222
4HE795A337B298	4.12	4.03	0.024 295	0.002 474
4HE795A337B317	4.64	4.52	0.025 534	0.002 557
4HE795A337B335	5.15	5.02	0.031 260	0.003 183

Table 17: List of Q^2 and form factor ratio $\lvert\mathcal{F}_{\text{ratio}}({Q_0}^2)\rvert^2$ of the second iteration, spectrometer B.

Parameter	Value	Error
a_1	0.467×10^{-4}	$\pm 0.239 \times 10^{-4}$
a_2	-8.375×10^{-4}	$\pm 1.768 \times 10^{-4}$
a_3	39.658×10^{-4}	$\pm 3.697 \times 10^{-4}$
a_4	10.063×10^{-4}	$\pm 2.013 \times 10^{-4}$

Table 18: Fit parameters for the transition form factor ratio fit (54), iteration 1.

Parameter	Value	Error
a_1	1.118×10^{-4}	$\pm 0.149 \times 10^{-4}$
a_2	-13.358×10^{-4}	$\pm 1.099 \times 10^{-4}$
a_3	49.071×10^{-4}	$\pm 2.295 \times 10^{-4}$
a_4	7.740×10^{-4}	$\pm 1.238 \times 10^{-4}$

Table 19: Fit parameters for the transition form factor ratio fit (54), iteration 2.

Setup	Q_0^2 [fm^{-2}]	$\Gamma_{0,2}$ [MeV]	$\Delta\Gamma_{0,2}$ [MeV]	$\Gamma_{0,3}$ [MeV]	$\Delta\Gamma_{0,3}$ [MeV]
4HE450A261B293	0.89	0.312	0.174	0.299	0.084
4HE450A322B163	1.39	0.278	0.027	0.287	0.029
4HE450A323B183	1.38	0.269	0.027	0.277	0.028
4HE450A323B201	1.39	0.290	0.029	0.298	0.030
4HE450A323B226	1.39	0.261	0.030	0.274	0.030
4HE450A323B262	1.38	0.267	0.029	0.281	0.030
4HE690A240B240	1.68	0.272	0.035	0.289	0.036
4HE690A270B240	2.17	0.283	0.032	0.297	0.034
4HE690A270B255	2.16	0.293	0.034	0.303	0.034
4HE690A297B270	2.62	0.313	0.052	0.312	0.045
4HE690A297B283	2.63	0.330	0.129	0.317	0.078
4HE690A322B169	3.11	0.274	0.029	0.283	0.029
4HE690A322B189	3.10	0.266	0.027	0.278	0.028
4HE690A322B207	3.09	0.262	0.027	0.275	0.028
4HE690A322B224	3.11	0.284	0.035	0.286	0.033
4HE690A322B240	3.09	0.325	0.042	0.325	0.041
4HE690A322B297	3.10	0.279	0.029	0.288	0.029
4HE690A345B322M2	3.58	0.288	0.026	0.295	0.026

Table 20: List of Γ_0 for the Voigt profile (57) and the two investigated backgrounds 2 and 3 from Sec. 6.3 for spectrometer A. If the fit did not converge, the data point was omitted. Involving higher computation costs can improve this situation.

Setup	Q_0^2 [fm^{-2}]	$\Gamma_{0,2}$ [MeV]	$\Delta\Gamma_{0,2}$ [MeV]	$\Gamma_{0,3}$ [MeV]	$\Delta\Gamma_{0,3}$ [MeV]
4HE450A261B293	1.24	0.276	0.028	0.290	0.031
4HE450A322B163	0.39	0.271	0.041	0.289	0.035
4HE450A323B183	0.49	0.206	0.020	0.241	0.025
4HE450A323B201	0.59	0.299	0.036	0.305	0.035
4HE450A323B226	0.75	0.207	0.028	0.260	0.033
4HE450A323B262	1.00	0.185	0.019	0.211	0.019
4HE690A240B240	1.99	0.219	0.022	0.245	0.023
4HE690A270B240	1.99	0.217	0.021	0.242	0.023
4HE690A270B255	2.24	0.252	0.028	0.267	0.028
4HE690A297B270	2.51	0.227	0.025	-	-
4HE690A297B283	2.74	0.293	0.122	0.310	0.078
4HE690A322B169	1.00	-	-	0.110	0.031
4HE690A322B189	1.24	0.232	0.030	0.273	0.030
4HE690A322B207	1.49	0.302	0.064	0.313	0.056
4HE690A322B224	1.74	0.259	0.036	0.288	0.034
4HE690A322B240	1.99	0.246	0.023	0.264	0.025
4HE690A322B297	3.01	0.282	0.060	0.296	0.059
4HE690A345B322M2	3.52	0.237	0.073	0.278	0.078
4HE795A337B181	1.52	0.219	0.026	0.253	0.030
4HE795A337B208	2.00	0.285	0.088	0.298	0.087
4HE795A337B233	2.50	0.256	0.033	0.278	0.036
4HE795A337B256	3.00	0.258	0.039	0.277	0.045
4HE795A337B277	3.50	0.281	0.030	0.289	0.032
4HE795A337B298	4.03	0.271	0.028	0.282	0.032
4HE795A337B317	4.52	0.156	0.029	0.238	0.026
4HE795A337B335	5.02	0.307	0.047	-	-

Table 21: List of Γ_0 for the Voigt profile (57) and the two investigated backgrounds 2 and 3 from Sec. 6.3for spectrometer B. If the fit did not converge, the data point was omitted. Involving higher computation costs can improve this situation.

Setup	Q_0^2 [fm^{-2}]	$\Gamma_{0,2}$ [MeV]	$\Delta\Gamma_{0,2}$ [MeV]	$\Gamma_{0,3}$ [MeV]	$\Delta\Gamma_{0,3}$ [MeV]
4HE450A261B293	0.89	0.243	0.020	0.267	0.022
4HE450A322B163	1.39	0.283	0.025	0.299	0.027
4HE450A323B183	1.38	0.268	0.025	0.285	0.026
4HE450A323B201	1.39	0.308	0.030	0.326	0.032
4HE450A323B226	1.39	0.238	0.021	0.268	0.024
4HE450A323B262	1.38	0.258	0.023	0.285	0.026
4HE690A240B240	1.68	0.273	0.025	0.315	0.032
4HE690A270B240	2.17	0.267	0.022	0.298	0.024
4HE690A270B255	2.16	0.291	0.040	0.323	0.034
4HE690A297B270	2.62	-	-	-	-
4HE690A297B283	2.63	-	-	-	-
4HE690A322B169	3.11	0.313	0.046	-	-
4HE690A322B189	3.10	0.297	0.042	0.330	0.039
4HE690A322B207	3.09	0.282	0.038	0.321	0.042
4HE690A322B224	3.11	0.290	0.037	0.310	0.036
4HE690A322B240	3.09	-	-	-	-
4HE690A322B297	3.10	-	-	-	-
4HE690A345B322M2	3.58	-	-	-	-

Table 22: List of Γ_0 for parametrisation (58) and the two investigated backgrounds 2 and 3 from Sec. 6.3 for spectrometer A. If the fit did not converge, the data point was omitted. Involving higher computation costs can improve this situation.

Setup	Q_0^2 [fm^{-2}]	$\Gamma_{0,2}$ [MeV]	$\Delta\Gamma_{0,2}$ [MeV]	$\Gamma_{0,3}$ [MeV]	$\Delta\Gamma_{0,3}$ [MeV]
4HE450A261B293	1.24	0.321	0.099	0.321	0.031
4HE450A322B163	0.39	0.228	0.022	0.267	0.024
4HE450A323B183	0.49	0.195	0.016	0.247	0.021
4HE450A323B201	0.59	0.315	0.028	-	-
4HE450A323B226	0.75	0.190	0.016	0.256	0.022
4HE450A323B262	1.00	0.142	0.014	0.177	0.015
4HE690A240B240	1.99	0.199	0.020	0.259	0.023
4HE690A270B240	1.99	0.182	0.016	0.242	0.020
4HE690A270B255	2.24	0.237	0.019	0.266	0.022
4HE690A297B270	2.51	0.169	0.041	-	-
4HE690A297B283	2.74	0.244	0.021	0.300	0.027
4HE690A322B169	1.00	-	-	-	-
4HE690A322B189	1.24	0.220	0.018	0.289	0.023
4HE690A322B207	1.49	0.295	0.037	0.329	0.038
4HE690A322B224	1.74	0.231	0.019	0.306	0.027
4HE690A322B240	1.99	0.253	0.022	0.289	0.025
4HE690A322B297	3.01	0.242	0.021	0.277	0.025
4HE690A345B322M2	3.52	0.110	0.031	0.196	0.153
4HE795A337B181	1.52	0.232	0.039	0.299	0.045
4HE795A337B208	2.00	0.256	0.039	0.281	0.043
4HE795A337B233	2.50	0.238	0.048	0.323	0.069
4HE795A337B256	3.00	0.122	0.022	0.260	0.031
4HE795A337B277	3.50	0.252	0.027	0.280	0.034
4HE795A337B298	4.03	0.212	0.021	0.275	0.032
4HE795A337B317	4.52	-	-	0.178	0.035
4HE795A337B335	5.02	0.267	0.025	0.301	0.028

Table 23: List of Γ_0 for parametrisation (58) and the two investigated backgrounds 2 and 3 from Sec. 6.3 for spectrometer B. If the fit did not converge, the data point was omitted. Involving higher computation costs can improve this situation.

Setup	$Q_0{}^2$ [fm^{-2}]	$\lvert\mathcal{F}_{\mathrm{M0^+}_2}(Q_0^2)\rvert^2$	$\Delta\lvert\mathcal{F}_{\mathrm{M0^+}_2}(Q_0^2)\rvert^2$	$\lvert\mathcal{F}_{\mathrm{M0^+}_3}(Q_0^2)\rvert^2$	$\Delta\lvert\mathcal{F}_{\mathrm{M0^+}_3}(Q_0^2)\rvert^2$
4HE450A261B293	0.89	1.871	0.087	1.784	0.102
4HE450A322B163	1.39	2.410	0.122	2.264	0.107
4HE450A323B183	1.38	2.319	0.104	2.230	0.105
4HE450A323B201	1.39	2.303	0.103	2.159	0.101
4HE450A323B226	1.39	2.283	0.102	2.135	0.109
4HE450A323B262	1.38	2.324	0.104	2.233	0.107
4HE690A240B240	1.68	2.162	0.095	2.026	0.088
4HE690A270B240	2.17	1.925	0.085	1.842	0.080
4HE690A270B255	2.16	1.886	0.083	1.806	0.078
4HE690A297B270	2.62	1.568	0.070	1.446	0.062
4HE690A297B283	2.63	1.536	0.068	1.426	0.062
4HE690A322B169	3.11	1.235	0.057	1.179	0.051
4HE690A322B189	3.10	1.176	0.054	1.100	0.048
4HE690A322B207	3.09	1.182	0.054	1.116	0.049
4HE690A322B224	3.11	1.101	0.051	1.025	0.046
4HE690A322B240	3.09	1.149	0.052	1.091	0.047
4HE690A322B297	3.10	1.158	0.052	1.072	0.047
4HE690A345B322M2	3.58	0.834	0.040	0.813	0.036

Table 24: Tabulated values for $\lvert\mathcal{F}_{\mathrm{M0^+}}(Q_0^2)\rvert^2$ for $d\sigma_1$ (57) and backgrounds 2 and 3 Sec. 6.3, spectrometer A.

Setup	$Q_0{}^2$ [fm^{-2}]	$\lvert\mathcal{F}_{\mathrm{M0^+}_2}(Q_0^2)\rvert^2$	$\Delta\lvert\mathcal{F}_{\mathrm{M0^+}_2}(Q_0^2)\rvert^2$	$\lvert\mathcal{F}_{\mathrm{M0^+}_3}(Q_0^2)\rvert^2$	$\Delta\lvert\mathcal{F}_{\mathrm{M0^+}_3}(Q_0^2)\rvert^2$
4HE450A261B293	1.24	2.026	0.092	1.833	0.080
4HE450A322B163	0.39	0.852	0.098	0.770	0.236
4HE450A323B183	0.49	1.014	0.066	1.006	0.050
4HE450A323B201	0.59	1.228	0.065	1.229	0.056
4HE450A323B226	0.75	1.459	0.074	1.436	0.065
4HE450A323B262	1.00	1.849	0.086	1.765	0.077
4HE690A240B240	1.99	2.073	0.091	1.933	0.083
4HE690A270B240	1.99	1.998	0.088	1.913	0.082
4HE690A270B255	2.24	1.906	0.082	1.777	0.076
4HE690A297B270	2.51	1.697	0.073	1.614	0.069
4HE690A297B283	2.74	1.433	0.062	1.405	0.060
4HE690A322B169	1.00	2.054	0.093	2.025	0.088
4HE690A322B189	1.24	2.191	0.098	2.133	0.092
4HE690A322B207	1.49	2.237	0.097	2.200	0.094
4HE690A322B224	1.74	2.216	0.098	2.116	0.090
4HE690A322B240	1.99	2.075	0.091	1.962	0.084
4HE690A322B297	3.01	1.255	0.055	1.197	0.051
4HE690A345B322M2	3.52	0.926	0.042	0.970	0.059
4HE795A337B181	1.52	2.268	0.100	2.254	0.097
4HE795A337B208	2.00	2.059	0.091	2.013	0.087
4HE795A337B233	2.50	1.599	0.072	1.598	0.070
4HE795A337B256	3.00	1.284	0.060	1.241	0.055
4HE795A337B277	3.50	0.886	0.039	0.868	0.038
4HE795A337B298	4.03	0.618	0.029	0.601	0.027
4HE795A337B317	4.52	0.376	0.021	0.385	0.019
4HE795A337B335	5.02	0.246	0.016	0.254	0.013

Table 25: Tabulated values for $\lvert\mathcal{F}_{\mathrm{M0^+}}(Q_0^2)\rvert^2$ for $d\sigma_1$ (57) and backgrounds BG2 and BG3 Sec. 6.3, spectrometer B.

Setup	$Q_0{}^2$ [fm^{-2}]	$\lvert\mathcal{F}_{\mathrm{M0^+}_2}(Q_0^2)\rvert^2$	$\Delta\lvert\mathcal{F}_{\mathrm{M0^+}_2}(Q_0^2)\rvert^2$	$\lvert\mathcal{F}_{\mathrm{M0^+}_3}(Q_0^2)\rvert^2$	$\Delta\lvert\mathcal{F}_{\mathrm{M0^+}_3}(Q_0^2)\rvert^2$
4HE450A261B293	0.89	1.893	0.086	1.895	0.086
4HE450A322B163	1.39	2.434	0.121	2.358	0.121
4HE450A323B183	1.38	2.343	0.103	2.335	0.103
4HE450A323B201	1.39	2.342	0.102	2.319	0.102
4HE450A323B226	1.39	2.320	0.102	2.284	0.102
4HE450A323B262	1.38	2.349	0.104	2.344	0.104
4HE690A240B240	1.68	2.132	0.095	2.157	0.095
4HE690A270B240	2.17	1.919	0.084	1.931	0.084
4HE690A270B255	2.16	1.881	0.082	1.860	0.082
4HE690A297B270	2.62	1.579	0.070	1.558	0.070
4HE690A297B283	2.63	1.539	0.069	1.514	0.069
4HE690A322B169	3.11	1.251	0.056	1.231	0.056
4HE690A322B189	3.10	1.193	0.054	1.147	0.054
4HE690A322B207	3.09	1.196	0.054	1.161	0.054
4HE690A322B224	3.11	1.115	0.051	1.065	0.051
4HE690A322B240	3.09	1.162	0.052	1.132	0.052
4HE690A322B297	3.10	1.171	0.052	1.130	0.052
4HE690A345B322M2	3.58	0.856	0.040	0.898	0.040

Table 26: Tabulated values for $\lvert\mathcal{F}_{\mathrm{M0^+}}(Q_0^2)\rvert^2$ for $d\sigma_2$ (59) and backgrounds BG2 and BG3 Sec. 6.3, spectrometer A.

Setup	$Q_0{}^2$ [fm^{-2}]	$\lvert\mathcal{F}_{\mathrm{M0^+}_2}(Q_0^2)\rvert^2$	$\Delta\lvert\mathcal{F}_{\mathrm{M0^+}_2}(Q_0^2)\rvert^2$	$\lvert\mathcal{F}_{\mathrm{M0^+}_3}(Q_0^2)\rvert^2$	$\Delta\lvert\mathcal{F}_{\mathrm{M0^+}_3}(Q_0^2)\rvert^2$
4HE450A261B293	1.24	2.066	0.092	2.117	0.095
4HE450A322B163	0.39	0.861	0.098	0.878	0.099
4HE450A323B183	0.49	1.039	0.066	1.089	0.067
4HE450A323B201	0.59	1.241	0.065	1.311	0.066
4HE450A323B226	0.75	1.494	0.074	1.559	0.074
4HE450A323B262	1.00	1.904	0.086	1.964	0.086
4HE690A240B240	1.99	2.097	0.091	2.094	0.091
4HE690A270B240	1.99	2.012	0.088	1.975	0.087
4HE690A270B255	2.24	1.927	0.082	1.916	0.084
4HE690A297B270	2.51	1.722	0.073	1.694	0.074
4HE690A297B283	2.74	1.455	0.062	1.473	0.063
4HE690A322B169	1.00	2.016	0.093	2.016	0.091
4HE690A322B189	1.24	2.169	0.098	2.168	0.096
4HE690A322B207	1.49	2.208	0.097	2.205	0.096
4HE690A322B224	1.74	2.243	0.098	2.255	0.097
4HE690A322B240	1.99	2.080	0.091	2.015	0.091
4HE690A322B297	3.01	1.284	0.055	1.273	0.056
4HE690A345B322M2	3.52	0.947	0.042	0.998	0.043
4HE795A337B181	1.52	2.233	0.100	2.257	0.098
4HE795A337B208	2.00	2.037	0.091	2.003	0.090
4HE795A337B233	2.50	1.597	0.072	1.619	0.072
4HE795A337B256	3.00	1.303	0.060	1.294	0.060
4HE795A337B277	3.50	0.905	0.039	0.923	0.040
4HE795A337B298	4.03	0.639	0.029	0.644	0.030
4HE795A337B317	4.52	0.392	0.021	0.419	0.022
4HE795A337B335	5.02	0.259	0.016	0.291	0.016

Table 27: Tabulated values for $\lvert\mathcal{F}_{\mathrm{M0^+}}(Q_0^2)\rvert^2$ for $d\sigma_2$ (59) and backgrounds BG2 and BG3 Sec. 6.3, spectrometer B.

Legend:

The values in the data tables correspond to the following assignment, where the caption of the tables provides information to which spectrometer and resonance model (see Tab. 5) the values belong:

- $\widetilde{Q}^2$: central value of squared four-momentum for the elastic scattering. Only used for the form factor ratio.
- Q_0^2: central value of the monopole resonance. Used for the form factor ratio and the transition form factor.
- $|\mathcal{F}_{\text{ratio}}(Q_0{}^2)|^2$: transition form factor in ratio to the elastic peak.
- $\Gamma_{0,2}$: *full-width-at-half-maximum* of the monopole resonance determined with background model 2 (see Tab. 4).
- $\Gamma_{0,3}$: *full-width-at-half-maximum* of the monopole resonance determined with background model 3 (see Tab. 4).
- $|\mathcal{F}_{\text{M0}^+{}_2}(Q_0^2)|^2$ monopole transition form factor determined with background 2. The form factor in the table is multiplied with $10^4 \,/\, (4\pi)$ as in Fig. 55.
- $|\mathcal{F}_{\text{M0}^+{}_3}(Q_0^2)|^2$ monopole transition form factor determined with background 3. The form factor in the table is multiplied with $10^4 \,/\, (4\pi)$ as in Fig. 55.

LIST OF FIGURES

BIBLIOGRAPHY

[AC16] A1 Collaboration, Johannes Gutenberg University M. Institut für Kernphysike K. Institut für Kernphysike: *A1 Collaboration*. http://wwwa1.kph.uni-mainz.de/A1. Version: 2016. – Accessed: 2019-11-04

[Bac18] Bacca, Sonia: *Personal Communication*. 2018

[Bas11] Basunia, M. S.: List of energy levels for Al-27. In: *Nucl. Data Sheets 112, 1875* 112 (2011). http://www.nndc.bnl.gov/nudat2/getdataset.jsp?nucleus=27AL&unc=nds

[BBLO13] Bacca, Sonia ; Barnea, Nir ; Leidemann, Winfried ; Orlandini, Giuseppina: Isoscalar Monopole Resonance of the Alpha Particle: A Prism to Nuclear Hamiltonians. In: *Phys. Rev. Lett.* 110 (2013), Jan, 042503. http://dx.doi.org/10.1103/PhysRevLett.110.042503. – DOI 10.1103/PhysRevLett.110.042503

[BBLO15] Bacca, Sonia ; Barnea, Nir ; Leidemann, Winfried ; Orlandini, Giuseppina: Examination of the first excited state of ^{4}He as a potential breathing mode. In: *Phys. Rev. C* 91 (2015), Feb, 024303. http://dx.doi.org/10.1103/PhysRevC.91.024303. – DOI 10.1103/PhysRevC.91.024303

[Ber17] Beričič, J.: *Measurement of Generalized Polarizabilities of the Proton by Virtual Compton Scattering*, University of Ljubiljana, Faculty of Mathematics and Physics, Doktorarbeit, 2017

[BL13] Blobel, V. ; Lohrmann, E.: *Statistische und numerische Methoden der Datenanalyse*. Vieweg+Teubner Verlag, 2013 (Teubner Studienbücher Physik). https://books.google.de/books?id=W_clBgAAQBAJ. – ISBN 9783663056904

[Bro25] Broglie, Louis Victor Pierre R.: Recherches sur la théorie des quanta. In: *Annals Phys.* 2 (1925), S. 22–128

[BW36] Breit, G. ; Wigner, E.: Capture of Slow Neutrons. In: *Phys. Rev.* 49 (1936), Apr, 519–531. http://dx.doi.org/10.1103/PhysRev.49.519. – DOI 10.1103/PhysRev.49.519

[Che08] Chernykh, M.: *Electron Scattering on ^{12}C, the Structure of the Hoyle State and a Neutron Ball for (e,e'n) Experiments at the S-DALINAC*, Technische Universität Darmstadt, Doktorarbeit, 2008

[CHK+61] Crannell, H. ; Helm, R. ; Kendall, H. ; Oeser, J. ; Yearian, M.: Electron-Scattering Study of Nuclear Levels in Cobalt, Nickel, Lead, and Bismuth. In: *Phys. Rev.* 123 (1961), Aug, 923–938. http://dx.doi.org/10.1103/PhysRev.123.923. – DOI 10.1103/PhysRev.123.923

[Dir28] Dirac, P. A. M.: The Quantum Theory of the Electron. In: *Proceedings of the Royal Society of London. Series A, Containing Papers of a Mathematical and Physical Character.* 117 (1928), Nr. 778, S. 610–624. http://dx.doi.org/10.1098/rspa.1928.0023. – DOI 10.1098/rspa.1928.0023

[Dis92] Distler, M. O.: *Aufbau und Test einer Driftkammer*, Johannes Gutenberg-Universität, Mainz, Diplomarbeit, 1992

[Dis96] Distler, M. O.: *Elektroproduktion von neutralen Pionen am Wasserstoff an der Schwelle*, Johannes Gutenberg-Universität, Mainz, Doktorarbeit, 1996

[EKLM11] Epelbaum, Evgeny ; Krebs, Hermann ; Lee, Dean ; Meissner, Ulf-G.: Ab Initio Calculation of the Hoyle State. In: *Phys. Rev. Lett.* 106 (2011), May, 192501. http://dx.doi.org/10.1103/PhysRevLett.106.192501. – DOI 10.1103/PhysRevLett.106.192501

[ELO98] Efros, Victor D. ; Leidemann, Winfried ; Orlandini, Giuseppina: Exact ^{4}He spectral function in a semirealistic NN potential model. In: *Phys. Rev. C* 58 (1998), Jul, 582–585. http://dx.doi.org/10.1103/PhysRevC.58.582. – DOI 10.1103/PhysRevC.58.582

[Ess13] Esser, A.: *Zerfallspionenspektroskopie leichter Hyperkerne in der Elektroproduktion*, Johannes Gutenberg-Universität, Mainz, Doktorarbeit, 2013

[Exc16] Excellence, Johannes Gutenberg University M. o.: *Teilchenbeschleuniger MESA*. http://mesa.kph.uni-mainz.de/. Version: 2016. – Accessed: 2019-11-04

[For83] Forest, Taber D.: Off-shell electron-nucleon cross sections: The impulse approximation. In: *Nuclear Physics A* 392 (1983), Nr. 2, 232 - 248. http://dx.doi.org/https://doi.org/10.1016/0375-9474(83)90124-0. – DOI https://doi.org/10.1016/0375–9474(83)90124–0. – ISSN 0375–9474

[F.R11] F.R.S., Professor E. R.: LXXIX. The scattering of α and β particles by matter and the structure of the atom. In: *The London, Edinburgh, and Dublin Philosophical Magazine and Journal of Science* 21 (1911), Nr. 125, S. 669–688. http://dx.doi.org/10.1080/14786440508637080. – DOI 10.1080/14786440508637080

[FRC+68] Frosch, R.F. ; Rand, R.E. ; Crannell, Hall ; McCarthy, J.S. ; Suelzle, L.R. ; Yearian, M.R.: Inelastic electron scattering from ^{4}He. In: *Nuclear Physics A* 110 (1968), Nr. 3, 657 - 673. http://dx.doi.org/https://doi.org/10.1016/0375-9474(68)90379-5. – DOI https://doi.org/10.1016/0375–9474(68)90379–5. – ISSN 0375–9474

[Fri00] Friedrich, J.: *Messung der Virtuellen Comptonstreuung an MAMI zur Bestimmung Generalisierter Polarisierbarkeiten des Protons*, Johannes Gutenberg-Universität, Mainz, Doktorarbeit, 2000

[FV82] Friedrich, J. ; Voegler, N.: The salient features of charge density distributions of medium and heavy even-even nuclei determined from a systematic analysis of elastic electron scattering form factors. In: *Nuclear Physics A* 373 (1982), Januar, S. 192–224. http://dx.doi.org/10.1016/0375-9474(82)90147-6. – DOI 10.1016/0375–9474(82)90147–6

[Hei16] Heilig, M.: *Aufbau und Inbetriebnahme eines Helium-Kryotargets für Formfaktormessungen am Mainzer Mikrotron*, Johannes Gutenberg-Universität, Mainz, Diplomarbeit, 2016

[Hel56] Helm, Richard H.: Inelastic and Elastic Scattering of 187-Mev Electrons from Selected Even-Even Nuclei. In: *Phys. Rev.* 104 (1956), Dec, 1466–1475. http://dx.doi.org/10.1103/PhysRev.104.1466. – DOI 10.1103/PhysRev.104.1466

[HGK04] Hiyama, E. ; Gibson, B. F. ; Kamimura, M.: Four-body calculation of the first excited state of ^{4}He using a realistic NN interaction: $^4\mathrm{He}(e,e')^4\mathrm{He}(0_2^+)$ and the monopole sum rule. In: *Phys. Rev. C* 70 (2004), Sep, 031001. http://dx.doi.org/10.1103/PhysRevC.70.031001. – DOI 10.1103/PhysRevC.70.031001

[Jac64] Jackson, John D.: Remarks on the phenomenological analysis of resonances. In: *Nuovo Cim.* 34 (1964), S. 1644–1666. http://dx.doi.org/10.1007/BF02750563. – DOI 10.1007/BF02750563

[Jan06] Jankowiak, A.: The Mainz Microtron MAMI - Past and future. In: *The European Physical Journal A - Hadrons and Nuclei* 28 (2006), May, Nr. 1, 149–160. http://dx.doi.org/10.1140/epja/i2006-09-016-3. – DOI 10.1140/epja/i2006–09–016–3. – ISSN 1434–601X

[J.C32] J.Chadwick: Possible Existence of a Neutron. In: *Nature* 129 (1932), S. 312. http://dx.doi.org/https://doi.org/10.1038/129312a0. – DOI https://doi.org/10.1038/129312a0

[JMB79] John M. Blatt, Victor F. W.: *Theoretical nuclear physics*. Springer Verlag, 1979

[Koh01] Kohl, M.: *Elektroproduktion von π^+-Mesonen an ^{3}He und das Studium von Mediumeffekten*, Johannes Gutenberg-Universität, Mainz, Doktorarbeit, 2001

[KOM+83] Köbschall, G. ; Ottermann, C. ; Maurer, K. ; Röhrich, K. ; Schmitt, Ch. ; Walther, V.H.: Excitation of the quasi-bound state in ^{4}He by electron scattering at medium momentum transfer. In: *Nuclear Physics A* 405 (1983), Nr. 3, 648 - 652. http://dx.doi.org/https://doi.org/10.1016/0375-9474(83)90523-7. – DOI https://doi.org/10.1016/0375–9474(83)90523–7. – ISSN 0375–9474

[LB67] Lombard, R.M. ; Bishop, G.R.: The scattering of high-energy electrons by 27Al. In: *Nuclear Physics A* 101 (1967), Nr. 3, 601 - 624. http://dx.doi.org/https://doi.org/10.1016/0375-9474(67)90655-0. – DOI https://doi.org/10.1016/0375–9474(67)90655–0. – ISSN 0375–9474

[LEI09] LEIDEMANN, WINFRIED: THE LORENTZ INTEGRAL TRANSFORM (LIT) METHOD. In: *International Journal of Modern Physics E* 18 (2009), Nr. 05n06, 1339-1358. http://dx.doi.org/10.1142/S0218301309013567. – DOI 10.1142/S0218301309013567

[LLH+01] Liu, Yuyan ; Lin, Jieli ; Huang, Guangming ; Guo, Yuanqing ; Duan, Chuanxi: Simple empirical analytical approximation to the Voigt profile. In: *J. Opt. Soc. Am. B* 18 (2001), May, Nr. 5, 666–672. http://dx.doi.org/10.1364/JOSAB.18.000666. – DOI 10.1364/JOSAB.18.000666

[MAG15] MAGIX: *The MAGIX Project*. http://magix.kph.uni-mainz.de/. Version: 2015. – Accessed: 2019-11-04

[McC73] McCarty, R. D.: Thermodynamic Properties of Helium-4 from 2 to 1500 K at pressures to 10^8 Pa. In: *J. Phys. Chem. Ref. Data, Vol. 2, No. 4, 1973* (1973)

[MP68] Margulies, S. ; Phelan, J. J.: On the parametrization of resonances occurring near threshold. In: *Il Nuovo Cimento A (1965-1970)* 58 (1968), Dec, Nr. 4, 804–814. http://dx.doi.org/10.1007/BF02825371. – DOI 10.1007/BF02825371. – ISSN 1826–9869

[MT00] Maximon, L. C. ; Tjon, J. A.: Radiative corrections to electron-proton scattering. In: *Phys. Rev. C* 62 (2000), Oct, 054320. http://dx.doi.org/10.1103/PhysRevC.62.054320. – DOI 10.1103/PhysRevC.62.054320

[OKM+85] Ottermann, C.R. ; Köbschall, G. ; Maurer, K. ; Röhrich, K. ; Schmitt, Ch. ; Walther, V.H.: Elastic electron scattering from ^{3}He and ^{4}He. In: *Nuclear Physics A* 436 (1985), Nr. 4, 688 - 698. http://dx.doi.org/https://doi.org/10.1016/

0375-9474(85)90554-8. – DOI https://doi.org/10.1016/0375–9474(85)90554–8. – ISSN 0375–9474

[Sch26] Schrödinger, E.: Quantisierung als Eigenwertproblem. In: *Annalen der Physik* 385 (1926), Nr. 13, 437-490. http://dx.doi.org/10.1002/andp.19263851302. – DOI 10.1002/andp.19263851302

[Sic15] Sick, Ingo: Form Factors and Radii of Light Nuclei. In: *Journal of Physical and Chemical Reference Data* 44 (2015), 05. http://dx.doi.org/10.1063/1.4921830. – DOI 10.1063/1.4921830

[The72] Theissen, Horst: *Spectroscopy of light nuclei by low energy (< 70 MeV) inelastic electron scattering*. Berlin, Heidelberg : Springer Berlin Heidelberg, 1972. – 1–57 S. http://dx.doi.org/10.1007/BFb0041391. http://dx.doi.org/10.1007/BFb0041391

[TWH92] Tilley, D. R. ; Weller, H. R. ; Hale, G. M.: Energy levels of light nuclei A = 4. In: *Nucl. Phys.* A541 (1992), S. 1–104. http://dx.doi.org/10.1016/0375-9474(92)90635-W. – DOI 10.1016/0375–9474(92)90635–W

[Ueb71] Ueberall, Herbert: *Electron Scattering from Complex Nuclei*. Academic Press, 1971

[VFL+00] Vanderhaeghen, M. ; Friedrich, J. M. ; Lhuillier, D. ; Marchand, D. ; Van Hoorebeke, L. ; Wiele, J. Van d.: QED radiative corrections to virtual Compton scattering. In: *Phys. Rev. C* 62 (2000), Jul, 025501. http://dx.doi.org/10.1103/PhysRevC.62.025501. – DOI 10.1103/PhysRevC.62.025501

[Wal70] Walcher, Thomas: Unelastische Elektronenstreuung am ^{4}He bei kleinem Impulsübertrag*. In: *Zeitschrift Physik* 237 (1970), S. 368 – 380

[WBWB74] Wertheim, G. K. ; Butler, M. A. ; West, K. W. ; Buchanan, D. N. E.: Determination of the Gaussian and Lorentzian content of experimental line shapes. In: *Review of Scientific Instruments* 45 (1974), Nr. 11, S. 1369–1371. http://dx.doi.org/10.1063/1.1686503. – DOI 10.1063/1.1686503

[WSPC14] Wiringa, R. B. ; Schiavilla, R. ; Pieper, Steven C. ; Carlson, J.: Nucleon and nucleon-pair momentum distributions in $A \leq 12$ nuclei. In: *Phys. Rev. C* 89 (2014), Feb, 024305. http://dx.doi.org/10.1103/PhysRevC.89.024305. – DOI 10.1103/PhysRevC.89.024305